Normal Zone Propagation in a YBCO Superconducting Tape

Measurement and Analysis of Quasi-Adiabatic Normal Zone Propagation in a YBCO coated conductor

A technical report performed within the framework of a graduation assignment as part of the Applied Physics Master of Science programme, September 20, 2012

Author: J. van Nugteren
Supervisor: Dr. M.M.J. Dhallé

UNIVERSITY OF TWENTE.

Abstract

In this report the measured normal zone propagation velocity and minimal quench energy of YBCO coated conductor tapes are presented throughout a wide range of temperature, of the percentage of the critical current and applied magnetic field. For these measurements a pre-existing set-up is reassembled and improved. Surprisingly the measured data show that the normal zone propagation velocity depends predominantly on the current and hardly on temperature or applied magnetic field. The minimal quench energy, on the other hand, depends on all three external parameters. The measured data are then compared to analytical and numerical descriptions for the normal zone propagation and the minimal quench energy. This leads to the introduction of a cooling term into the analytical and numerical models to find a better agreement between the data and the model predictions. This means that the experiment is only quasi-adiabatic, as opposed to fully adiabatic. For the minimal quench energy, significant differences between the experiment and the models are found. These differences are explained by the relatively slow heat transfer between the heater and the tape, which causes only a fraction of the energy to be transferred, when the normal zone already develops.

Nomenclature

The following list clarifies the symbols used throughout the report.

Symbol	Description	Unit
A_1	First amplification factor for the quench detector	N.A.
A_2	Second amplification factor for the quench detector	N.A.
B	Magnetic field	$[T]$
C	One dimensional heat capacity	$[J/mK]$
C_0	Geometric average one dimensional heat capacity	$[J/mK]$
E	Electric field	$[V/m]$
E_0	Electric field used in the definition of the critical current	$[V/m]$
E_{pulse}	Energy contained in a heater pulse	$[J]$
f_{amp}	Amplification factor	N.A.
h	Heat transfer coefficient for cooling to the environment	$[W/mK]$
h_{cu}	Thickness (height) of the copper layer	$[m]$
i	Index of Node	N.A.
J_c	Critical current density	$[A/mm^2$
I	Electrical current	$[A]$
I_{op}	Sample current	$[A]$
I_{sample}	Sample current	$[A]$
I_{nc}	Electrical current in the normal conducting parts of the sample	$[A]$
I_{sc}	Electrical current in the superconducting parts of the sample	$[A]$
k	One dimensional thermal conductivity	$[Wm/K]$
MQE	Minimal quench energy	$[J]$
n_{nodes}	Total number of nodes	N.A.
N	N-value of a superconductor	N.A.
P_Ω	Ohmic heating power	$[J/sm]$
P_i	Quench initialisation power	$[J/sm]$
P_c	Cooling power	$[J/sm]$
QE	Quench energy	$[J]$
r_{sh}	Radius of the sample holder	$[m]$
R	Electrical resistance	$[\Omega]$
$R_{T=293\ K}$	Electrical resistance at room temperature	$[\Omega]$
t	Time	$[s]$
t_{pulse}	Duration of a heat pulse	$[s]$
T	Temperature	$[K]$
T_{cs}	Current sharing temperature	$[K]$
T_c	Critical temperature	$[K]$
T_t	Transition temperature	$[K]$
T_{op}	Operating temperature	$[K]$
T_{env}	Environmental temperature	$[K]$
T_i	Temperature of the node at index i	$[K]$
$\tilde{T}$	Average temperature between T_t and T_{op}	$[K]$
U	Voltage	$[V]$
U_{in}	Input voltage of the quench detector	$[V]$
U_{offset}	Offset voltage of the quench detector	$[V]$
U_{trig}	Trigger level of the quench detector	$[V]$
V_{nzp}	Normal zone propagation velocity	$[m/s]$
w_{sample}	Sample width	$[m]$
x	Spacial coordinate	$[m]$

Symbol	Description	Unit
x_i	position of the node at index i	$[m]$
z	Spacial coordinate in a moving coordinate system	$[m]$
z_i	position of the node at index i	$[m]$
α	Stekly parameter	N.A.
γ	Damping factor for steady state model	$[m/s^2K]$
ϵ	Thermal emissivity	N.A.
ζ_e	Time constant for heat flux from the hot spot to the environment	$[s]$
ζ_s	Time constant for the heat flux from the normal zone front to the sample ends	$[s]$
ρ	One dimensional electrical resistivity	$[\Omega/m]$
σ_{boltz}	Stefan-Boltzmann constant	$[W/m^2K^4]$
σ_{hoop}	Hoop stresses in sample	$[N/m^2]$
ℓ_{vt}	Length spanned by a voltage tap	$[m]$
ℓ_{nz}	Length of the normal zone	$[m]$
ℓ_{mpz}	Length of the minimal propagation zone	$[m]$
τ_{sample}	Sample thickness	$[m]$

Contents

Chapter 1 Introduction

This report describes both the measurement and the modelling of adiabatic Normal Zone Propagation (NZP) in a YBCO coated conductor. In Section 1.1 a general introduction is given to superconductivity. Readers interested in a more complete discussion are referred to Tinkham [1] or Cyrot & Pavuna [2]. Because YBCO coated conductors belong to the high temperature superconductors (HTS) they are introduced in Section 1.2. These new HTS materials have properties that allow a wider range of applications than the classical low temperature superconductors. Some of these applications are described in Section 1.3. One of the issues for HTS materials, which needs more research, is their thermal stability and quench protection. An introduction to these concepts is given in Section 1.4. Finally, in Section 1.5 an overview of the assignment and chapter layout is given.

1.1 Superconductivity

Superconductivity is a phenomenon that causes the resistivity in certain materials to become zero at temperatures below their characteristic critical temperature. The phenomenon was first discovered in mercury by Heike Kamerlingh Onnes on April 8, 1911 [3]. Since then many other superconducting materials have been found. Superconductors can be divided into two major groups: type I and type II superconductors. Type I materials are typically elements such as Pb and Hg, while type II materials are usually compounds such as $NbTi$, Nb_3Sn and $YBa_2Cu_3O_{7-x}$. The two groups set themselves apart through their behaviour in magnetic field. A type I superconductor tries to expel magnetic field by setting up shielding currents, a phenomenon called the Meissner effect. When the magnetic field becomes too strong for the shielding current, superconductivity is lost. Type II materials, however, are able to maintain superconductivity up to higher field by allowing magnetic flux quanta to penetrate the material, a phenomenon called the Abrikosov effect. Because the electrical current around these flux quanta is circular, they are often also called vortices. By introducing material defects and impurities in the material, it is energetically more favourable for vortices to be 'pinned' on these locations, preventing power dissipation in the material due to flux line movement. This way the material can maintain its superconductivity up to much higher field and current than type I superconductors. However, when the current density becomes too high, the Lorentz forces on the vortices exceed the pinning forces, resulting in the movement of the fluxlines, which causes power dissipation and thus the appearance of resistivity. This effect places an upper limit on the current density flowing through the material, named its critical current density, or, in the case of a superconducting wires or cables, their critical current. The critical current depends on both the temperature and the magnitude of the magnetic field, forming a critical surface which is unique to each material.

Traditionally the main application area for superconductivity is magnet construction. Because superconductors have zero resistivity, a magnet wound with superconducting wires can operate without electric loss. This allows for the construction of magnets that generate higher field than for instance a magnet wound with copper wires. Because Niobium Titanium ($NbTi$) is the only ductile type II superconductor, it has become the workhorse for many applications, such as the magnets for accelerators and MRI systems. It has a critical temperature of 9.2 K and a critical field of 14.2 T. The critical surface of the state-of-the-art NbTi conductors used in the vast majority of the Large Hadron Collider (LHC) magnets in CERN is shown in Figure 1.1. Another superconductor of interest is Tri-Niobium Tin (Nb_3Sn), it has a critical temperature of 18.3 K and a critical field of 30 T, which both are superior to the corresponding values of $NbTi$. However Nb_3Sn is brittle and is therefore more difficult to implement in a coil. The usual strategy is to wind the coil first and only then to react the niobium and the tin (which are contained inside the strands) afterwards using a heat treatment. The critical surface of typical Nb_3Sn conductors prepared with the Powder In Tube (PIT) process, a state-of-the-art method to produce high-performance wires, is presented in Figure 1.2.

1.2 High Temperature Superconductors

Both $NbTi$ and Nb_3Sn are low temperature superconductors (LTS). In the late 20th century a new class of superconductors was discovered: high temperature superconductors (HTS). One of these HTS materials is Ytrium Barium Copper Oxide ($YBa_2Cu_3O_{7-x}$ or in short YBCO) which was discovered in 1986 [4]. The critical temperature of YBCO is 93 K, making it the first material discovered with a critical temperature above 77 K, the boiling point of liquid Nitrogen. Be-

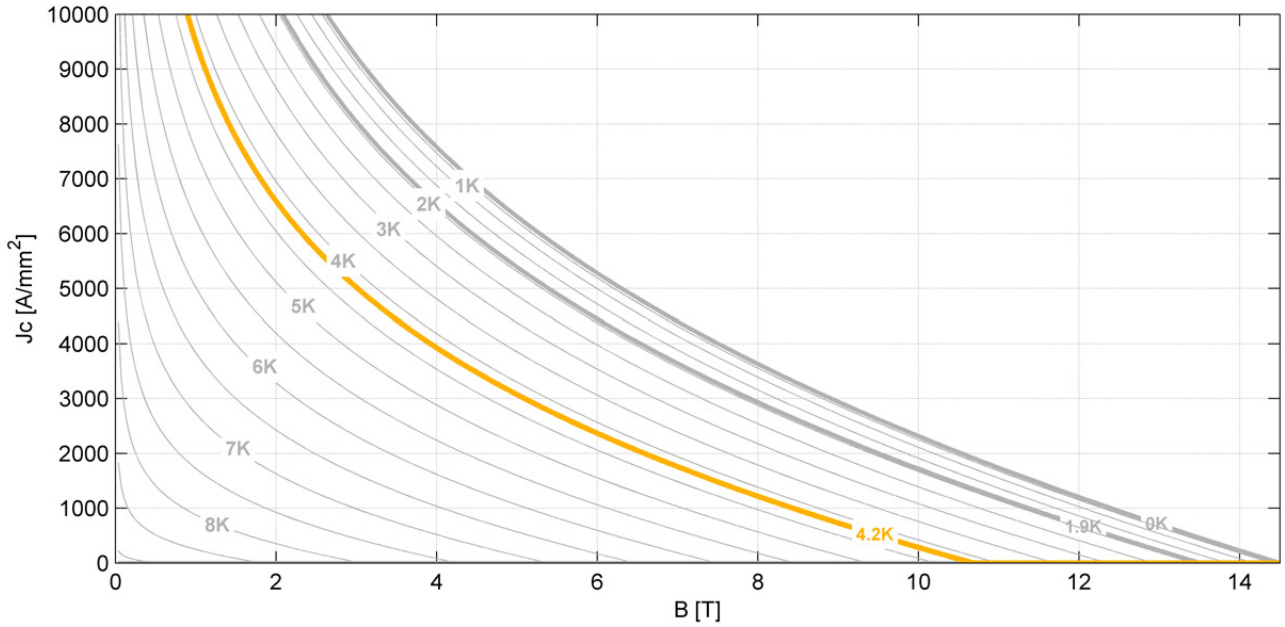

Figure 1.1: Illustration of the critical surface of LHC grade $NbTi$ (as defined by the Bottura scaling relation [5, 6]). The critical current density J_c is plotted against the magnetic induction. Each curve corresponds to a different temperature decreasing from the bottom left to the top right of the graph. The yellow line is the critical current density at the boiling point of liquid helium. Note that J_c is the current density in the superconducting parts of the composite wires used in these magnets only.

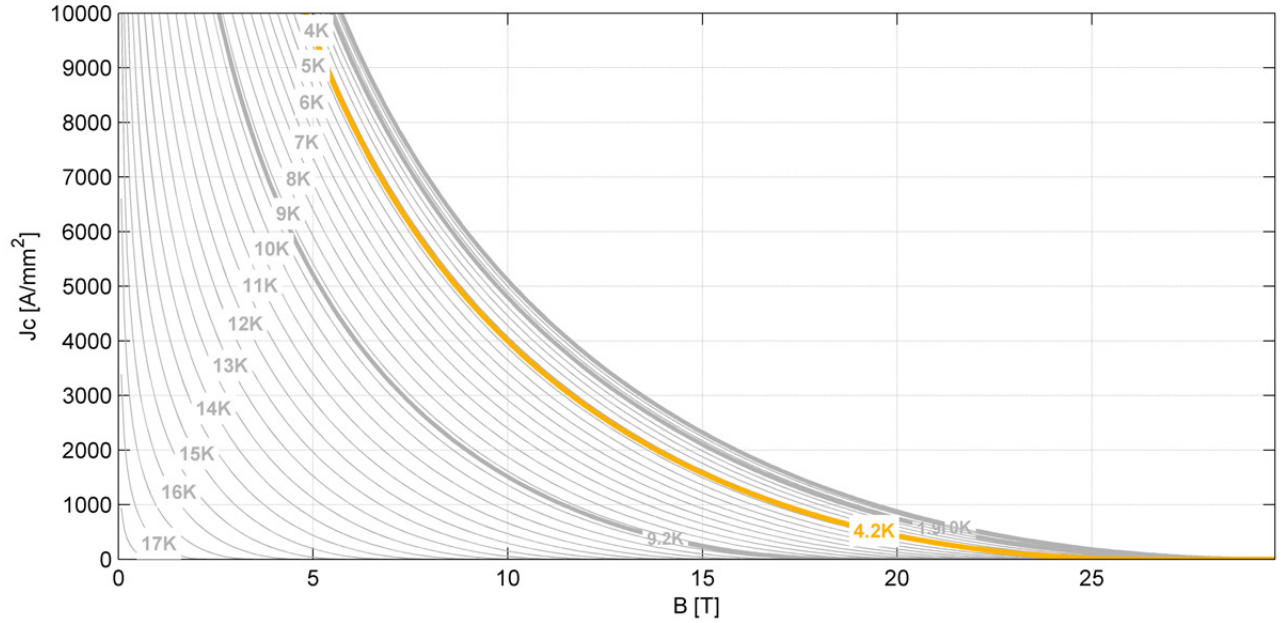

Figure 1.2: Illustration of the critical surface of PIT Nb_3Sn (as defined by the Godeke scaling relation [7]). The yellow line is the critical current density at the boiling point of liquid helium. Note that this is the current density in the superconductor only and that both the temperature range and the scaling of the horizontal axes is different from that of Figure 1.1.

cause the crystal structure of YBCO is highly anisotropic the upper critical field[1] depends on the angle of the magnetic field with respect to the orientation of the crystallographic copper oxide planes. It is estimated that when the field is perpendicular to these layers the upper critical field lies at 120 T and when the field is parallel to the copper oxide layers the critical field becomes 240 T [8]. However, because of the complex crystal structure and the short coherence length of the superconductor, YBCO has proven to be quite difficult to manufacture into long lengths of conductor. Initially thanks to advances in Pulsed Laser Deposition (PLD) and later also through less expensive wet chemical deposition techniques, companies such as Superpower and American Superconductor are now able to manufacture YBCO tapes with a near-mono-crystalline micro-structure, of multiple kilometres in length. Just like the LTS, these conductors are composite materials which contain several other metals and oxides besides the YBCO. Because the superconductor to non-superconductor fraction is still relatively low, improvements in terms of critical current can still be expected in the near future.

Another HTS worth mentioning is Bismuth Strontium Calcium Copper Oxide ($Bi_2Sr_2Ca_{n-1}Cu_nO_{2n+4+x}$ or in short BSCCO). BSCCO was discovered in 1988 at the National Research Institute for Metals in Japan [9]. In the most commonly used variant n equals three and this material is therefore named BSCCO 2223. It has a critical temperature of 108 K and an upper critical field of approximately 200 T [10]. Despite being discovered later than YBCO, it was the first HTS superconductor to be manufactured into practical wires, based on a relatively straightforward Powder In Tube (PIT) method. However the unavoidable use of expensive silver as the tube material, but especially also its poor performance in high magnetic field and temperature (due to poor vortex pinning), has made BSCCO currently a less favourable candidate for practical applications.

1.3 Applications

The major advantage of working with superconductors opposed to copper or other Ohmic conductors is that they allow for much higher current densities. This makes it possible to design compact and efficient magnets, which is very important for particle accelerators and detectors, because of the space limitations and power consumption in these devices. But also for Magnetic Resonance Imaging (MRI) and Nuclear Magnetic Resonance (NMR) systems, the use of superconducting magnets is commonplace, especially in view of the higher magnetic field that they permit. However, due to the cryogenic infrastructure required (its cost, but often also perceived questions regarding its unproven reliability), further commercial application has remained minor. Nevertheless this is currently shifting due to the availability of longer stretches of YBCO coated conductor, which allows for practical application at higher temperatures. This has led to the development of the first superconducting motors and generators, which operate at temperatures well above 4.2 K, the boiling point of liquid helium (which is the cooling medium of the vast majority of LTS applications [11, 12]). Because the current densities in the superconductor can be much higher, these machines can be reduced in size and weight by a significant amount compared to their Copper-based counterparts [13]. Superconducting rotating machinery for example can be used in combination with a diesel generator as a compact agile ship engine, or in a 10 MW wind converter as a compact light-weight generator. In addition to its possible use at higher temperatures, at 4.2 K YBCO also allows for application at higher magnetic field, for example in accelerator magnets generating fields above 20 T. Because the price of coated conductors is still relatively high, compared to LTS materials, the envisaged strategy is to build hybrid coils that use $NbTi$ in the low field region, Nb_3Sn in the medium field region and YBCO as an insert in the high field region [14].

1.4 Thermal Stability and Quench Protection

One of the main issues in the design of superconducting devices concerns the so-called thermal stability of the conductor. When the temperature in the conductor rises locally above the critical temperature (this can be caused for example by a sudden movement of a strand due to the formation of cracks in the impregnating resin under influence of Lorentz forces, or in accelerator magnets by highly energetic particles hitting the conductor), then superconductivity is lost in this localized 'zone' and Ohmic heating will occur. If this normal zone is small, heat transport to the colder areas of the conductor at both ends of the zone exceeds the volumetric heat generation inside the normal zone, causing it to collapse again. However, if the normal zone exceeds a certain critical length, then the heat generation becomes larger than the cooling and the normal zone will expand. The latter phenomenon is called a quench.

When a quench occurs it is of importance to detect it as quickly as possible, so that damage to the conductor, due to localized heating, can be avoided. For small magnets it is often sufficient to shut down the current supply, after which the energy stored in the magnetic field of the coil can dissipate in its cold mass. For larger magnets however, it is of importance to fire quench heaters that on purpose create multiple normal zones in the magnet. This allows the stored energy to dissipate more evenly throughout the entire volume of the device, so that local excessive temperature rises are avoided. For the design of a quench protection system two parameters are of interest: the Normal Zone Propagation

[1] The upper critical field is the magnetic field at which the vortex density in type II superconductors becomes so large that even in these materials superconductivity is lost.

Velocity (V_{nzp}) and the Minimal Quench Energy (MQE). The first is the speed with which the superconducting-to-normal transition front travels as the normal zone expands. From a practical viewpoint, it determines the delay between the start of a quench and its detection by the protection electronics (since it dictates the rate of voltage buildup), as well as how evenly heat is spread out along the conductor. Generally it is preferable to have V_{nzp} as high as possible, as this leads to faster build-up of voltage, increasing the ease of detection. Additionally a higher V_{nzp} reduces the number of required quench heaters, because the quench spreads faster through the coil. The MQE, on the other hand, is defined as the smallest amount of energy required to initiate a propagating normal zone. It is important because it determines the risk that a quench occurs. For LTS materials, both MQE and V_{nzp} depend on magnetic field, current and temperature. Thermal stability of LTS has extensively been studied for $\sim 50\ years$ now and it might even be argued that these studies were essential in order to make the realisation of the first commercial MRI systems $\sim 30\ years$ ago possible. These studies lead to a satisfactory understanding of the coupled (and non-linear) thermal and electromagnetic processes involved in the propagation of a normal zone. These 'classical' models that were developed for LTS conductors shall be discussed in detail in Section 4.2, where we shall comment on their applicability to HTS materials.

1.5 Assignment and Chapter Layout

In order to propagate, a normal zone in essence needs to generate a sufficient amount of Ohmic heat to raise the temperature of the colder area in front of the zone all the way up to the normal state. Basically, this amount is determined by the (integrated) heat capacity of the material and by the temperature difference between the background operational temperature and the transition temperature (the so-called thermal margin). In LTS, operating at 4.2 K, the heat capacity is very small and the thermal margin dominates the overal behaviour. HTS, on the other hand, may operate at a ~ 10 times higher temperature and the temperature-dependent heat capacity can become orders of magnitude higher. As H. van Weeren showed in his Phd. thesis [15], in MgB_2 conductors this leads to a competition between increasing heat capacity (rendering the conductor more stable) and decreasing thermal margin (making it less stable). This competition manifests itself in a non-monotonic temperature dependence of both MQE and V_{nzp}. Maybe the main lesson learned out of this earlier work is that the temperature, magnetic field and current dependence of the key stability parameters becomes richer than with the well studied LTS materials.

In the present context, for the construction of HTS devices it is important to know the quench propagation characteristics of YBCO tape conductor throughout the envisaged operational temperature-, magnetic field- and current range. However, even if applications are foreseen at temperatures ranging all the way from 4.2 K to 77 K and all of them typically involve current levels of several hundreds of amperes, all data available on V_{nzp} and MQE of YBCO coated conductor lies in the temperature range of $40 - 77\ K$ and currents below 100 A [16, 17, 18, 19, 20, 21, 22, 23][2]. The NZP setup at the University of Twente, allows for measurement at lower temperatures and much higher currents. Therefore the assignment described in this report is to measure both the adiabatic Normal Zone Propagation Velocity and the Quench Energy for YBCO coated conductor, at various values of magnetic field, current and temperature. The assignment is performed within the framework of a graduation project, within the MSc. programme in Applied Physics at the University of Twente.

The report is subdivided into 4 Chapters. This present chapter has given a general introduction to superconductivity. Chapter 2 describes the experimental setup that is used for the measurements. The results from these measurements are then presented in Chapter 3. Finally, in Chapter 4, a number of models is introduced that are used to further understand the acquired results.

[2]These literature data are presented in more detail and compared to our results in Section 4.5.

Chapter 2 Experimental Setup

This Chapter describes the experimental setup used for the measurement of temperature-, magnetic field- and current dependent quench propagation under adiabatic conditions. This 'time-of-flight' type of experiment has been used at the University of Twente since the late eighties of last century [24, 25] and was originally designed to characterize LTS wires at a fixed temperature of 4.2 K*. In 2007 it was redesigned to operate at variable baseline temperature by H. van Weeren for the study of quench propagation in Magnesium di-Boride (MgB_2) [15]. Afterwards all the instrumentation controlling the experiment was dismantled. During the course of this assignment the instrumentation had to be reassembled from scratch. This led to the introduction of a new data acquisition system based upon Labview and NiDAQ. Additionally, the embedded heater, which is an important component of the sample holder, was replaced because its current leads were broken.*

2.1 Overview

In a time-of-flight type of experiment, temperature, magnetic field and current through the sample are allowed to stabilize at chosen values before a localized heat pulse is injected. If the pulse does not trigger a quench, the temperature is allowed to stabilize again after which a pulse with increased energy is injected. When a quench does occur, the speed of the superconducting-to-normal transition front is deduced from voltage-versus-time recordings at various distances from the initial heat pulse location.

The measurements presented in this report are 'quasi-adiabatic'. This means that the normal zones that are created can only expel their ohmic heat through the sample itself, towards the colder and still superconducting sample parts at either side of the zone. Nearly no heat is exchanged with the sample holder itself, at least not on a time scale relevant for the propagation of the zone[1].

One important point of worry in the design of such an adiabatic NZP experiment are the current contacts. High current levels pass the resistive terminals at either end of the sample and the heat generated in these contacts must be cooled efficiently so that they do not warm up the sample. Figure 2.1 gives a schematic overview of the sample holder in its present form, while Figure 2.2 shows a photograph of the holder with the first YBCO sample mounted. Roman numerals in the text below refer to various parts indicated in Figure 2.1. A helical sample is mounted between two copper flanges (I) that are kept at a temperature of 4.2 K by a liquid helium reservoir inside of the hollow sample holder (II). Two different types of sample were measured. It is necessary to use a different layout of the heaters, sensors and voltage taps on each of these sample types. After all changes to instrumentation and sample holder, the setup is first tested using a Nb_3Sn tape. This 'Gorizont' tape and its associated layout is discussed in Section 2.2.

After the setup is thus tested, a series of YBCO tapes (III) are mounted. These coated conductors are discussed, together with their experimental layout, in Section 2.3. All samples are soldered to the copper flanges (I) using a low temperature solder, based on a Bismuth Lead Tin alloy ($Bi_{46}Sn_{34}Pb_{20}$) that has a melting point around 105 °C [26]. This simplified the mounting of the samples and prevented the current leads (IV) from being unsoldered from the inside of the sample holder. The current through the sample is supplied via the copper flanges by two Nb_3Sn current leads which are both connected through the helium bath. The main advantage is that the leads are kept at 4.2 K at all times, without influencing the adiabatic conditions of the sample. Underneath the sample a newly constructed embedded heater (H_{embed} (V)) allows to raise the global temperature of the sample. However, as discussed above, this needs to be performed as adiabatic as possible. Small ridges (VI) on the surface of the embedded heater raise the sample slightly, reducing thermal contact between the sample and the heater. In addition to the embedded heater, two small heaters (H_1 and H_2) are mounted directly on the sample in order to flatten the temperature profile of the sample. The temperature of the tape is monitored by several CERNOX temperature sensors (T_1, T_2 and T_3), which are connected in series.

In Section 2.4 the temperature control of the sample and the construction of the embedded heater are discussed in more detail. To initiate a normal zone, a quench heater (H_Q) is mounted on the tape. Finding a good design for the quench

[1] In Appendix B these time constants are estimated and it will be shown that the set-up remains adiabatic as long as $h << C_s^2 V_{nzp}^2 / k$, with h the heat transfer coefficient to the environment; C_s the heat capacity of the sample; V_{nzp} the propagation velocity of a normal zone and k the longitudinal heat conductivity along the sample.

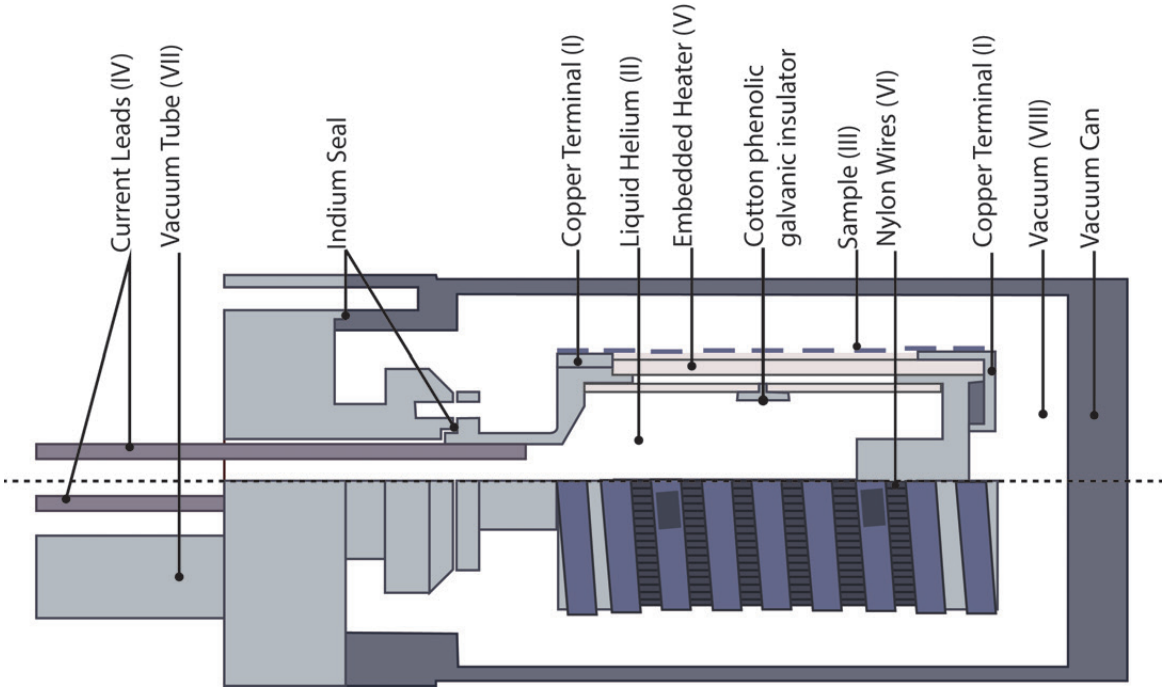

Figure 2.1: Geometry of the sample holder. Note that the image is turned 90° counter-clockwise. The roman numerals refer to the components described throughout the overview presented in Section 2.1.

heater proved to be challenging. Therefore the quench heater and the underlying systems are discussed in more detail in Section 2.5. The propagation of the quench is measured using three voltage taps (V_1, V_2 and V_3), that are soldered consecutively to the tape near the quench heater. The time shift of the voltage profiles and the distance between the voltage taps are then used to calculate V_{nzp}. The same voltage taps are also used for the measurement of the critical current. This means that the measurement system for the voltages has to be simultaneously fast and sensitive. The systems for measuring the voltage are described in more detail in Section 2.6. To prevent the temperature from rising too excessively during a quench (which can burn out the sample), a protection system shuts down the sample current when a quench occurs. However, if this happens too quickly, the quench does not propagate past the voltage taps, preventing the acquisition of useful data. The quench protection and the sample current control systems are described in Section 2.7.

An overview schematic of the instrumentation is presented in Figure 2.3. The layouts of the sample holder differ for each of the samples and are therefore presented separately, in Figure 2.4 for Gorizont and in Figure 2.6 for YBCO. Because part of the wiring to the sample holder is broken, an additional set of wire pairs has been added through the vacuum tube (VII). With this procedure the labelling of the wire pairs changes as well. The new wire pairs are labeled 1-9 and the old wire pairs that run through the helium bath are labeled 21-32 (basically the old value plus twenty). An overview of all wire pairs and their respective labeling is presented in Table 2.1.

2.2 Gorizont Sample Layout

In order to test the experimental setup with the new instrumentation and to develop some routine in the experimental procedures using a relatively robust sample, measurements are performed on a Nb_3Sn Gorizont tape, which is well-characterized in a much earlier project [27, 28]. Gorizont is a Nb_3Sn tape conductor which was developed as an alternative to the wind and react bronze path conductors. The tape is approximately 5 mm wide and 0.2 mm thick and has a shape and size comparable to that of the YBCO conductors.

For this first measurement the layout of the sample is very similar to that proposed by van Weeren [15] (See Figure 2.4). A quench heater is placed on each side of the sample, one as backup for the other. At this stage the quench heater is basically a short length of manganin wire wound around a piece of copper that is soldered to the tape. Between the quench heaters, three consecutive voltage taps, each with a length of approximately 10 cm, are soldered to the tape. The temperature of the tape is monitored with three thermometers. Finally two baseline heaters are connected to the sample near the flanges, in order to control, together with the embedded heater, the temperature profile of the tape.

Since the data collected on this sample still may serve for future reference purpose but are not relevant for the assignment itself, they are briefly presented in Appendix E.

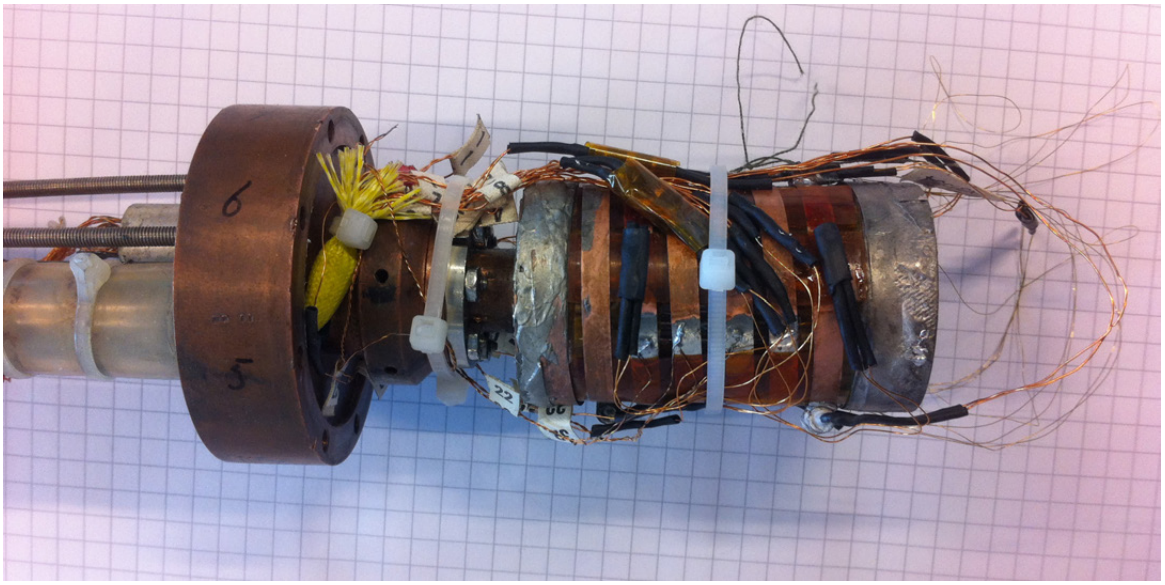

Figure 2.2: Photograph of the sample holder with the first SCS4050 tape mounted.

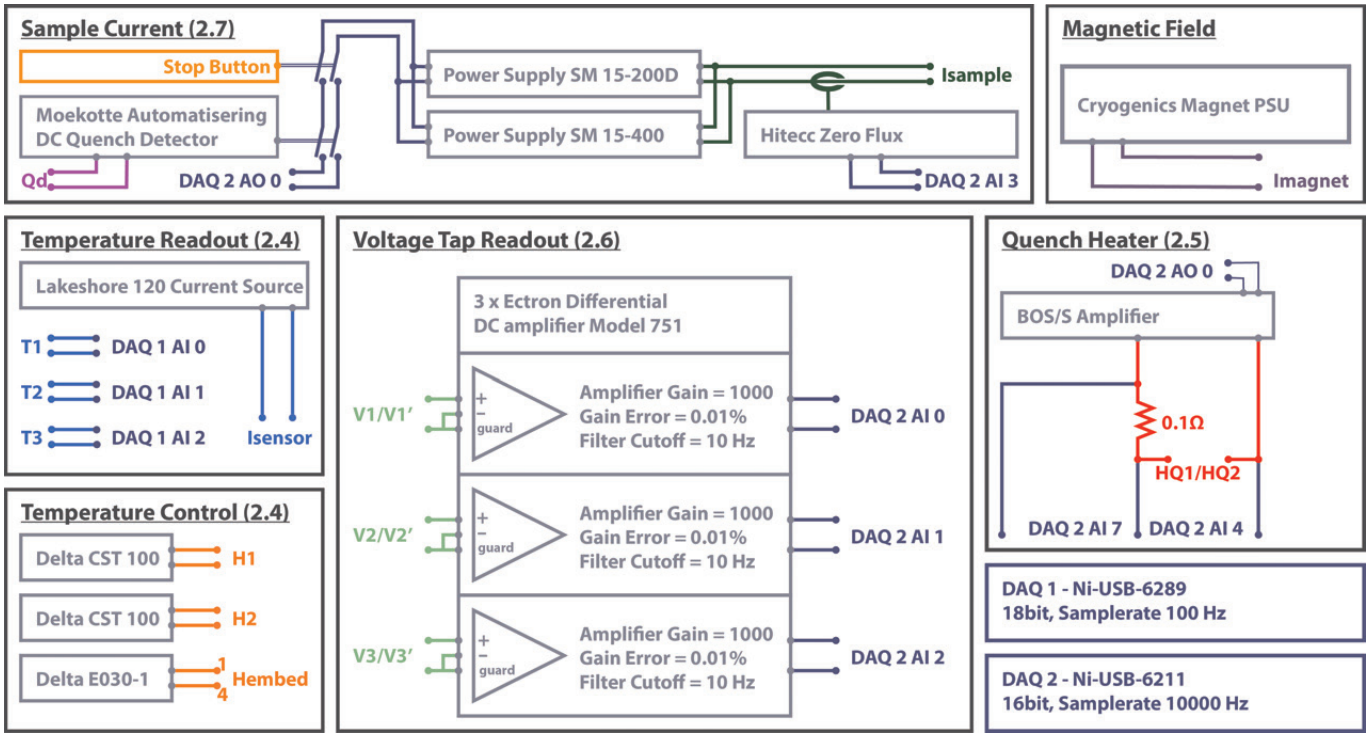

Figure 2.3: Schematic overview of the instrumentation used to control the NZP experiment. The various functional blocks are described in more detail in the Sections that are indicated.

Wire Pair	Pin	Description	Abbreviation	$R_{T=293\ K}$ [Ω]
0		Quench detector	Q_d	0
00		Quench detector backup		N.C.
1	1-2	Current for temperature sensors	I_{sensor}	150
2	3-4	Current for heater 1	H_1	20
3	5-6	Current for heater 2	H_2	20
4	7-8	Current leading to embedded heater 1-2	$H_{embed,1-2}$	10
5	9-10	Current leading to embedded heater 3-4	$H_{embed,3-4}$	14
6	11-12	Current for quench heater	H_Q	15
7	13-14	Voltage of quench heater	H_Q	15
8	15-16	Spare		N.C.
9	17-18	Spare		N.C.
24		Voltage of temperature sensor 1	T_1	50
25		Voltage of temperature sensor 2	T_2	50
27		Voltage of temperature sensor 3	T_3	50
22		Voltage tap 1	V_1	shorted
23		Voltage tap 2	V_2	shorted
32		Voltage tap 3	V_3	shorted
21		Voltage tap 1 accent	V_1'	shorted
26		Voltage tap 2 accent	V_2'	shorted
31		Voltage tap 3 accent	V_3'	shorted

Table 2.1: Overview of all wire pairs running from the instrumentation cabinet to the sample holder (for future reference the resistances are given for the connected components at room temperature and for the configuration used for the YBCO sample). The abbreviations in the one-before-last-column are used in the schematic overview of the instrumentation (Figure 2.3) and schematic sample layouts (Figures 2.4 and 2.6).

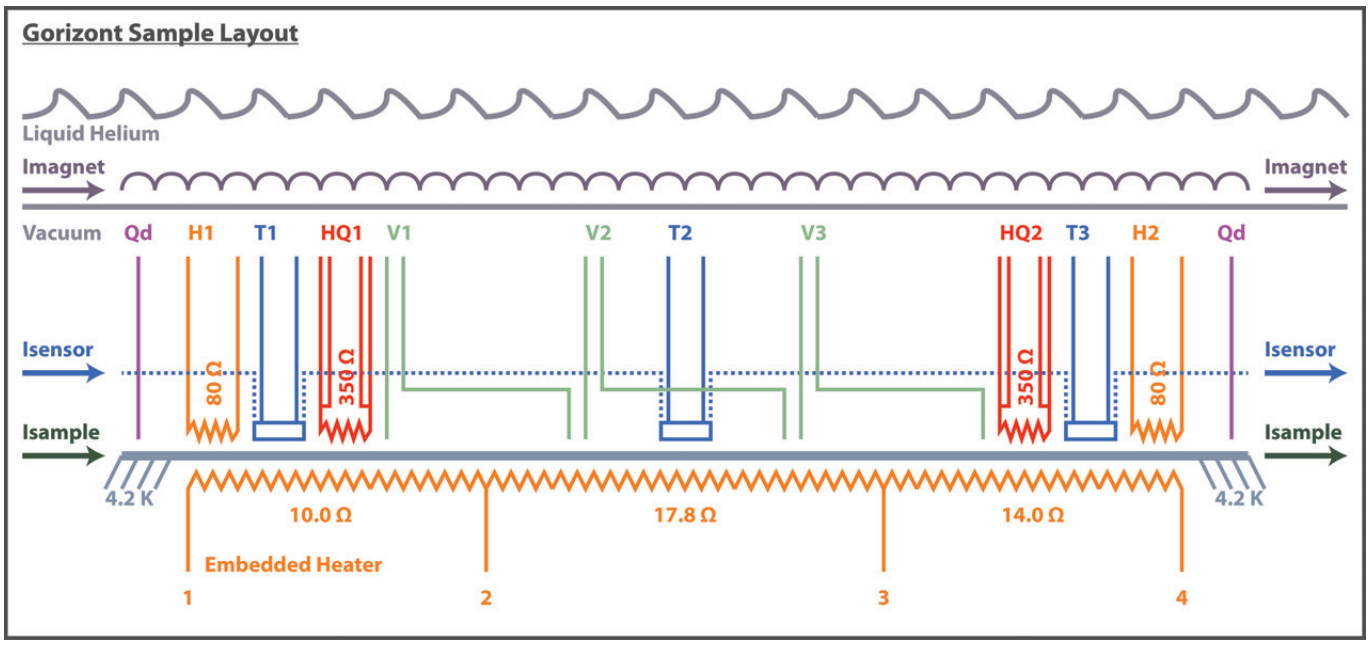

Figure 2.4: Schematic overview of the electric and thermal connections on the sample holder of the NZP experiment in the configuration that is used for Gorizont tape. The abbreviations naming the components and their respective wire pairs are explained in Table 2.1.

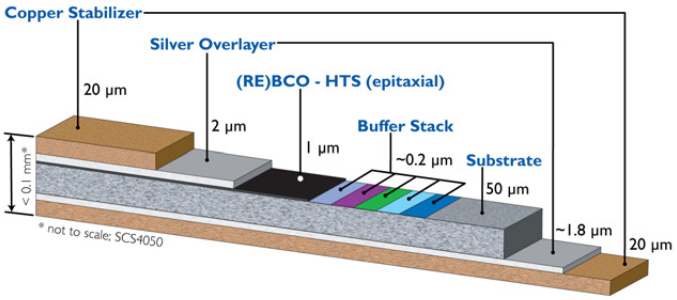

Figure 2.5: Schematic of the cross section of a SCS4050 YBCO coated conductor as provided by SuperPower.

Material	Layer Thickness
Copper stabilizer	20 μm
Silver overlayer	2 μm
YBCO	1 μm
Buffer stack	$\sim$ 0.2 μm
Hastelloy® C-276	50 μm
Silver overlayer	1.8 μm
Copper stabilizer	20 μm

Table 2.2: Material composition of SuperPower SCS4050 YBCO coated conductor.

2.3 YBCO Coated Conductor Sample Layout

The sample measured is provided by SuperPower and is a YBCO coated conductor (SCS4050) with a width of 4.04 mm and a thickness of 96 μm. The thickness and material composition of each of the individual layers is presented in Figure 2.5 and Table 2.2. The YBCO layer is fabricated using the Metal Organic Chemical Vapour Deposition (MOCVD) process, which is the default method used by this manufacturer. The conductor is stabilized using a 20 μm thick copper external cladding that fully surrounds it. The critical current density of this tape in the magnetic field and temperature range relevant for this work, was also measured at CERN in 2011 [29, 30].

Through trial and error it is found that in contrast to the Gorizont tape, quench propagation in YBCO coated conductor is relatively sensitive to added thermal capacity on the tape. This not only affects the measurement of the normal zone propagation velocity, but can even stop the development of a full quench, long enough to cause a local burnout of the sample. The trigger level of the quench detector is set to a threshold voltage, which roughly corresponds to a certain normal zone length. If the quench is 'caught' between two components acting as heat drains and the length of the normal zone is not sufficient to set off the quench detector, the tape will heat up locally causing it to burn out. To avoid this problem entirely the quench heater is placed at the center of the tape surrounded by three voltage taps on each side (See Figure 2.6). Because the quench propagation velocity in YBCO is significantly lower compared to the Gorizont tape, it is necessary to place the voltage taps at a distance of 5 mm of each other. On the other hand, in order to still maintain the sensitivity required to measure the critical current, the voltage taps had to be at least 50 mm in length. Both requirements can still be met by overlapping the voltage taps. The first voltage tap is placed at a distance of 10 mm from the quench heater, which has a length of 6 mm, making the length of the normal zone 26 mm when it enters the first voltage tap. Unfortunately this configuration does not allow positioning a temperature sensor at the center of the tape. To keep the temperature sensors as central as possible only two thermometers are placed in between the voltage taps. Next to the thermometers, also inside the voltage taps, two heaters are placed that fine tune the temperature. It should be noted that all electrical connections near and on the sample, are made using a 0.1 mm thick manganin wire, in order to keep the experiment as adiabatic as possible.

During the measurements it is found that the YBCO coated conductor samples are vulnerable to Lorentz forces pointing inwards towards the sample holder, the direction commonly used with coil-shaped samples resulting in damage to the conductor. The damage is either caused by the sample being pressed into the ridge pattern or if the tape is not mounted tight enough, by local buckling of the sample under the compressive forces (see Figure 2.7). To remedy the problem it is decided to reverse the Lorentz force and to let it point in the outward direction. To make sure that the samples in this new configuration are not torn apart under the Lorentz force, the hoop stress in the sample is verified using

$$\sigma_{hoop} = \frac{r_{sh}(I_{op} \times B)}{\tau_{sample} \cdot w_{sample}}, \tag{2.1}$$

where σ_{hoop} is the hoop stress in Pascal, r_{sh} is the radius of the sample holder, I_{op} the current in the sample, B the magnetic field, τ_{sample} the sample thickness and w_{sample} the sample width. A generally accepted hoop stress for coil

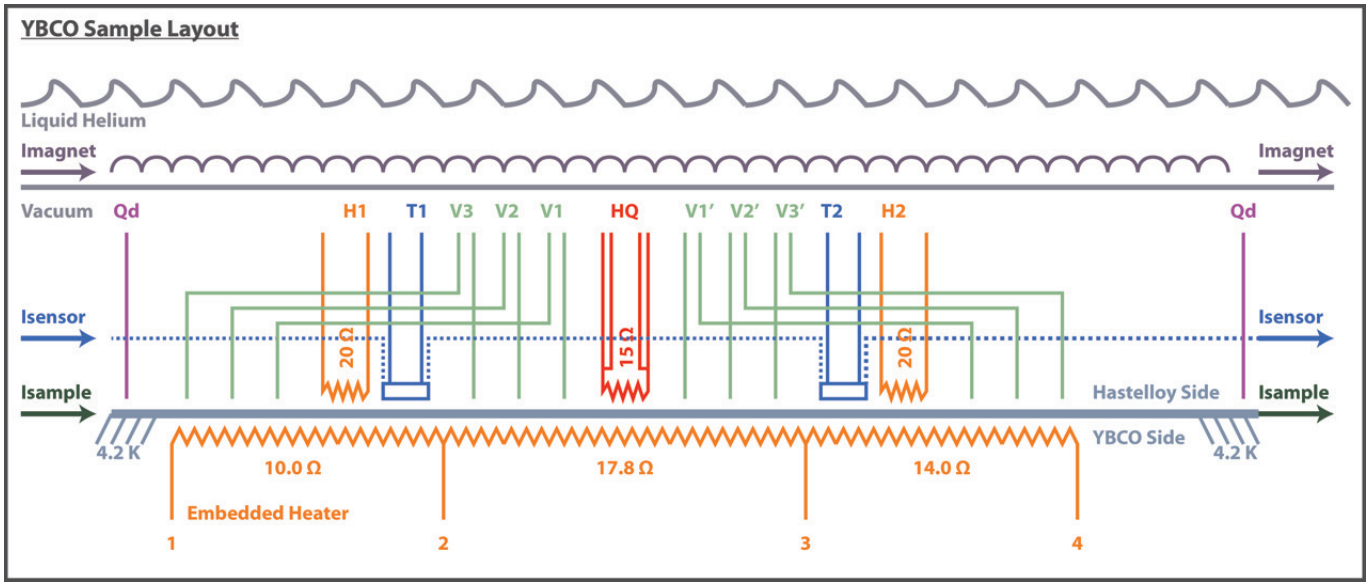

Figure 2.6: Schematic overview of the electric and thermal connections in the sample holder of the NZP experiment in the configuration used for YBCO tape. The abbreviations naming the components and their respective wire pairs are explained in Table 2.1.

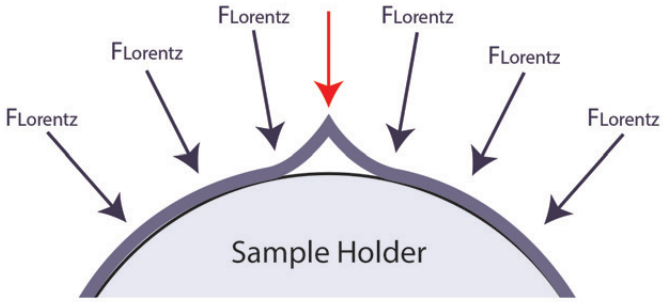

Figure 2.7: Schematic showing the buckling of a loosely mounted tape under the Lorentz force pointing inwards towards the sample-holder. The cusp at the red arrow denotes where the YBCO layer breaks.

design with YBCO coated conductor is about 300 MPa. For a sample holder with radius 16 mm and a magnetic field of 14 T, this value is reached at approximately 520 A. However, it has been reported in literature that some YBCO tapes are even able to handle stresses up to 700 MPa [31].

2.4 Temperature Control

For the measurement of quench propagation and especially when measuring YBCO coated conductor, it is of importance to perform the experiment as adiabatic as possible. Thermal convection can be reduced to nearly zero by performing the measurement in vacuum. The vacuum (see Figure 2.1, VIII) is achieved by pumping on the setup with a Hi-Cube pumping station from Pfeiffer for at least two nights to a pressure below 0.005 Pa. To check for leaks, after the pump is turned off, the pressure is measured as function of time. Even if no leaks are present the pressure still rises due to out-gassing. An acceptable rate for the pressure to rise is determined to be below 0.03 Pa/min. After the sample is lowered into the liquid helium any particles still present in the vacuum space would freeze to the walls. This phenomenon is called cryo-pumping and helps to maintain the vacuum. The remaining thermal contact of the sample to its environment can be split into the following three thermal paths:

1. the thermal conduction through the nylon of the ridge pattern on the surface of the heater.
2. thermal radiation to the embedded heater which is heated electrically and cooled by the helium from the inside.
3. thermal radiation to the wall of the vacuum chamber which is cooled from the outside to 4.2 K.

When the temperature of the sample is stable there is a balance between these three conduction terms. When the balance is disturbed, by for example a change in the current of the embedded heater, the temperature changes until the balance is restored. The settle time of this system is determined to be at least 240 s (for the new heater), which far exceeds the

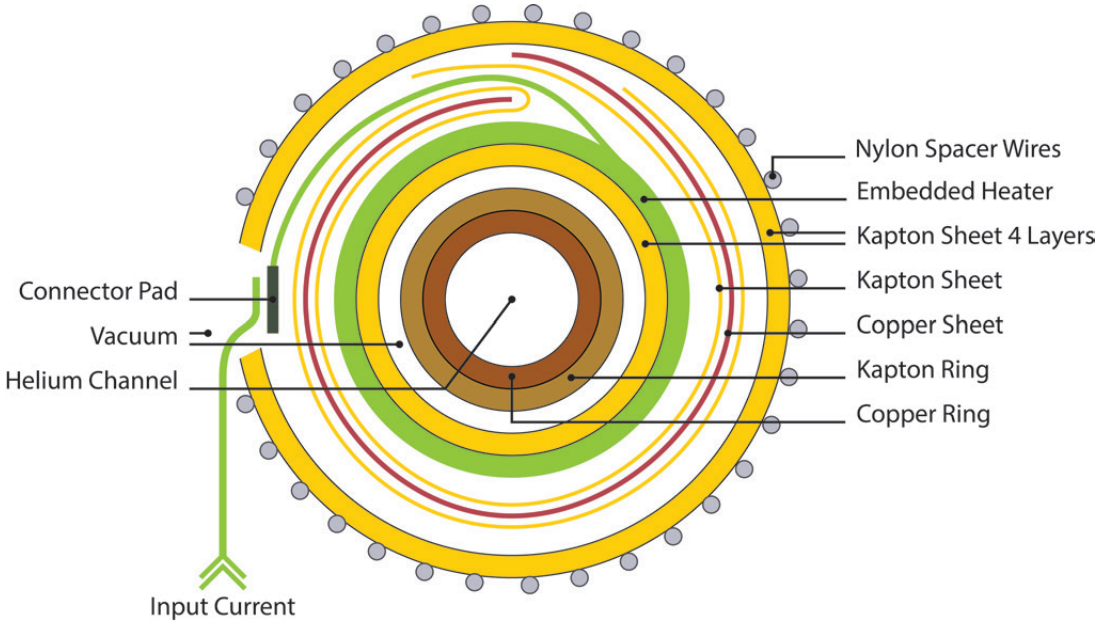

Figure 2.8: Cross section of the design of the new embedded heater roll. All layers are held together with clear epoxy. Note that the layer thicknesses are not to scale.

N	Material	#	Thickness	Sub-total
0	Former	1	14.25 *mm*	14.25 *mm*
1	Kapton	4	0.07 *mm*	0.28 *mm*
2	Phosphor Bronze	1	0.2 *mm*	0.2 *mm*
3	Kapton	1	0.07 *mm*	0.07 *mm*
4	Copper Sheet	1	0.1 *mm*	0.1 *mm*
5	Kapton	5	0.07 *mm*	0.35 *mm*
6	Nylon Ridges	1	0.1 *mm*	0.1 *mm*

Table 2.3: Layer composition of the embedded heater (from inside to outside).

time duration of any quench, proving that the thermal insulation of the sample from its surroundings is within reasonable levels (see also the footnote on Page 9 and the discussion in Appendix B).

Because the current leads of the original embedded heater are broken at the entry point into the Kapton (polyimide), it is necessary to construct a new one. To avoid the wires from breaking again in the new heater, the entry point is now designed with connector pads. If a wire breaks it can relatively easily be re-soldered to the heater. Also added to the heater is a layer of copper sheet material. The idea behind this is to spread the heat from the heater more evenly across its surface area. Whether this is a good idea or not is still under discussion, because it is found that the temperature is spread so homogeneously, that it does not matter which section of the heater (see Figure 2.6) is used for the heating. This results in less control over the temperature profile of the tape. A schematic of the embedded heater showing the entry of the current leads past the copper layer is presented in Figure 2.8. The thickness and material composition of the embedded heater is given in Table 2.3. For a step-by-step construction protocol for the heater, the reader is referred to Appendix A. Because the new embedded heater turned out to be thicker than the previous one, due to the extra copper layer, it is necessary to make a copper ring increasing the diameter of the top flange, and also a new copper ring to extend the bottom flange over the heater. The current of the embedded heater is supplied by a Delta E030-1 current source, which is capable of a maximum current of 1 A and a maximum voltage of 30 V. In order to decrease the sensitivity of the knob, it is useful to control the voltage, instead of the current. In addition to the embedded heater, two extra heaters H_1 and H_2 are used to level out the temperature of the sample near the copper flanges that form the current leads. These flanges are in direct contact with the internal He reservoir and thus constitute an important heat drain. In the case of the Gorizont tape, 80 Ω metalfilm resistors are used. In the case of the YBCO samples two SMD power resistors type 3521 with a resistance of 20 Ω are bonded to the sample using an alumina loaded epoxy. These heaters are similar to the quench heater (see Section 2.5). The current through the heaters is supplied by two Delta CST 100 current sources, with a maximum current of 100 mA.

The temperature of the sample is monitored using CERNOX temperature sensors, which are provided with a calibration curve by the manufacturer Lakeshore. For the experiment on the Gorizont tape the thermometers used are $X31553$, 12185 and $X31554$ for T_1, T_2 and T_3 respectively and for the experiment on YBCO tape $X31553$ and $X78396$ for T_1

and T_2 respectively. Before the thermometers are used, they are tested in liquid Nitrogen and in liquid Helium. The thermometers are fixed to the sample using a short square copper tube, which is soldered to the tape. The thermometer resides inside the copper tube and is kept in place using a short length of string (see Figure 2.9). The thermal connection between the thermometer and the copper is improved by adding some thermal grease. The current leads to all sensors are connected in series to reduce the number of wire pairs required. The measuring current is supplied by a Lakeshore 120 current source. Because the voltages coming from the thermometers are read directly by one of the data acquisition cards without pre-amplification, it is necessary to use a measuring current of 300 μA instead of the recommended 10 μA, in order to get an adequate signal-to-noise ratio. Initial tests comparing the CERNOX resistance values obtained with different measuring currents showing that this relatively high current level does not affect the values for the temperature due to self heating. The software transforms the voltages into temperatures using the provided calibration curves (which are given in Appendix C).

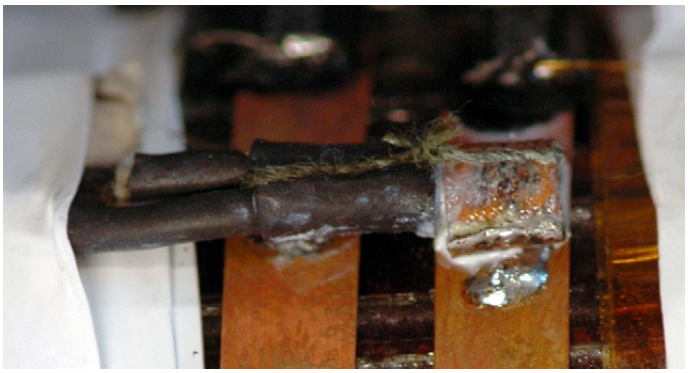

Figure 2.9: Photograph of the thermal anchoring of a Lakeshore CERNOX thermometer to the sample, in this case a YBCO coated conductor.

2.5 Quench Initialization

One of the problems encountered is the design of an adequate quench heater. In the past a piece of manganin wire is simply wound around the sample. By applying a low temperature varnish the wire is fixed thermally to the tape. For the measurement on the Gorizont tape such a configuration was also used and it was noted that the minimal quench energies were non-reproducible. This lead to the conclusion that the heater was in bad thermal contact with the tape. Furthermore, the sharp edges of the tape tended to damage the electrical insulation of the manganin wire resulting in electrical shorts. Therefore it is necessary to come up with a new and more robust heater design. The solution found is to bond a surface mounted ceramic SMD power resistor type 3521, with a resistance of 15 Ω, to the tape with an alumina loaded epoxy (see Figure 2.10). The dimensions of this SMD resistor are 3.2 *mm*, 0.55 *mm* and 6 *mm* for the width, thickness and length, respectively. The heater configuration is tested repeatedly in liquid nitrogen on a YBCO test sample with up to a maximum pulse energy of 1 *J* deposited in 100 *ms*. To test if the heater can cause damage to the sample through differences in thermal expansion, the sample and its heater are thermally cycled at least 20 times from room temperature to liquid nitrogen temperature and back. The critical current of the YBCO sample is measured before and after this test. In both cases the I_c value of the test sample at zero field and 77 K is found to be around 115 A, confirming the absence of degradation.

To determine the energy dissipated by the heater, it is connected in a four-point configuration, allowing the voltage over just the heater to be measured. The current to the heater is supplied by a Bipolar Operational Source / Sink (BOS/S) amplifier, which is set to amplify the voltage at its input by a factor of two. The input signal of the amplifier is provided by the output of the Data AcQuisition card (DAQ). For the initialization of the quench a single square pulse is used, the peak value and width of which can be adjusted. The offset of the amplifier is compensated for by the software. The maximum output of this amplifier is 20 *V* and 20 *A*. Because the voltage input limit of the DAQ card is only 10 *V*, it is necessary to measure the voltage over the heater through a voltage divider consisting of two resistors, each with a resistance of 28 *k*Ω. Inside the software the voltage is doubled again. The current through the heater is determined by measuring the voltage over a 0.1 Ω shunt resistor. The energy deposited by the pulse in the heater is then determined with

$$E_{pulse} = \int_0^\infty U \cdot I dt, \tag{2.2}$$

where U is the voltage over the heater and I is the current through it. By increasing the pulse height with increments of 0.1 *V*, until a quench occurs, the quench energy can be determined. This method proved to be much faster than seemingly smarter search algorithms, because the reset time after a quench is much longer than the reset time after a

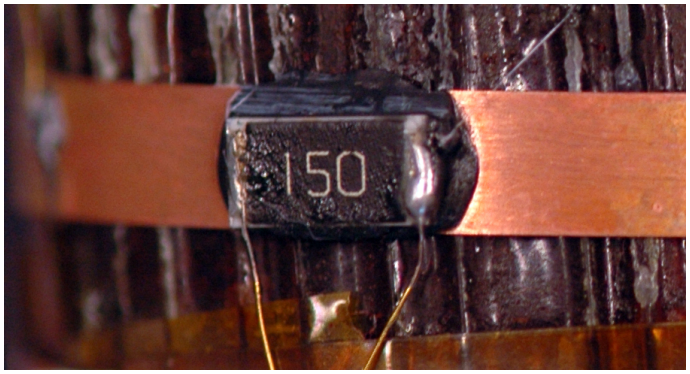

Figure 2.10: Photograph of the quench heater with manganin current leads stuck to the YBCO tape using an Alumina loaded epoxy.

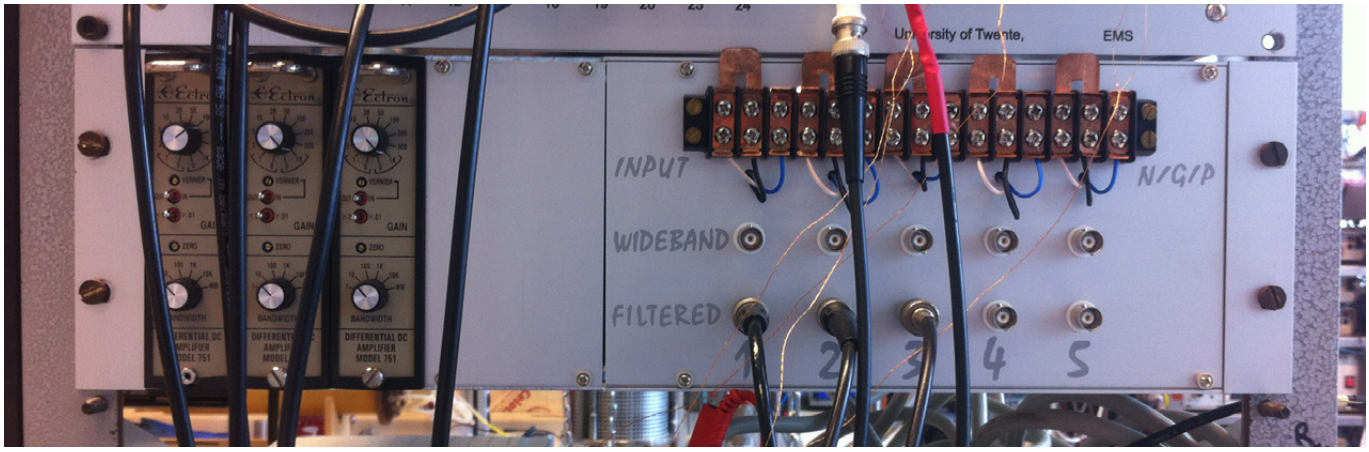

Figure 2.11: Photograph of the front panel of the enclosure constructed to accommodate a total of five Ectron 751ELN DC-amplifiers.

pulse that does not result in a quench. If the quench energy needs to be determined at multiple values of the current, it is best to start at the highest current, because each time the current is lowered, the quench energy increases slightly, making the next value of the quench energy predictable. This reduces the number of steps required to find it.

2.6 Voltage Readout

The voltage taps serve two purposes. First they are used to measure the critical current of the sample. Secondly they are used to measure the normal zone propagation. This means that the measurement system needs to be fast but also sensitive. Therefore the voltage is pre-amplified using three Ectron 751ELN DC-Amplifiers [32], assembled in a new enclosure (see Figure 2.11). In order to extend the experiment in the future to five voltage taps, the new enclosure provides five slots for amplifiers of which three are currently used. To avoid thermally induced voltages over the input terminals, only copper-to-copper connections are used. All wiring between the terminals and the amplifiers is electrically shielded and is kept as far away as possible from the main voltage lines that provide the amplifiers with power. The amplification factor of the amplifiers is set to 1000× and the low pass input filter to 10 Hz. During the measurement of quench propagation it is sometimes necessary to reduce the amplification factor of the first amplifier to 100×, to avoid clipping of the signal.

The amplified voltage is measured using one of the DAQ cards, which samples at a frequency of 10 kHz. Inside the software the electric field is determined by

$$E = \frac{U}{f_{amp}\ell_{vt}}, \tag{2.3}$$

where U is the measured voltage by the data acquisition card, f_{amp} is the amplification factor and ℓ_{vt} is the length of the voltage tap. During the measurement of the critical current noise is reduced further by taking the time average of the electric field over the last 0.25 s.

Sample Current	LP-Filter	Gain (fixed)	Trigger
$0 - 50\ A$	$1\ Hz$	250	$9.0\ V$
$50 - 150\ A$	$1\ Hz$	250	$8.0\ V$
$150 - 300\ A$	$1\ Hz$	250	$6.0\ V$
$300 - 400\ A$	$10\ Hz$	250	$2.0\ V$
$400 - 500\ A$	$10\ Hz$	250	$0.8\ V$

Table 2.4: Quench detector settings. Note that these settings are just a guideline.

2.7 Quench Protection and Current Control

The current through the sample is provided by a Delta SM 15-400 current source which can deliver a current of 400 A. For measurements at higher currents an additional Delta SM 15-200D is connected in parallel for an extra 200 A [2]. The sample current is measured with a HITEC zero flux probe which can measure up to 2000 A. The output of the probe is connected directly to one of the DAQ cards. During the measurement at 14 T it is discovered that the Nb_3Sn current leads have a critical current of 440 A, placing an upper limit on the sample current at this magnetic field. Also at lower magnetic fields, without helium gas flow cooling of the current leads, continuous currents above 500 A cause serious vaporization of helium.

To avoid burnout of the sample it is necessary to regulate the current to zero before it overheats. The sample is protected against burnout using three independent mechanisms:

1. *Hardware quench detection:* A Moekotte Automatisering DC Quench detector is connected to detect voltage build-up over the current leads. When it reaches a pre-set trigger level it breaks the connection of the control voltage to the power supplies (see also Figure 2.3). Note that the current leads are also protected against quenches through this mechanism.

2. *Software quench detector:* If the voltage of all three voltage taps exceeds a certain trigger level, then the software automatically sets the control voltage of the power supplies to zero.

3. *Timed current shutdown:* If the software reaches the end of the predefined time frame after a heat pulse, then the software automatically sets the control voltage of the power supplies to zero (also see Section 2.8).

During the measurement when a quench occurs in almost all cases the first mechanism is the first to react. Therefore the trigger level of the quench detector has to be tuned with care. The trigger level of the quench detector is defined using

$$|(U_{in} - U_{offset})A_1A_2| > U_{trig}, \tag{2.4}$$

where U_{in} is the voltage at the input of the quench detector, U_{offset} is the voltage set to compensate for the offset of the amplifiers, $A_1 \cdot A_2$ is the gain of the internal amplifiers and U_{trig} is the trigger level. If this expression is true the quench detector triggers and the sample current is regulated to zero. As a guideline the settings used for the quench detector are provided in Table 2.4. Also while tuning it is best to keep the temperature measured at 40 mm from the quench heater below 70 K. To prevent the quench detector from triggering due to induced voltages, the ramping of the sample current is performed at a maximum rate of 30 A/s.

2.8 Software

The software created for the data acquisition system is written with Labview, which is a graphical programming environment developed by National Instruments. The communication between Labview and the data acquisition cards is provided through the NiDAQmx library. The code consists of eleven major WHILE loops, each with its own specific task, that run in parallel. The data is transferred between the loops using global variables (something that is unavoidable when programming multi-threaded code in Labview). A global description of the WHILE loops and their tasks is given below:

1. *DAQ 1 Read Cycle* - This WHILE loop reads all acquired data from DAQ 1, which measures the voltages from the temperature sensors, applies the calibration curves and stores the data in the global memory.

2. *DAQ 2 Read Cycle* - This WHILE loop reads all acquired data from DAQ 2, which measures the voltages from the Ectrons, from the zero flux, from the quench heater and from the shunt resistance of the quench heater. Inside the loop the measured values are compensated for the amplification factors. The resulting data is stored in global memory.

[2] For the measurements also a 1 kA Heinzinger power supply is available. However, because of the analogue electronics inside, this power supply reacts relatively slow when the current is regulated to zero after a quench is detected and therefore two faster power supplies were used in parallel.

3. *Sample Current Cycle* - Reads the required current from a global variable and writes it to the output channel of DAQ 2.

4. *Ic Measurement Cycle* - When activated this cycle performs the measurement of the critical current, by slowly ramping the required sample current and matching the current measured by the zero flux with the measured electric fields. The time delay between the acquisition of data points can be set manually.

5. *Ic Fitting Cycle* - When a refit is requested this cycle fits the measured EI-curve using a least square fit.

6. *Pulse Cycle* - When activated this cycle fires a pulse to the quench heater and stores the measured electric fields, the sample current, the voltage over the quench heater and the current through the quench heater, during and after the pulse in global memory.

7. *Quench Detection Cycle* - Detects when all three electric fields are over a certain trigger level. If this is the case it sets the required current to zero and stops the measurement of the critical current if it is running.

8. *Matlab Data I/O Cycle* - When activated this cycle writes all acquired data for both the critical current measurement and the pulse measurement to a specified Matlab data file. This cycle uses a third party library called MatIO which is freely available through the VI package manager.

9. *Current Setting and Ramping* - Controls the ramping of the current by gradually changing the requested target current.

10. *Real time plotting* - Handles the graphical representation of the temperatures.

11. *Error Handling and Stopping* - If an error occurs in any of the WHILE loops this cycle sends a 'stop flag' to each of the other WHILE loops.

Chapter 3 Results

In this chapter the results from the measurements on the YBCO coated conductor are presented. The set-up used to collect the data is described in Chapter 2. Because important parts of the set-up were replaced, it was first tested with a well characterized and robust Nb_3Sn tape. The results of this sample are concisely presented in Appendix E.

After the measurement on the Nb_3Sn tape the experimental setup was moved to the main 15 T magnet and a learning curve for the more delicate measurement of YBCO coated conductors was embarked upon. With the first YBCO sample, there was a short in the electrical wiring. This caused the voltage recordings to be noisy, probably due to a short between the different voltage taps. However when the current in the sample was increased to 200 A, the tape suddenly became resistive. It probably broke under the Lorentz force that were at this point pointing inward towards the sample holder (see Section 2.3 and Figure 2.7). After inspection no externally visible damage could be found on the tape. For all the next samples it was decided to reverse the Lorentz force by mirroring the fixation of the sample on the holder. Unfortunately the second sample was resistive right after its first cool down. After inspection serious buckling of the tape was found underneath an experimental NIMCO quench heater. This was probably caused by differences in thermal expansion between this polymer substrate heater and the tape.

The third and fourth samples both performed well in terms of critical current. However during the first propagation measurements at 35 K, the tapes burned out (see Figure 3.1). In both cases the hot spot is located between the quench heater and a nearby temperature sensor. The lessons learned from these two failures resulted in major changes in the layout of the components on the sample so that the quench would never be 'trapped' between two components (see Figure 2.6). In addition the quench protection system was improved (see Section 2.7). With the new layout, protection system and the latest version of the quench heater (a surface mounted ceramic substrate resistor), the fifth sample was mounted. This sample performed well and two datasets were acquired. The first dataset was measured in the range of $70 - 90\ \%I_c$. Because during the measurement of this dataset a minor repair was needed of the quench heater, it was decided to re-measure the earlier data to check for reproducibility and to extend the range to $50 - 100\ \%I_c$. The data that are presented in this Chapter are thus the second dataset from the fifth YBCO sample.

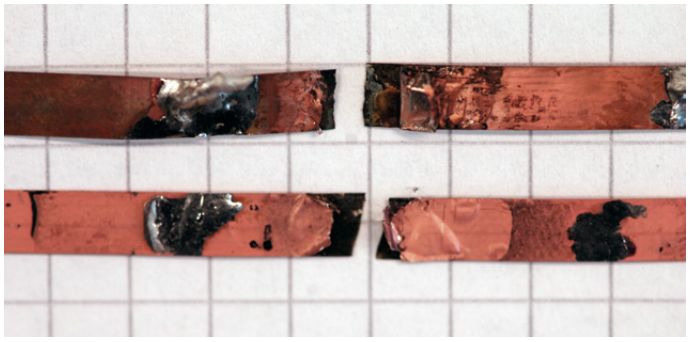

Figure 3.1: Photograph of the burned spot of samples three (top) and four (bottom).

3.1 Measurement Strategy

For the behaviour of the normal zone propagation velocity and the minimum quench energy three parameters are of interest: the sample current I, the baseline temperature T_{op} and the magnetic field B. For the first it is chosen to measure at several set percentages of the critical current, which is the conventional method with this type of experiments. The temperature and the magnetic field are varied linearly (see Table 3.1). Because the risk of sample burnout is relatively low for currents below 200 A, it was decided that in this regime the parameters can be changed in the order of increasing settling time. This is the least time- and thus helium-consuming protocol. For 14 T this 'low' current regime starts above 31 K; for 10 T above 35 K and for 6 T above 37 K. At higher currents, however, it is chosen to adjust the measurement protocol in order to minimize the risk of sample burnout, by each time performing all measurements (at various T and B values) at a given current I. After all measurements for this I-value are complete, the current is increased to a slightly

higher value. This requires the time-consuming raising and lowering of the magnetic field more often. However, it ensures that a maximum amount of data could be acquired from the sample. Also, all parameters are varied using small steps to avoid unpredictable changes in behaviour, which can possibly lead to sample damage.

name	symbol	range	start	stepsize	setting time
percentage of critical current	$\%I_c$	50-100	100 %	10 %	$\pm 10\ s$
temperature	T	$23 - 47\ K$	$35\ K$	$2\ K$	$\pm 5\ min$
magnetic field	B	$6 - 14\ T$	$14\ T$	$4\ T$	$\pm 15\ min$

Table 3.1: Parameter range for the NZP measurements. Note that the lower temperature is different for each magnetic field value.

3.2 Critical Current

Because it is chosen to measure at a certain set percentage of the critical current, it is first necessary to measure the $I_c(B,T)$ values. The critical current is determined by slowly ramping the current while measuring the resulting electric fields E between the voltage taps. All measured E data plotted against current I at all measured temperatures and magnetic fields, are presented in Appendix D. The derived I_c values as function of temperature and magnetic field are presented in Figure 3.2. Note that the critical current for all measurements is defined using the customary threshold field E_0 of 10 $\mu V/m$ and that the magnetic field is applied parallel to the tape. The N-values (the logarithmic slope of the power law-like $E(I)$ curves, see Appendix D) for all measurements are found to be in the range of 8 to 14, with a vague minimum around 37 K, which shifted slightly under the influence of magnetic field. However, this should be confirmed by more accurate measurements under more stable temperature conditions.

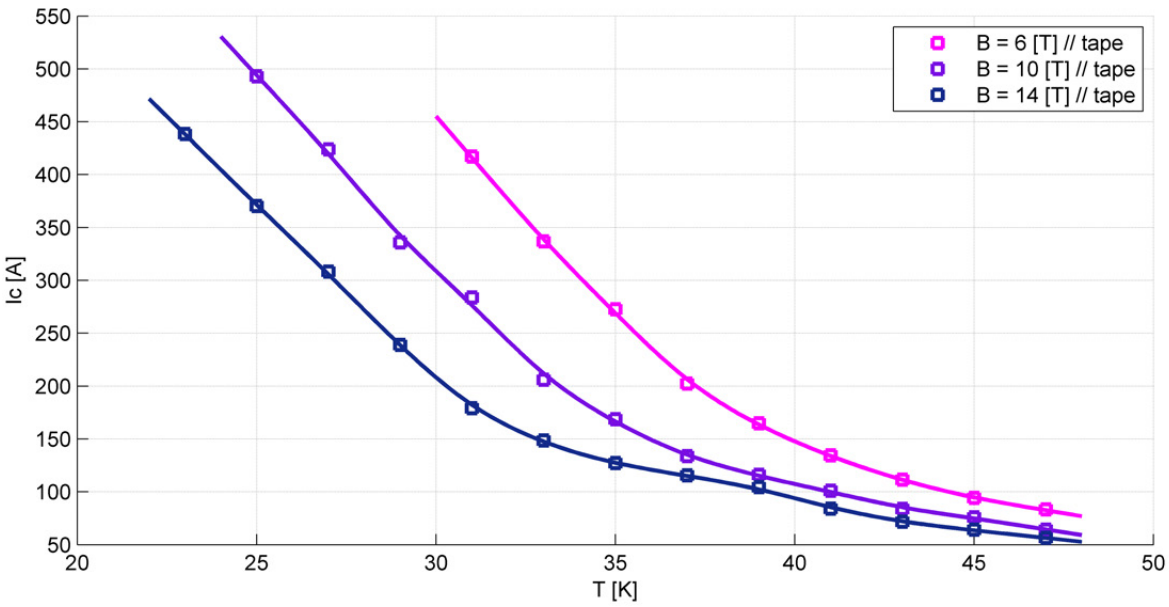

Figure 3.2: Measured critical current of tape sample SCS4050 as function of temperature and magnetic field at $B = 6$, 10 and 14 T, applied parallel to the tape. The critical current is defined at an electric field criterion of $E_0 = 10\ \mu V/m$. The EI-curves used to determine the critical current are provided in Appendix D.

3.3 Normal Zone Development

To measure the normal zone behaviour, the voltage development of the three voltage pairs after the occurrence of a quench is recorded. The next step is to derive the normal zone propagation velocities from these voltages. As an example, Figure 3.3 shows the voltage recordings of a quench at 35 K, 14 T and 90 $\%I_c$ plotted against time (note that the vertical axis is on a logarithmic scale). The increased noise level for V_1 with respect to the two other signals can be explained by the lower amplification factor chosen for the first Ectron in order to avoid clipping of the signal. The initial bump in the voltages is caused by the sudden change in current through the quench heater and its current leads, leading to induced voltages on the voltage taps. After the initial quench heater pulse, there is a slow rise in voltages, until the front of the normal zone fully enters the voltage taps at which point the voltages suddenly start to rise quickly.

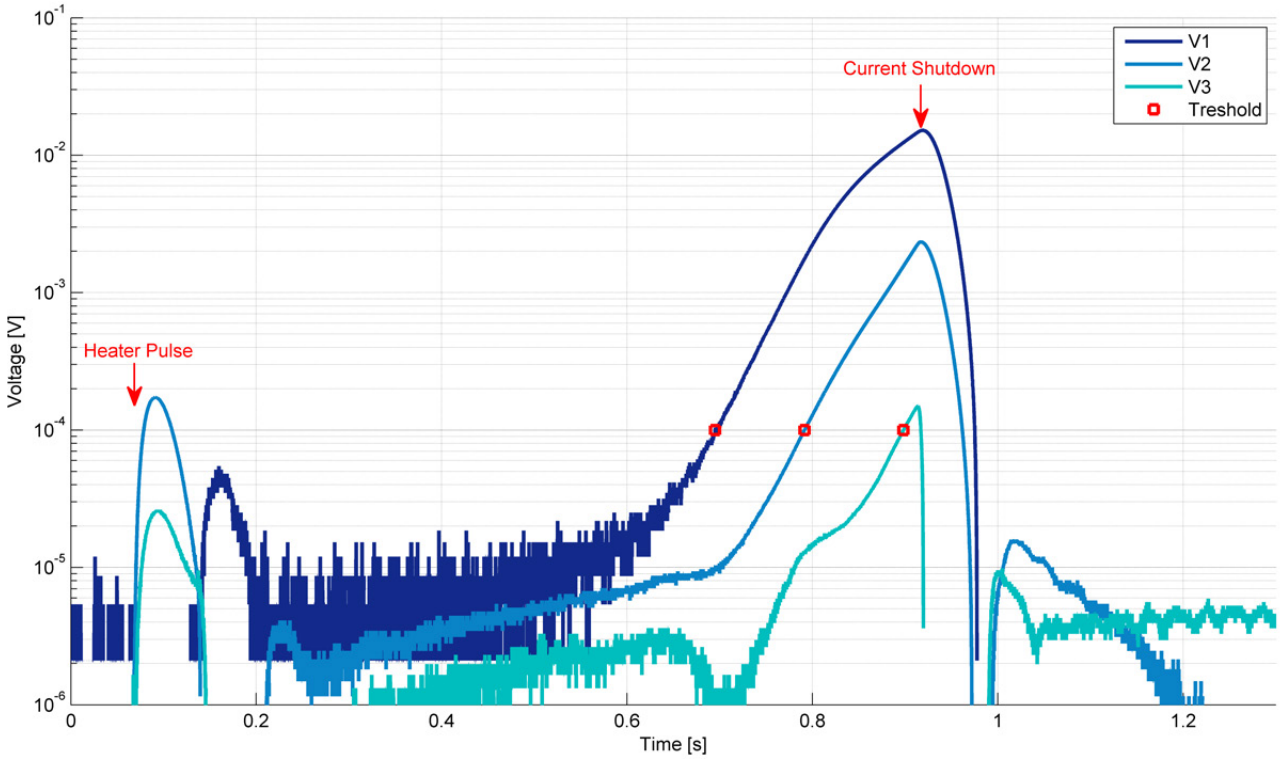

Figure 3.3: Measured voltages over the voltage taps as function of time for a quench in a YBCO coated conductor at a start temperature T_{op} of 35 K and a current I of 117.2 A, which corresponds to 90 %I_c.

To determine the normal zone propagation velocity, the time delay between the voltage profiles needs to be determined. The best results can be attained by taking a certain threshold voltage, at which the slope of the profiles is approximately equal for all three curves. For most measurements this voltage lies around 100 μV. However in some of the cases (less than 10 % of the measurements) it was necessary to adjust the threshold level slightly. From the time delays between the three voltage profiles and the distance with which the voltage taps are shifted with respect to each other, the normal zone propagation velocity is calculated. For the measurements at temperatures above 41 K it is noted that the profile of V_1, registered nearest to the quench heater, is deviating slightly from the profiles of V_2 and V_3. This is likely caused by initial transients of the quench (see the discussion of the 'minimal propagation length' in Section 4.2.2). Therefore in this temperature regime the propagation velocity is determined using only the time delay between V_2 and V_3. For temperatures below 31 K, on the other hand, the current is too high to allow the front of the normal zone to propagate all the way to the third voltage tap. This would cause the temperature recorded by T_1 and T_2 to rise above 70 K, which is the chosen safety limit (see Section 2.7). Therefore in this regime the velocity is determined using the time delay between V_1 and V_2.

For the data to be useful, it is of great importance that the determined velocities are the actual steady-state velocities of the normal zone front and not the transients related to the initial build-up of a minimum propagation length. There are two indications that this is indeed the case:

1. The voltage profiles from the successive voltage taps that are used for the determination of the velocity are nearly identical in shape but shifted in time. If they are related to initial transients, the profiles would differ in shape.

2. The time-dependent numerical computer model presented in Section 4.3.4, clearly confirms that the quench propagates at or near the steady state velocity once it reaches the position of the voltage taps.

3.4 Quench Energy and Normal Zone Propagation

In Figure 3.4 all measured data of the normal zone velocity and the quench energy are presented. To avoid overcrowding the graphs, it is decided not to include errorbars. It is estimated that the uncertainty on the normal zone propagation velocity is ±10 %. This estimate is based on the difference in velocities attained when using different threshold voltages and the uncertainty in the distance with which the voltage pairs are shifted. The plotted quench energies have been compensated for the heater efficiency[1], which was estimated to be 20% of the pulse deposited. The estimate is based on

[1] 'Heater efficiency' refers to the fact that only a fraction of the energy supplied by the pulsed power supply serves to initiate the quench. This is partly due to the fact that some heat is lost to other parts of the setup, and partly due to the fact that the normal zone may already fully develop before all the energy in the pulse is transferred to the sample heater. Heater efficiency is thus an unavoidable source of uncertainty in this type of experiment.

a numerical model that includes the thermal boundary between the sample and the heater (See Appendix F). According calculation about 50 % of the energy is dissipated inside the manganin wires, which are connected between the heater and the wire pairs of the four point measurement (note that in future experiments this should be avoided by soldering the four wires directly onto the heater). The other 30 % is lost because there is a thermal boundary between the heater and the sample, causing the energy dissipated in the heater to slowly seep to the tape. At some point the sample quenches while not all energy has been transferred yet. To model the heater behaviour, the current inside the sample was set to zero. However when a current is present in the sample, it heats up due to self-heating in addition to the heating from the quench heater. This slows down the transfer of heat from the heater to the tape even more and thus reduces the heater efficiency further, according to the model to as low as 10 % for currents of ~ 400 A. Therefore it should be kept in mind that, especially at higher currents, the minimum quench energy is significantly lower than measured. This is unfortunate, but in a practical experiment this common problem is hard to circumvent.

3.5 Current, Temperature and Magnetic Field Dependence

The data from the previous section is measured in a three-dimensional parameter space. In Figure 3.4 the data is presented in the way it is measured (as function of a percentage of the critical current $I(I_c)$). This way of presenting V_{nzp} and MQE data is common throughout literature, but since $I_c(B,T)$ is itself a function of different variables, it 'mixes' the influence of the three parameters I, B and T. In order to study the influence of each of the parameters separately it is better to represent the data in a different way. All data regarding normal zone velocity are plotted on a log-log scale against current in Figure 3.5. Surprisingly it can be seen that all data collapses on a single line. This means that within the measured parameter domain V_{nzp} depends mainly and unexpectedly on the current only. The line fitted to the data can be described by

$$V_{nzp} = 10^{P_2} I^{P_1}, \tag{3.1}$$

where P_1 and P_2 are the fitting parameters, which are determined using a root-mean-square fit, which can be found in Table 3.2. For completeness the data is fitted both at each value of magnetic field separately and for all data at once. When using the coefficients fitted for all data, the maximum deviation between the measured data and the fit is only 6 %. The power-law P_1 is nearly 1.5, which seems to be in contradiction with the analytical model prediction for V_{nzp}, presented in Section 4.2, which suggests that the velocity scales linearly with the current.

In similar fashion, the quench energy is also plotted against the sample current in Figure 3.6. It can be seen that the parametric dependence of the quench energy is less straightforward. In contrast to V_{nzp}, MQE clearly depends on all three measured parameters.

Another common way to represent the data is at fixed current levels. In order to convert the data that is measured at percentages of the critical current to the corresponding values at fixed currents, it must be interpolated. The normal zone velocities plotted at fixed current against temperature can be found in Figure 3.7. It can be seen that virtually no temperature dependence is present. This contrast to the temperature dependence of the quench energy QE, plotted at fixed currents against temperature in Figure 3.8, which clearly decreases when the temperature increases.

	Parameter Values		99 % Confidence Bounds			
B	P_1	P_2	P_{1low}	P_{1high}	P_{2low}	P_{2high}
6 T	1.490476219	-4.386905811	1.465212479	1.515739959	-4.440177616	-4.333634007
10 T	1.468625968	-4.335974025	1.450112199	1.487139737	-4.37532431	-4.29662374
14 T	1.514831278	-4.428173004	1.497925951	1.531736605	-4.462955274	-4.393390734
All	1.490855124	-4.382716184	1.47917877	1.502531477	-4.407179243	-4.358253124

Table 3.2: Normal zone propagation velocity coefficients for the tape SuperPower SCS4050.

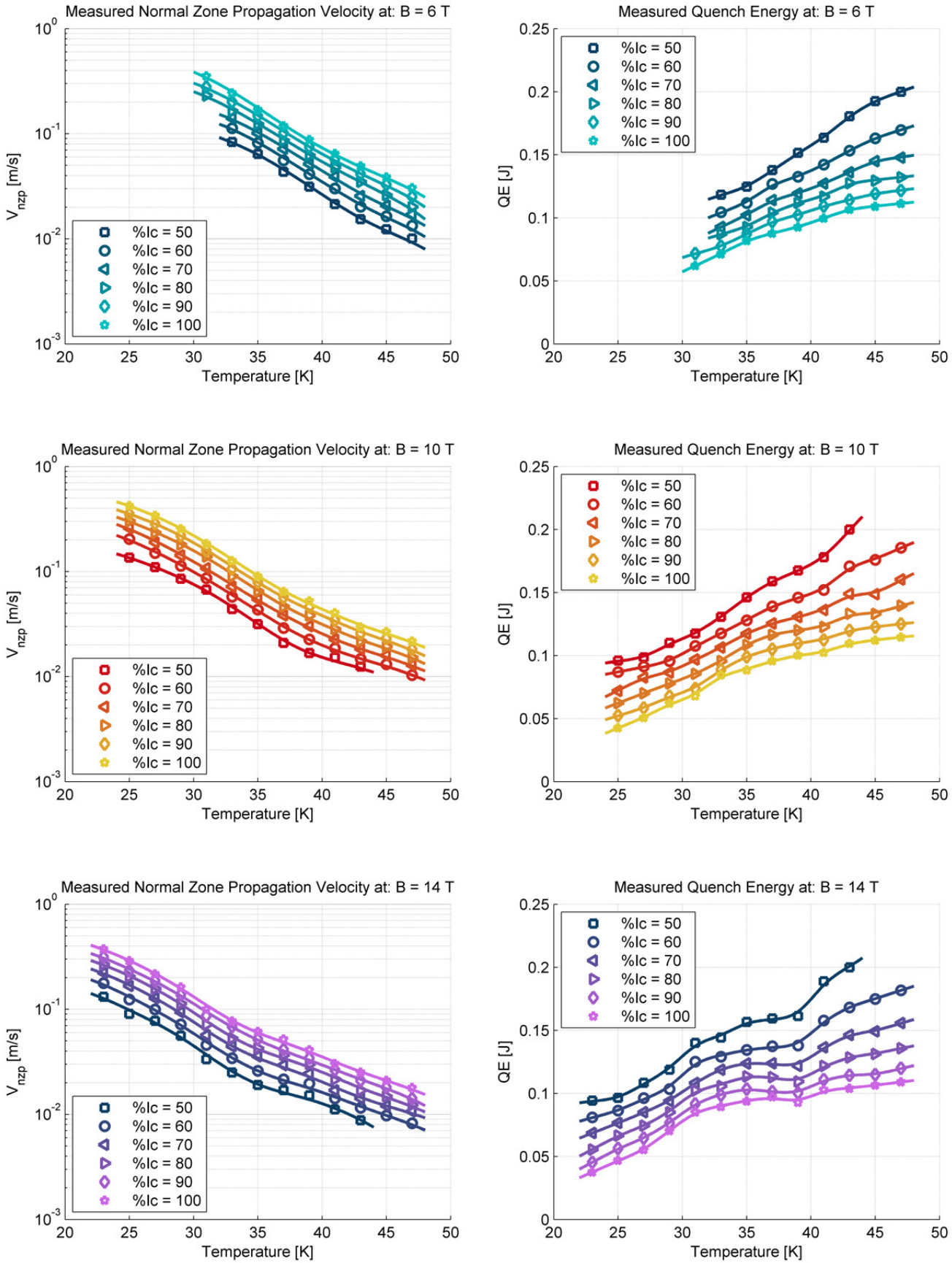

Figure 3.4: Measured normal zone propagation velocity (left) and quench energy (right) as function of field, temperature and percentage of the critical current. The data for the quench energy is compensated for an estimated heater efficiency of 20 %. Note that the normal zone velocities are plotted on a semi-log scale while the quench energies are plotted on a linear scale.

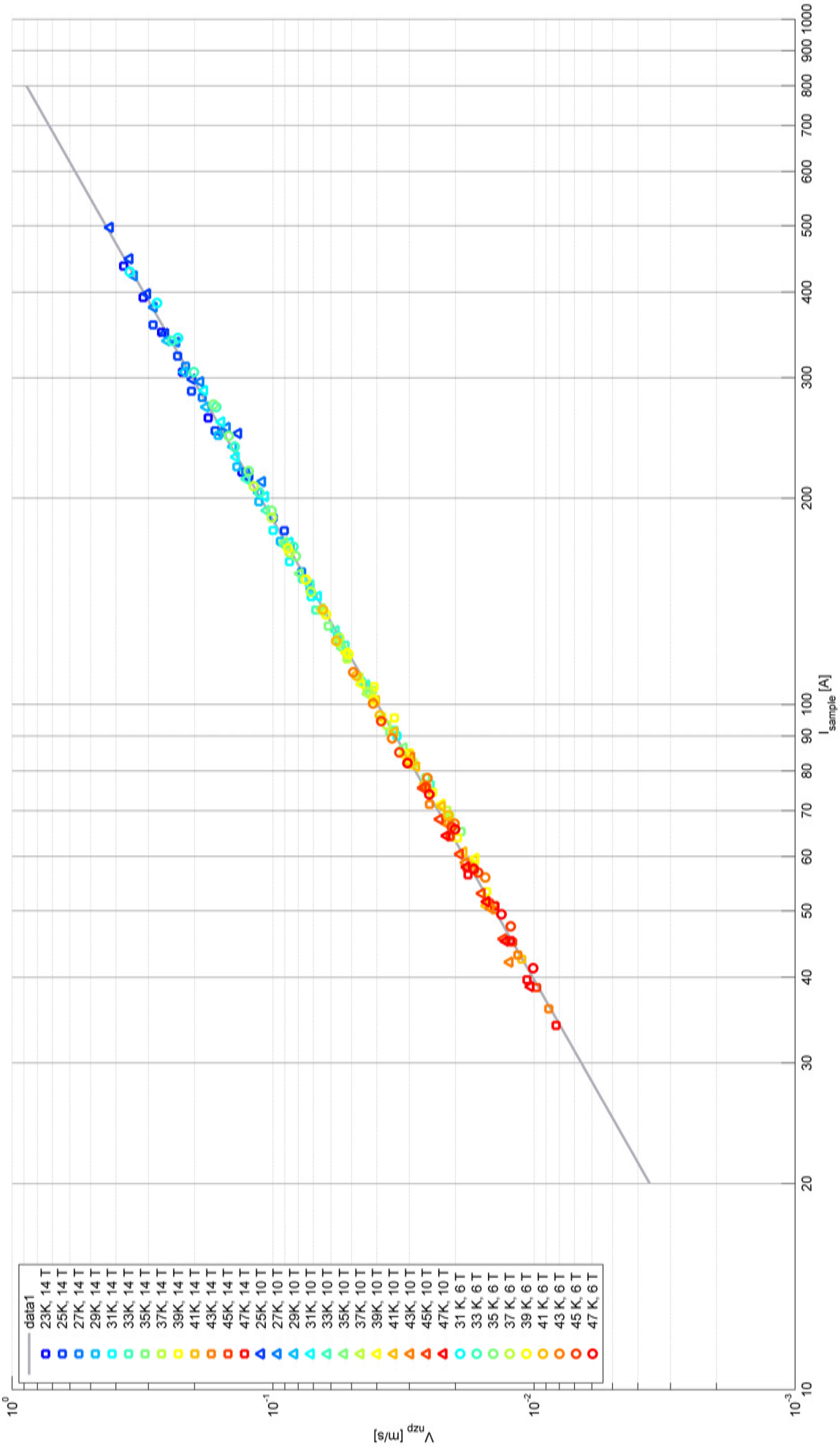

Figure 3.5: Normal zone propagation velocity plotted on a log-log scale against the sample current at all magnetic fields and all temperatures. The color of the data points denotes the temperature and the shape of the data points denotes the magnetic field magnitude. The solid line represents the power-law relation (see Section 3.5).

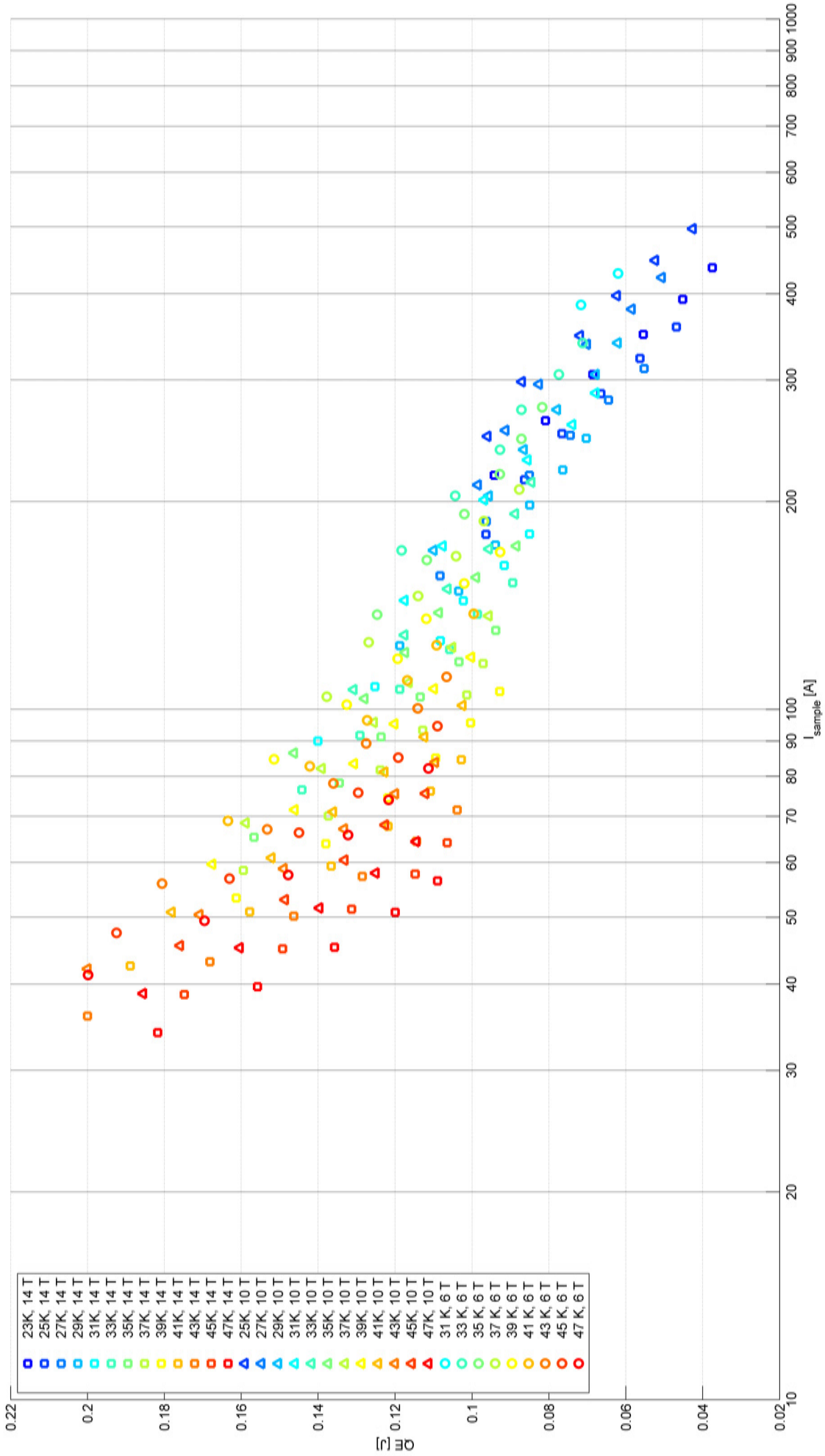

Figure 3.6: The quench energy plotted on a lin-log scale against the current at all magnetic fields and all temperatures. The color of the data points denotes the temperature and the shape of the data points denotes the magnetic field magnitude.

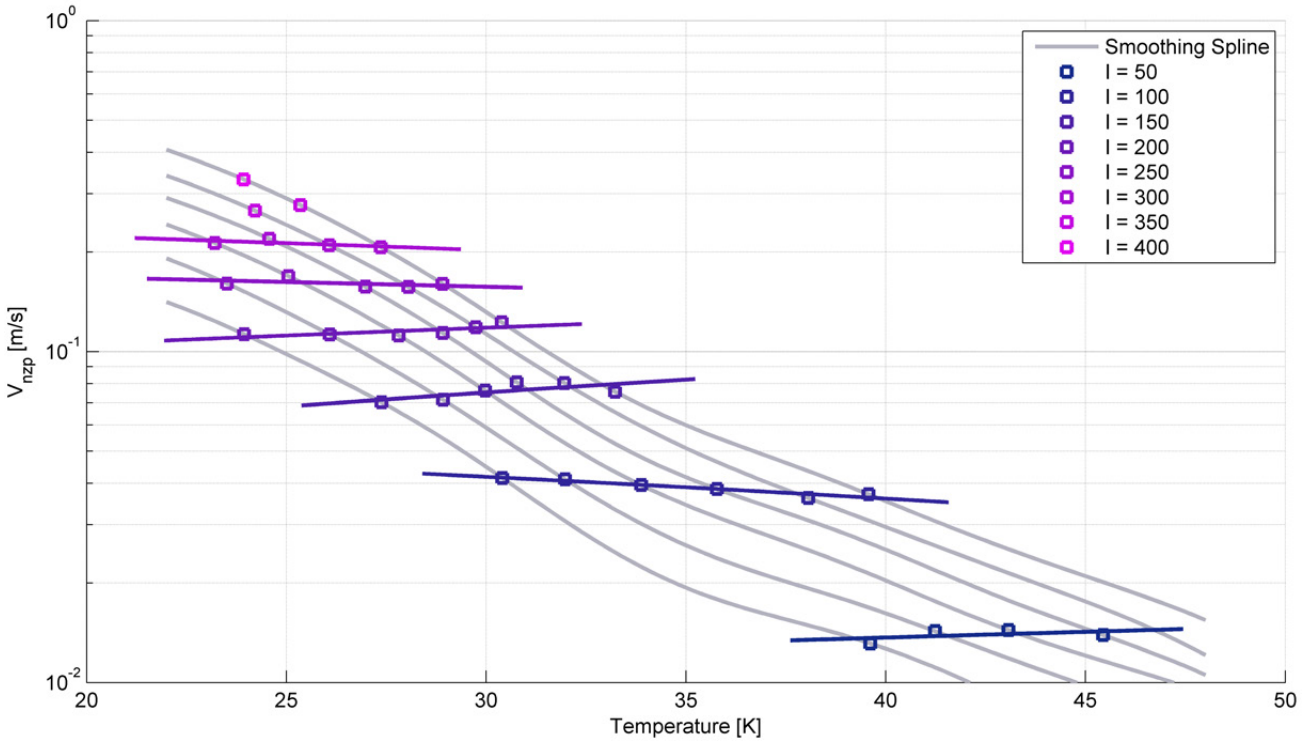

Figure 3.7: Dependence of the normal zone propagation velocity on the temperature at fixed currents and 14 T. To generate this graph the measured data presented in Figure 3.4 is interpolated using a smoothing spline visible in gray.

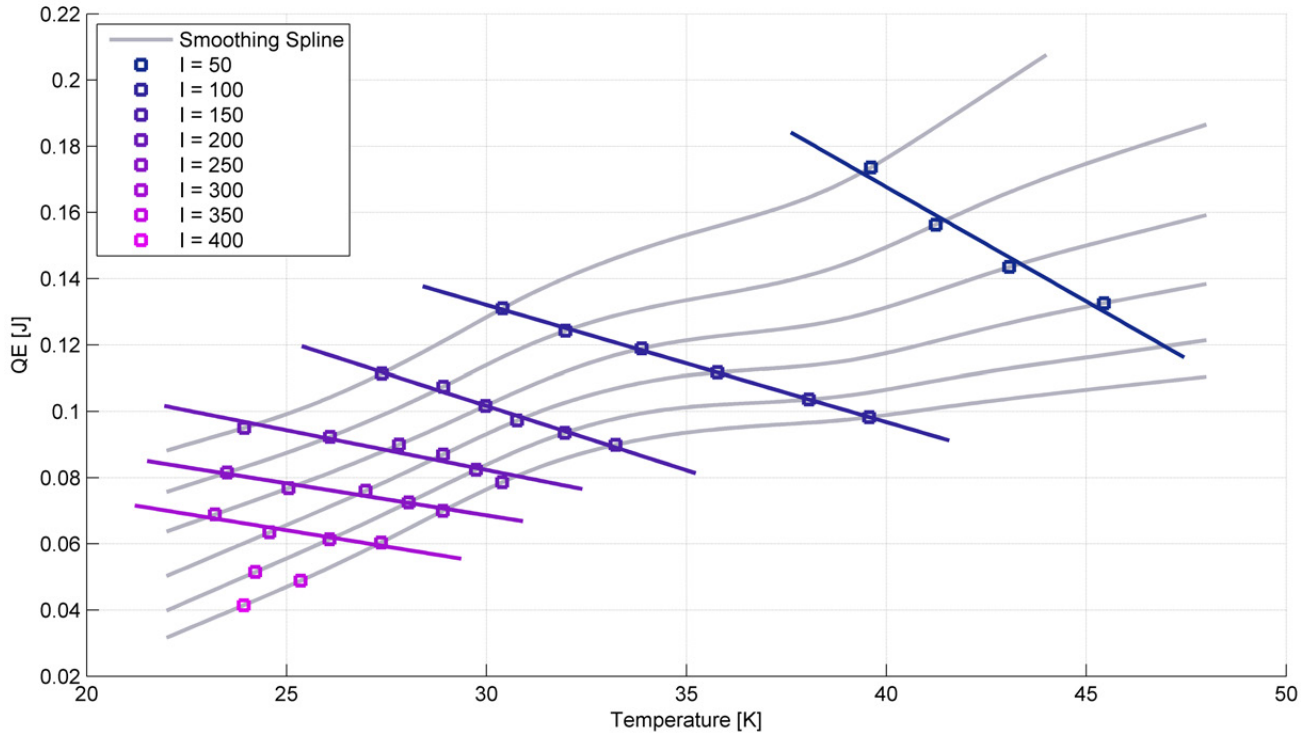

Figure 3.8: Dependence of the quench energy on the temperature at fixed currents and 14 T. To generate this graph the measured data presented in Figure 3.4 is interpolated using a smoothing spline visible in gray.

3.6 Conclusion

From the results the following conclusions are drawn:

- After an initial learning curve, the experimental setup performed well and a large dataset was produced in the temperature range of 23 to 47 K with increments of 2 K, for currents between 50 and 100 $\%Ic$ (this corresponds to a current range of 30 to 600 A), with increments of 10 $\%Ic$ and at 6, 10 and 14 T.
- Surprisingly the normal zone propagation velocity mainly depends on the current inside the sample, and hardly on B or T.
- The quench energy depends on all measured parameters.
- At 14 T the critical current of the Nb_3Sn current leads places a limit on the sample current of 440 A.

Chapter 4 Modelling and Analysis

This chapter introduces a series of analytical and numerical models of the thermal-electrical behaviour in a YBCO tape. The models were initially created to understand the development of a normal zone in LTS conductors. All models are based on the so-called heat balance equation, which is introduced in Section 4.1. They serve two purposes. The first is to provide insight in the physics behind a quench. For this purpose the analytical descriptions, described in Section 4.2, are best suited. The second goal of a model is to provide an accurate a-priori prediction of the normal zone propagation velocities and minimal quench energies, based on the material properties, critical current and environmental parameters (e.g. for the design of a quench protection system in a superconducting magnet). For this purpose, because of the absence of fitting parameters, the numerical model has proven to be more able. The relatively straightforward but adequate quasi one-dimensional numerical model used in this work is described in section 4.3.

4.1 Heat Balance Equation

Both the numerical and analytical models of normal zone behaviour are based on the heat balance equation [33][1]. The one-dimensional heat equation describes the change of temperature T at position x with respect to time t and is given by

$$C(T)\frac{\partial T}{\partial t} = \frac{\partial}{\partial x}\left[k(T)\frac{\partial T}{\partial x}\right] + P_\Omega + P_i - P_c, \tag{4.1}$$

where $C(T)$ is the temperature-dependent heat capacity in J/mK, $k(T)$ the temperature dependent thermal conductivity in Wm/K and T the temperature. The power terms P_Ω, P_i and P_c represent the Ohmic power dissipation in the tape, the initial disturbance and the cooling provided by the environment respectively, all given in W/m. These individual power terms are described in detail in Subsections 4.1.1, 4.1.2 and 4.1.3.

4.1.1 Ohmic Power Dissipation

A practical superconductor can be modelled as a normal conducting element in parallel with a superconducting element [34, 35]. The current inside the normal conducting element is called I_{nc} and the current in the superconducting element is I_{sc}. The Ohmic power P_Ω is dissipated inside the normal conducting element and can be written as

$$P_\Omega = \rho(T) I_{nc}^2, \tag{4.2}$$

where ρ is the electrical resistivity of the normal conducting materials in Ω/m. The distribution of the current over the superconducting element and the normal conducting element depends on the temperature and can be divided into three regimes (see Figure 4.1):

1. *Fully superconducting* - Below the current sharing temperature T_{cs}, the total current I_{op} is smaller than the critical current $I_c(B,T)$ so that all current flows through the superconductor and no Ohmic heating occurs.
2. *Current Sharing* - T_{cs} is defined as the (magnetic field- and current-dependent) temperature where $I_c(B,T)$ falls below I_{op}. Between T_{cs} and the critical temperature T_c, a transition takes place, where an increasing amount of current runs through the normal conducting element.
3. *Fully normal* - Above T_c superconductivity is lost and all current runs through the normal conducting element.

Because the Ohmic power dissipation term results in a highly non-linear differential equation, for analytic solutions often the current sharing region is approximated using a step function, with a discontinuous transition between the fully superconducting to the fully normal regime at a certain transition temperature T_t. Classically, there are three choices available for the transition temperature [24]:

1. Cherry: $T_t = T_{cs}$

[1] Because all models in this chapter are one-dimensional, for convenience also one dimensional units are used. Throughout this chapter if the units of a certain variable are uncommon they are stated explicitly. For reference also see the nomenclature on Page 1.

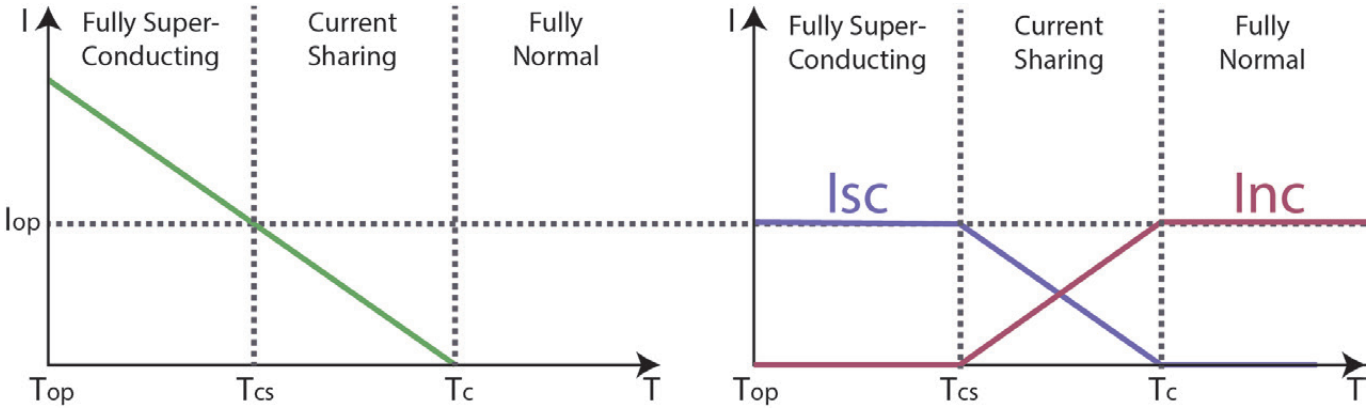

Figure 4.1: Schematic representation of current sharing in a practical superconductor (adapted from Bellis [35]).

2. Keilin: $T_t = T_c$
3. Dresner: $T_t = (T_{cs} + T_c)/2$

In addition to these standard choices some authors choose to use the transition temperature as a free fitting parameter in which it is allowed to vary between T_{cs} and T_c. In this work the option that was proposed by Dresner is chosen. This option is based on a piece-wise solution of the heat equation that takes the full current sharing regime as given in Figure 4.1 into account [34]. Such solution of Equation 4.1 can be constructed for the three regimes ($T < T_{cs}$, $T_{cs} < T < T_c$ and $T_c < T$) separately, but then the boundaries of these solutions describing various parts of the normal zone need to be matched by demanding that both temperature and temperature gradient remain continuous. This last step leads to implicit equations, which prevents the full solution to be written in a closed analytical form. For this reason Dresner showed that this full solution could be best approximated using the more simple step function model (which leads to analytical expressions), that has a transition temperature precisely at the average between the current sharing temperature T_{cs} and the critical temperature T_c.

4.1.2 Initial Power Dissipation

The initial disturbance power P_i is the power dissipated inside the conductor that triggers the development of a propagating normal zone. For an ideal quench heater the initialisation power can be described as a sharp square pulse that acts on an infinitesimal part of the conductor[2]. The power term for such a pulse can be written as

$$P_i = \delta(x) rect(t), \tag{4.3}$$

where δ is the Kronecker-delta function and $rect$ is a rectangular function defined as

$$\begin{aligned} rect(t) &= E_{pulse}/t_{pulse} && (0 \leq t \leq t_{pulse}) \\ rect(t) &= 0 && (t > t_{pulse}) \end{aligned} \tag{4.4}$$

where E_{pulse} is the energy contained in the heat pulse and t_{pulse} is the pulse duration.

4.1.3 Cooling Power

The cooling term represents both the heat flux P_{cond} through thermal conduction to the environment and the radiative heat flux P_{rad} between the tape and its environment, both in W/m. The equation to describe this cooling term is given as

$$P_c = P_{cond} + P_{rad} = h(T - T_{env}) + p\epsilon\sigma_{boltz}\left(T_{env}^4 - T^4\right), \tag{4.5}$$

where h is the heat transfer coefficient to the environment in W/mK, σ_{boltz} is the Boltzmann constant (given as $5.67037321 \times 10^{-8}$), ϵ is the thermal emissivity of the conductor surface, p is the periphery of the conductor and T_{env} is the temperature of the environment.

To estimate the influence of both these terms near the superconducting-to-normal transition, the heat flux is calculated at 93 K (the critical temperature of YBCO). The estimated emissivity for the copper is taken to be 0.7 and the periphery of the conductor 2×4.04 mm. The radiative power to the vacuum can at 4.2 K is

$$P_{rad} = 2 \cdot 4.04 \times 10^{-3} 0.7\sigma(93^4 - 4.2^4) = 0.0238\ W/m. \tag{4.6}$$

[2]It can be argued that the quench energy is lower when the heat is divided initially over the exact length of the minimal propagation zone. However this would add an additional complexity to the models since the length of the minimal propagation zone is not known (it can be estimated roughly as is described in Section 4.2.2). Because of this uncertainty it is decided to use a localized heat pulse.

For the thermal conductivity, the heat flux through the nylon (polyamide) ridge pattern at the surface of the embedded heater is considered. Since the embedded heater is heated from the inside the temperature of the heater is higher than the bath temperature and chosen to be 35 K. The thermal conductivity of nylon at 35 K is estimated to be 0.2 W/mK [36]. The thermal contact between the tape and the nylon ridges is estimated to be only 5 % of the surface area of the tape. The thickness of the ridges is estimated at 0.5 mm. The conductive heat flux from the tape to the embedded heater through thermal conduction is then calculated as

$$P_{cond} = 0.05 \cdot 0.2 \cdot \frac{4.04 \times 10^{-3}\,[93 - 35]}{0.5 \times 10^{-3}} = 4.68\ W/m, \tag{4.7}$$

which is roughly two decades larger than the radiative heat flux. This means that for the thermal behaviour near the superconducting to normal transition, even for HTS materials, the radiative term can be neglected.

4.2 Analytic Description

In this Section analytic predictions of both the normal zone velocity and the minimum quench energy are presented. The main steps of their derivation is sketched. Readers interested in a more detailed discussion are referred to Iwasa and Wilson [37, 38].

4.2.1 Normal Zone Propagation Velocity

An analytical expression for the normal zone propagation velocity can be derived directly from the heat balance equation (Equation 4.1). Since V_{nzp} describes the steady-state behaviour of a propagating normal zone, the initial disturbance term P_i is put to zero. We work out V_{nzp} in the adiabatic limit, so that also P_c is assumed to be zero (corrections to this adiabatic assumption are discussed later in this chapter. The conditions under which it is valid are estimated in Appendix B). The heat balance equation then becomes

$$C(T)\frac{\partial T}{\partial t} = \frac{\partial}{\partial x}\left[k(T)\frac{\partial T}{\partial x}\right] + \rho I_{nc}^2. \tag{4.8}$$

By substituting $z = x - V_{nzp}t$, where V_{nzp} is defined as the normal zone velocity, a coördinate transformation can be performed. The derivative of the temperature is then expressed as

$$\frac{\partial T}{\partial t} = \frac{\partial T}{\partial z}\frac{\partial z}{\partial t} = -V_{nzp}\frac{dT}{dz}. \tag{4.9}$$

To model a quench, the system is split into a normal conducting region at $z < 0$ at which the temperature is defined as $T_n(z)$ and a superconducting region at $z > 0$ at which the temperature is defined as $T_s(z)$. In the normal normal conducting region $I_{nc} = I_{op}$ and in the superconducting region $I_{nc} = 0$ (This corresponds to the simplified representation of the current sharing regime by a step function, as described in Section 4.1.1 above). The differential equations for the two domains then become

$$-V_{nzp}C(T_n)\frac{dT_n}{dz} = \frac{d}{dz}\left[k(T_n)\frac{dT_n}{dz}\right] + \rho(T_n)I_{op}^2, \qquad (z < 0) \tag{4.10}$$

$$-V_{nzp}C(T_s)\frac{dT_s}{dz} = \frac{d}{dz}\left[k(T_s)\frac{dT_s}{dz}\right]. \qquad (z > 0) \tag{4.11}$$

It is furthermore assumed that the material properties are constant with respect to the temperature. Subscripts s and n annotate whether the property is defined at the super- or the normal-conducting region respectively. Also is assumed that at the normal side $d^2T/dz^2 = 0$. The equations then become

$$C_n V_{nzp}\frac{\partial T_n}{\partial z} + \rho_n I_{op}^2 = 0, \qquad (z < 0) \tag{4.12}$$

$$k_s\frac{d^2T_s}{dz^2} + C_s V_{nzp}\frac{dT_s}{dz} = 0. \qquad (z > 0) \tag{4.13}$$

The solution for the normal side is given by a straight line $T_n(z)$. By imposing the boundary condition $T_n(0) = T_t$, where T_t is the transition temperature, the solution becomes

$$T_n = -\frac{\rho_n I_{op}^2}{C_n V_{nzp}}z + T_t. \tag{4.14}$$

For the superconducting region the solution is an exponential equation. By imposing the boundary conditions $T_s(\infty) = T_0$, where T_{op} is the operating temperature, and $T_s(0) = T_t$, the solution at the superconducting region becomes

$$T_s = (T_t - T_{op})\exp\left[-\frac{C_s V_{nzp}}{k_s}z\right] + T_{op}. \tag{4.15}$$

Because no sudden jumps may occur in the heat flux, the temperature gradient must be a continuous function at the border between the two regions. This imposes the following boundary condition

$$\left.\frac{dT_n}{dz}\right|_{z=0} = \left.\frac{dT_s}{dz}\right|_{z=0}. \tag{4.16}$$

By substituting equations 4.14 and 4.15 the equation becomes

$$\frac{k_n \rho_n I_{op}^2}{C_n V_{nzp}} = -C_s V_{nzp}(T_t - T_{op}), \tag{4.17}$$

which, when solved for the velocity becomes

$$V_{nzp} = \frac{I_{op}}{C_0}\sqrt{\frac{\rho_n k_n}{(T_t - T_{op})}}. \tag{4.18}$$

C_0 is the geometric average thermal capacity calculated as $\sqrt{C_n C_s}$. The material properties ρ, k and C are best calculated at $\tilde{T} = (T_t + T_{op})/2$ [37]. The equation then becomes

$$V_{nzp} = \frac{I_{op}}{C(\tilde{T})}\sqrt{\frac{\rho(\tilde{T})k(\tilde{T})}{(T_t - T_{op})}}. \tag{4.19}$$

The analytical expression acquired can now be compared to the measured data. The material properties are calculated using the fitting relations provided in Appendix G and the thickness of the layers from Table 2.2. They are shown in Figure 4.3. The critical current is interpolated from the measured data see Figure 3.2. The critical temperatures are determined through extrapolation and are found to be around 83 K for all values of magnetic field. The analytic expression evaluated for 50 and 90 $\%Ic$ as function of the operation temperature at a magnetic field of 14 T, is compared to the measured data in Figure 4.2. It can be seen that the analytical prediction (Equation 4.19) approximates the data well at lower temperatures, but starts to deviate at lower currents. The maximum deviation from the data at these lower currents is more than a factor two. It should also be noted that the power 1.5 as introduced in Section 3.5 is not present in the analytically calculated data.

The likely cause of the differences between the measured data and the analytic expression in Equation 4.19 is the fact that the experiment is only 'quasi-adiabatic' (as discussed further in Appendix B). The cooling term can be implemented in the analytic expression in the form of a minimum propagation current [17]. Equation 4.19 then becomes

$$V_{nzp} = \frac{I_{op} - I_m}{C(\tilde{T})}\sqrt{\frac{\rho(\tilde{T})k(\tilde{T})}{(T_t - T_{op})}}, \tag{4.20}$$

where I_m is the minimum propagation current, which can be calculated using [34, 24]

$$I_m = \frac{\sqrt{1+8\alpha}-1}{2\alpha} I_c, \tag{4.21}$$

where α is the Stekly parameter given as

$$\alpha = \frac{\rho I_c^2}{h(T_c - T_{op})}. \tag{4.22}$$

To avoid division by zero in the Stekly parameter, I_m is simply set to zero when h is zero. Now Equation 4.20 is compared to the measured data (see Figure 4.4). It can be seen that when the cooling term h increases the normal zone velocity starts to decrease, especially at the higher temperatures. This is because I_m takes up a larger percentage of the lower currents in this temperature domain. If the cooling term h becomes higher, at a certain point the minimal propagation current exceeds the sample current and no normal zone propagation is possible. Based on Figure 4.4 the cooling is estimated to be around $h \approx 0.1\ W/mK$. Using this value for h, the analytic expression approximates the data within a maximum deviation of 25 %. With the same setting similar deviations are found for the V_{nzp} data recorded at 6 and 10 T (25 % and 22 % respectively).

4.2.2 Minimum Quench Energy

The minimum quench energy can be estimated by introducing the concept of a minimum propagation zone ℓ_{mpz}. The amount of Ohmic heat generated in a normal zone is proportional to its length, while heat loss towards the colder sample parts at either length is not. Therefore, when the initial disturbance creates a normal zone that is shorter than the critical length ℓ_{mpz}, cooling exceeds heating so that the normal zone shrinks and eventually disappears. This length can thus be

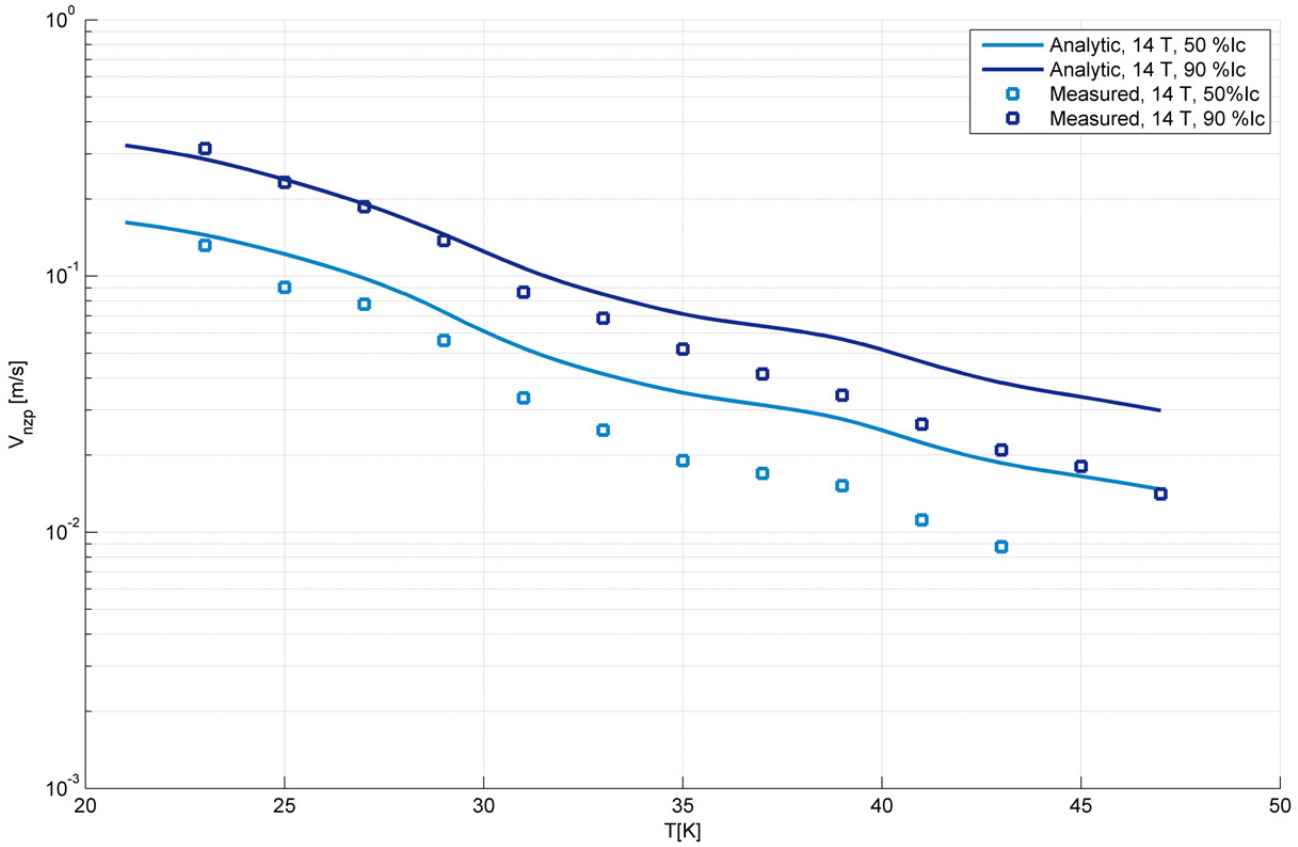

Figure 4.2: Comparison between measured data and the analytic model for the normal zone propagation velocity at 14 T for values of 50 and 90 $\%Ic$.

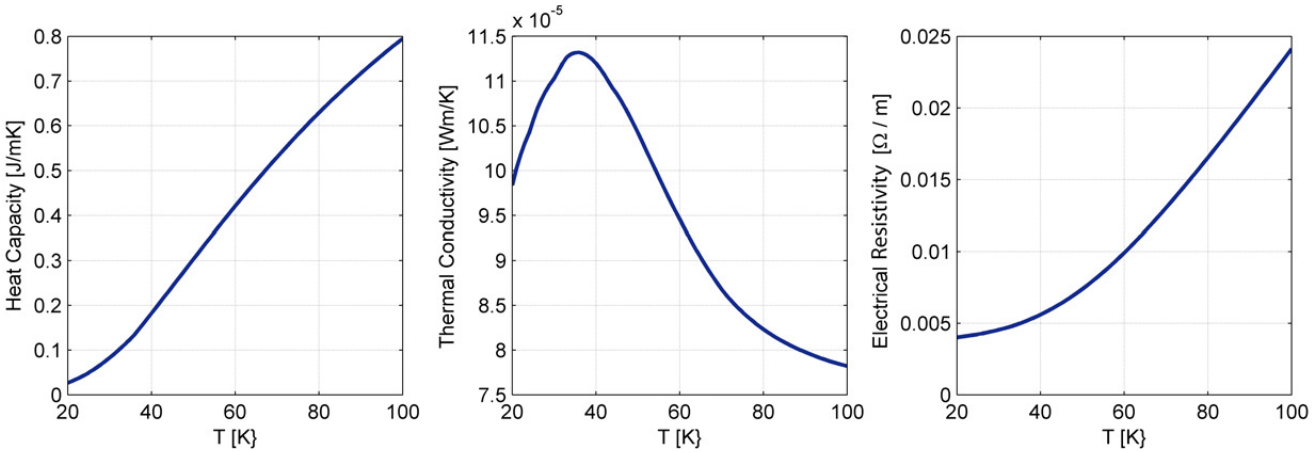

Figure 4.3: Calculated material properties C, k and ρ for SuperPower tape SCS4050 (see Appendix G for the scaling relations used in the calculation of these properties).

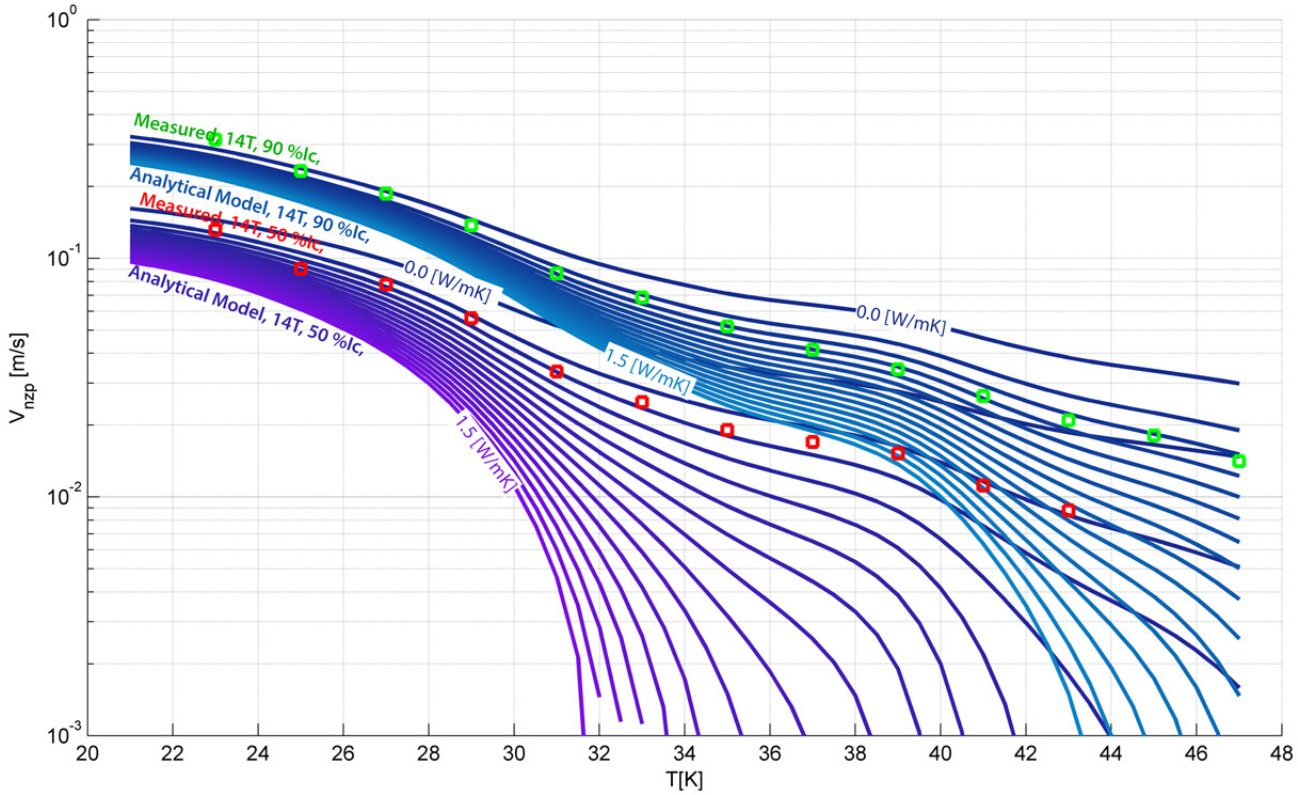

Figure 4.4: Comparison between measured data and the analytic model for the normal zone propagation velocity at 14 T for values of 50 and 90 $\%Ic$. The model is evaluated for values of the cooling term h ranging between 0.0 and 1.5 W/mK with increments of 0.1 W/mK.

calculated using the balance between the Ohmic heating inside the zone and the cooling at its boundaries. This balance can be written as

$$\ell_{mpz}\rho I^2 = \frac{2k(T_t - T_{op})}{\ell_{mpz}}, \tag{4.23}$$

where ρ is the resistivity and k the thermal conductivity of the non superconducting materials. The temperatures T_t and T_{op} are the transition temperature and the operation temperature of the conductor. The minimal propagation zone then becomes

$$\ell_{mpz} = \left[\frac{2k(T_t - T_{op})}{I^2\rho}\right]^{1/2}. \tag{4.24}$$

The minimal quench energy is now the amount of energy that the initial disturbance needs to deliver in order to raise the temperature of the conductor above T_t over a length equal to the minimal propagation zone. This can be calculated as

$$MQE = \ell_{mpz}\int_{T_0}^{T_t} C(T)dT, \tag{4.25}$$

where $C(T)$ is the temperature dependent heat capacity of the conductor. Again the results are compared with the measured data in Figure 4.5. It can be seen that the general behaviour looks similar, MQE increases with temperature and decreases with current. At higher temperatures the data matches the analytic equation within 35 %. However, at lower temperatures large deviations between the measured data and the prediction (Equation 4.24 and 4.25) are found (the predicted MQE is about a factor 3 too low). The reason for this relatively large deviation is because the data is compensated for an heater efficiency using a constant factor of 20 % calculated for a sample at zero current as described in Appendix F. The quench heater model also allows for calculation with a sample current, but this would inherently replicate the results from the numerical models described further down in this Chapter.

4.2.3 Conclusion

From the analytical models the following conclusions are drawn:

1. The experiment is quasi-adiabatic. The cooling factor h required to achieve an optimal correspondence between the V_{nzp} data and the analytical model is found to be approximately 0.1 W/mK.

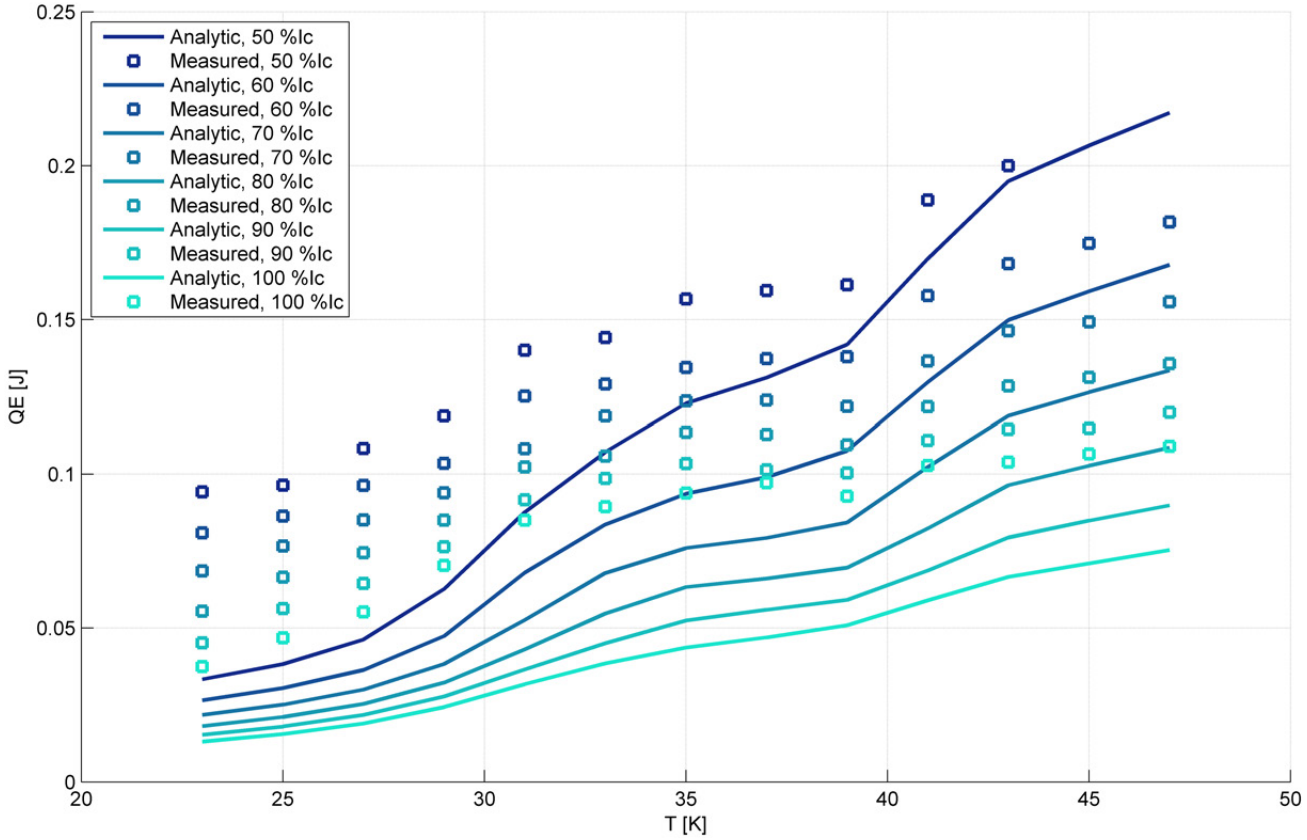

Figure 4.5: Comparison analytic expression for MQE and the measured quench energies, at 14 T.

2. After the cooling has been accounted for in the analytic equations, a reasonable fit can be found for the normal zone velocities (within 25 % of the measured data).

3. The measured minimum quench energy does not compare well to the analytical model. This is likely caused by the (a-priori unknown) variation in heater efficiencies over the measured current range.

4. The analytic models require a choice for the transition temperature T_t. Because this parameter depends on the material properties of the conductor, it is hard to use these analytical expressions for an a-priori prediction.

4.3 Numerical Description

The analytical expressions provide good insight in the thermal behaviour of a practical superconductor. However, they require the choice of a transition temperature T_t and another temperature at which the material properties are calculated $\tilde{T}$. Because these choices themselves depend on the material properties of the conductor, the predictive capability of these models is only minor. Implementing parallel path current sharing within a numerical model makes it possible to predict the normal zone velocities and the minimal quench energies without such choices. The only variable that remains to be fitted in this numerical model is the cooling term h. For future experiments, even this may also avoided by measuring the minimal propagation current I_m directly. In addition to their better predictive capability, the numerical models also provide more detailed insight in the development of the normal zone, since they are able to produce the temperature profiles as function time.

4.3.1 Parallel Path Model

The parallel path model is a more complete current sharing model. As discussed before, a practical superconductor can be seen as a superconducting element, with current I_{sc}, running in parallel with a normal conducting element, with current I_{nc} (see Figure 4.6). The total current in the conductor is then given as

$$I_{op} = I_{sc} + I_{nc}. \tag{4.26}$$

In the analytic description it is assumed that as soon as the temperature exceeds the transition temperature, all current runs through the normal conducting element. In reality however, the current in the superconducting element saturates, forcing the excess current to flow through the normal conducting element. Unfortunately it is impossible to formulate

a direct equation to calculate the current in either elements. The current in the superconducting element can however readily be approximated numerically using the implicit expression

$$I_{op} - \frac{E_0}{\rho_n}\left[\frac{I_{sc}}{I_c}\right]^N - I_{sc} = 0, \tag{4.27}$$

where E_0 is the criterion used to determine the critical current (in this work 10 μV), I_c the critical current and N the N-value of the conductor. I_{sc} needs to be determined such that the equation is valid. This can be achieved relatively easily, using a numerical search algorithm such as the Newton-Raphson method. For the upper and lower bounds I_0 and 0 A are used, respectively. After I_{sc} is determined, I_{nc} can be calculated using Equation 4.26. As an example, in Figure 4.7 I_{sc} and I_{nc} are plotted against I_{op} at a fixed T and against T at fixed I_{op}. The electrical resistivity used to create this plot is taken from Figure 4.3. Comparison with the schematic current sharing model in Figure 4.1 shows that a smoother transition takes place at T_{cs} and T_c. This smearing out of the current sharing regime is caused by the finite N-value of the conductor, which gives the voltage transition at the current sharing temperature a power law character. However the most important remark is that here, in contrast to the analytical normal zone propagation models, no choice for the transition temperature is required.

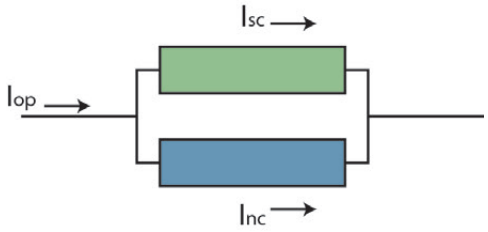

Figure 4.6: Schematic representation of a superconductor with a normal conducting element in parallel with a superconducting element.

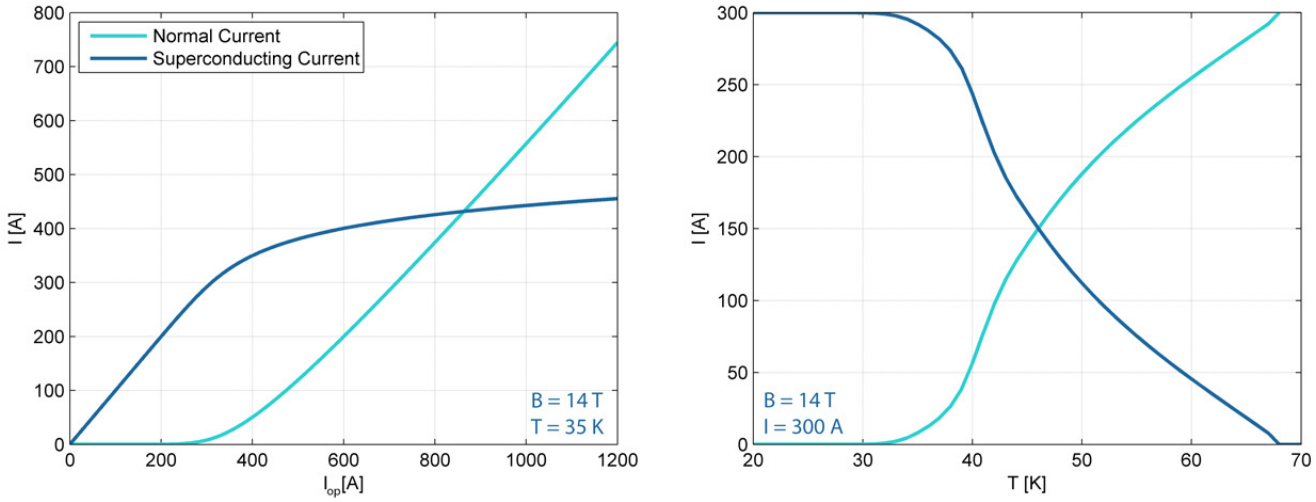

Figure 4.7: Plot demonstrating current sharing between a superconducting and a normal conducting element connected in parallel in a magnetic field of 14 T. On the left I_{sc} and I_{nc} are plotted against the overall sample current, at a fixed temperature of 35 K, and on the right, against the temperature, at a fixed current of 300 A (electrical conductivity of the non-superconducting materials is based on the material composition of SCS4050).

4.3.2 Finite Difference Method

In order to find a numerical solution to the heat Equation (Equation 4.1), it can be rewritten for discrete elements called nodes. This method is often referred to as the finite difference method. For a one-dimensional problem these nodes lie in a chain and are connected through thermal resistors. Furthermore to each node is attributed a thermal capacity (See Figure 4.8). The nodes are indexed in an ascending order using the index i. Transverse heat transfer to the environment can be added using a cooling term, making the model quasi one-dimensional. The heat equation for each node in this system becomes

$$C(T_i)\frac{dT_i}{dt} = \frac{k(T_i)(2T_i - T_{i-1} - T_{i+1})}{dx_i} + I_{nc}^2\rho(T_i)dx_i + P_i(x_i, t) - h(T_i - T_{op})dx_i, \tag{4.28}$$

where $C(T)$ is the temperature-dependent heat capacity in J/mK, $k(T)$ the temperature-dependent thermal conductivity Wm/K, $\rho(T)$ the temperature-dependent electrical resistivity in Ω/m and dx_i the length of the node with index i. If the start temperatures are known the system of equations can be solved for each time step through numerical integration. Such a scheme is called 'forward time, centred space' (FTCS). The temperatures of the next time step are then simply calculated with

$$T_i(t+dt) = T_i(t) + \frac{dT_i}{dt} \cdot dt, \tag{4.29}$$

where dt is the increase in time, which can be determined each time step such that dT/dt becomes smaller than a set value. However the heat equation is a 'stiff' differential equation. This means that it becomes unstable under FTCS integration, unless relatively small time steps are used, resulting in long computing times. To remedy this problem a different but more complex integration scheme can be used. One of them is 'backward time, centred space' (BTCS) which solves a set of equations to determine the temperatures of the next time step, such that it matches with the temperature profile from previous time step [39]. This technique is readily available in Matlab under the *ode15s* routine, which is specifically designed to solve time dependent systems of differential equations that have a stiff nature. Using this solver both a steady state model and a time-dependent model are created (see respectively Sections 4.3.3 and 4.3.4).

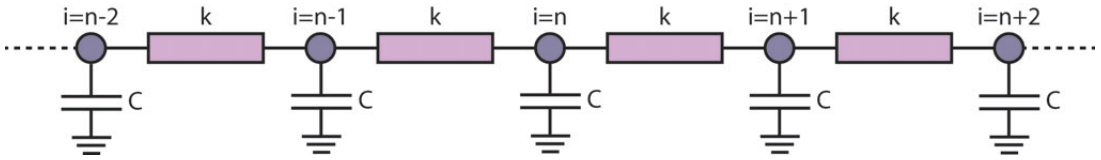

Figure 4.8: System of nodes described by the discrete heat equation.

4.3.3 Steady State

To provide more insight in the temperature profile of the normal zone front, it is first attempted to find a numerical solution to the heat equation similar to the analytical model (Equation 4.11). This is done using a boundary value problem solver (Matlab *BVP*). However the solution becomes only stable if the normal zone velocity is known beforehand. Because this is unpractical, it is decided to try a different approach where an additional velocity term is added to the discrete heat equation (Equation 4.28), to simulate the velocity of the medium (a 'trick' often used in fluid mechanics). In essence, this method is the same as the use of the 'moving' coordinate leading to equations 4.10 and 4.11. In order to maintain context with these transformed analytical equations it is decided to name the transformed coordinate also here z. The discrete heat equation with this additional velocity term is then given as

$$C(T_i)\frac{dT_i}{dt} = k(T_i)\frac{2T_i - T_{i-1} - T_{i+1}}{dz_i} + V_{nzp}C(T_i)\frac{T_{i+1} - T_{i-1}}{2} + I_{nc}^2\rho(T_i)dz_i - h(T_i - T_{op})dz_i, \tag{4.30}$$

where the normal current can be determined using Equation 4.27 with the Newton-Raphson method. For a steady state solution the left term of the equality is zero. In this case the equation becomes very similar to its analytical counterpart (Equation 4.11). This solution can be found by using a using a time dependent solver (Matlab *ode15s*), in which velocity of the system is changed each time step using the average temperature change of all nodes, given as

$$\frac{dV_{nzp}}{dt} = \frac{\gamma}{n_{nodes}} \sum_{i=0}^{n_{nodes}} \frac{dT_i}{dt} dx_i, \tag{4.31}$$

where n_{nodes} is the total number of nodes and γ is a damping factor. If the average temperature change is positive the velocity is too low and is therefore increased and vice versa. After some time the system converges to a solution. As an example, it is chosen to use 160 nodes divided linearly in the interval of $[-0.05, 0.05]$ m. The start temperature at $x = -0.05$ m is $T_{op} + 50$ and at $x = 0.05$ m the start temperature is T_{op}, where T_{op} is set to 35 K. The start temperatures of the other nodes are interpolated linearly. The start velocity is chosen to be 0.01 m/s. The current in the sample is set to 90 $\%Ic$ which corresponds to a current of 115 A. The values for the critical current, I_c and N are interpolated through smoothing splines using the data from the measurements (see also Figure 3.2). The material properties are the same as presented in Figure 4.3 and thus Appendix G. The layer thickness of the individual materials is taken from Table 2.2. Through trial and error a reasonable value for the damping factor is found at $\gamma = 15$ m/s^2K. The resulting temperature profile and velocity as function of time are presented in Figure 4.9. It can be seen that the normal zone velocity becomes stable after one second and the temperature profile converges to a single line. These velocity and temperature profiles is the steady state solution to Equation 4.30.

Now the results from the measurements are compared to the model. Without cooling the normal zone velocities at the lower currents are a factor two too high. In Figures 4.10-4.12 the calculated normal zone velocities from the steady

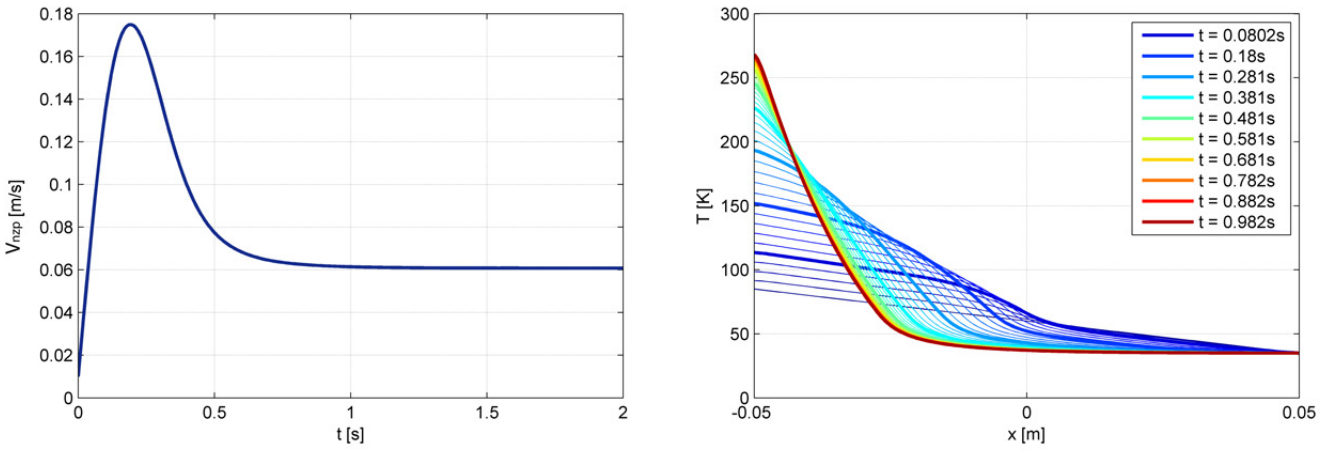

Figure 4.9: Demonstration of the steady state solution for a quench inside a YBCO coated conductor. On the left the stabilization of the velocity and on the right the temperature profiles as function of time. Calculation is performed at $Top = 35\ K$ and $I_{op} = 115\ A$ which corresponds to 90 $\%Ic$.

state model, with values for h ranging between 0 and 1.5 W/mK, are compared to the measured datasets for 50 and 90 $\%Ic$ at the respective magnetic fields fields of 6, 10 and 14 T. It can be seen that the result is very similar to that of the analytical expression in Figure 4.4. For a good fit the value of h lies around 0.3 W/mK. With this cooling factor, the deviation with the measured data is 30 %, 25 % and 16 % respectively. These deviations may be explained by the fact that the material properties of the tape were taken from literature data and are therefore not necessarily in good agreement with the materials used inside the YBCO tape that is measured. Therefore a deviation of 30 % is deemed acceptable.

4.3.4 Time Dependent

Because the steady-state model does not include the initiation of the quench, it is unable to calculate the minimum quench energies. Therefore also a time-dependent model is created. The time-dependent model is also based on the discrete heat equation (Equation 4.28), in which the normal current I_{nc} is again determined using Equation 4.27 and the Newton-Raphson method. The quench originates from the center node using a discrete form of the initial disturbance term (see Section 4.1.2). The differential equation is solved using Matlab *ode15s*. To compare the model to the measured data 400 nodes are divided over an interval of $[-0.1, 0.1]$ m. All nodes start at the same temperature T_{op}. An example of the resulting temperature profiles is presented in Figure 4.13, both for the situation where $E_{pulse} < MQE$ and for $E_{pulse} > MQE$. In the first case the normal zone clearly collapses, while in the second case a propagating normal zone develops.

To find the MQE, a search algorithm can be used that runs the model multiple times. It requires an upper estimate and a lower estimate for the quench energy. First the upper and lower estimates are tested to ensure that a quench occurs in the upper estimate and doesn't occur for the lower estimate. If the estimation proves to be incorrect the upper and lower boundary are adjusted automatically. After the upper and lower estimates have been confirmed, the energy exactly in between the upper and lower estimate is tried. If a quench occurs the upper estimate is shifted towards the tested energy. If no quench occurs the lower estimate is shifted. This process is repeated until the difference between the upper and lower estimate is less than a pre-set tolerance (for the calculations in this report a tolerance of 0.1 % is used). The minimal quench energy is then equal to the upper estimate.

In addition to the minimum quench energy the normal zone propagation velocity can also be derived from this model. A zone is defined to be normal when the electric field exceeds 100 $\mu V/m$. The length of the normal zone ℓ_{nz} is then calculated at each time step using the two intersections between a horizontal line at 100 $\mu V/m$ and the calculated electric field. The normal zone velocity then becomes

$$V_{nzp} = \frac{1}{2}\frac{d\ell}{dt}. \tag{4.32}$$

The factor 1/2 compensates for the fact that the normal zone travels in two directions. The model is compared to the measured data. The best agreement is found at a cooling term of 0.4 W/mK, where the maximum deviation from the data is found, 20 % at 14 T, 8 % at 10 T and 15 % at 6 T. For all magnetic fields the deviation is once more highest at the lower current. Similar to the steady-state model, these deviations are within an acceptable level because of the uncertainty on the material properties used in the model.

Using the time-dependent model it is possible to calculate quench propagation in a fully adiabatic environment. The

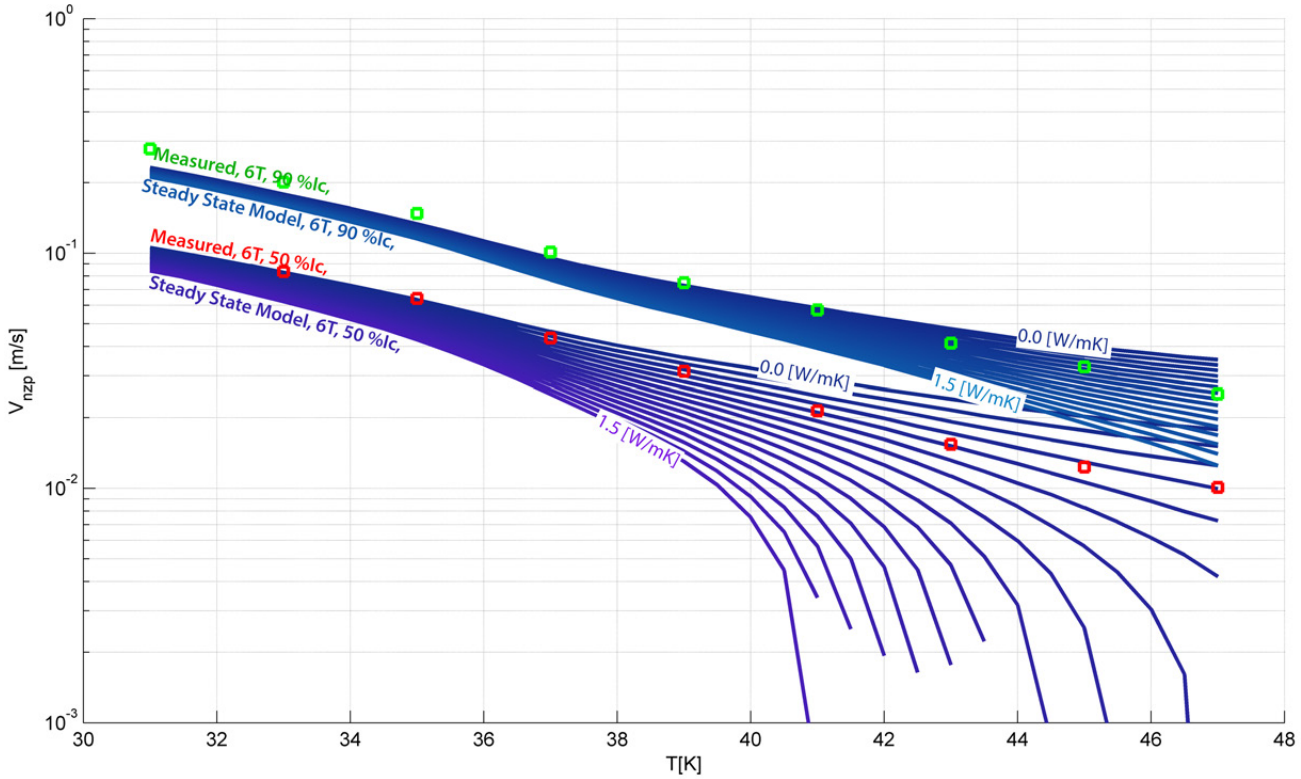

Figure 4.10: Comparison between measured data and steady state model for the normal zone propagation velocity at 6 T for values of 50 and 90 $\%Ic$. The model is evaluated for values of the cooling term h ranging between 0.0 and 1.5 W/mK with increments of 0.1 W/mK.

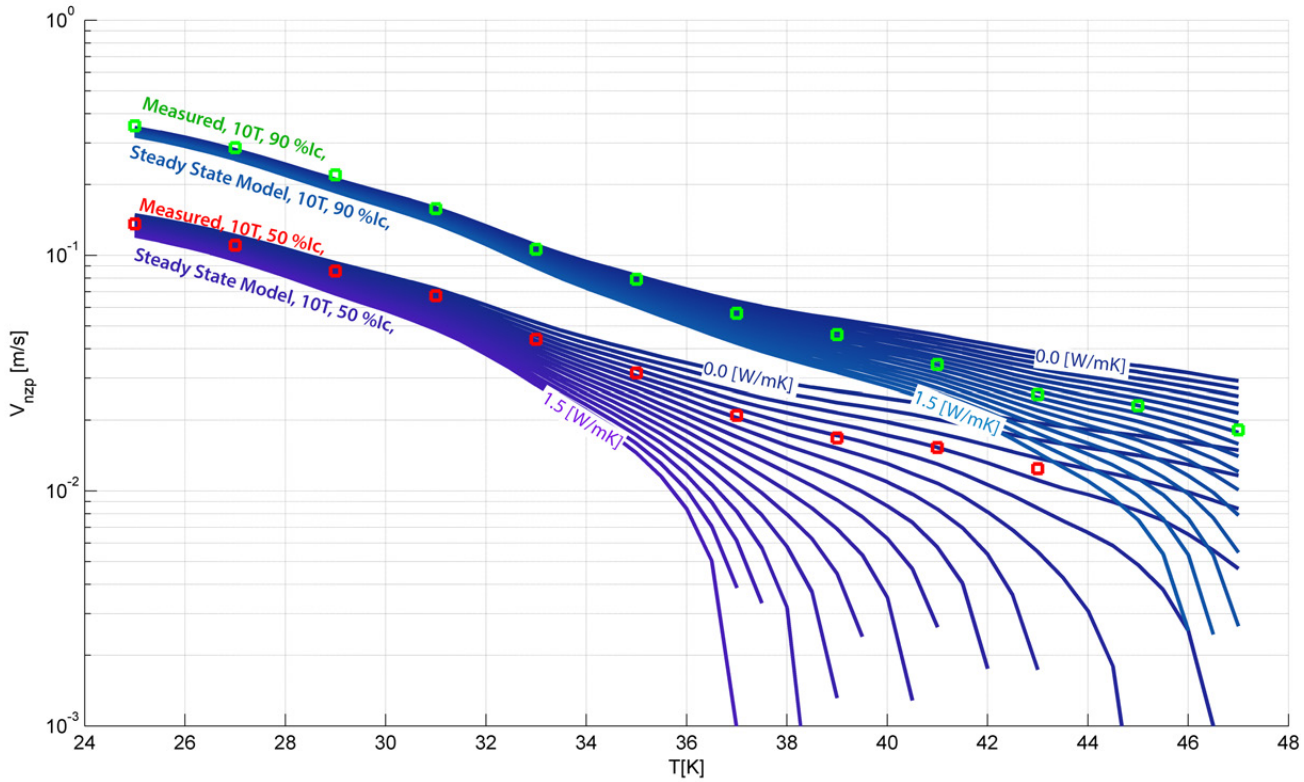

Figure 4.11: Comparison between measured data and steady state model for the normal zone propagation velocity at 10 T for values of 50 and 90 $\%Ic$. The model is evaluated for values of the cooling term h ranging between 0.0 and 1.5 W/mK with increments of 0.1 W/mK.

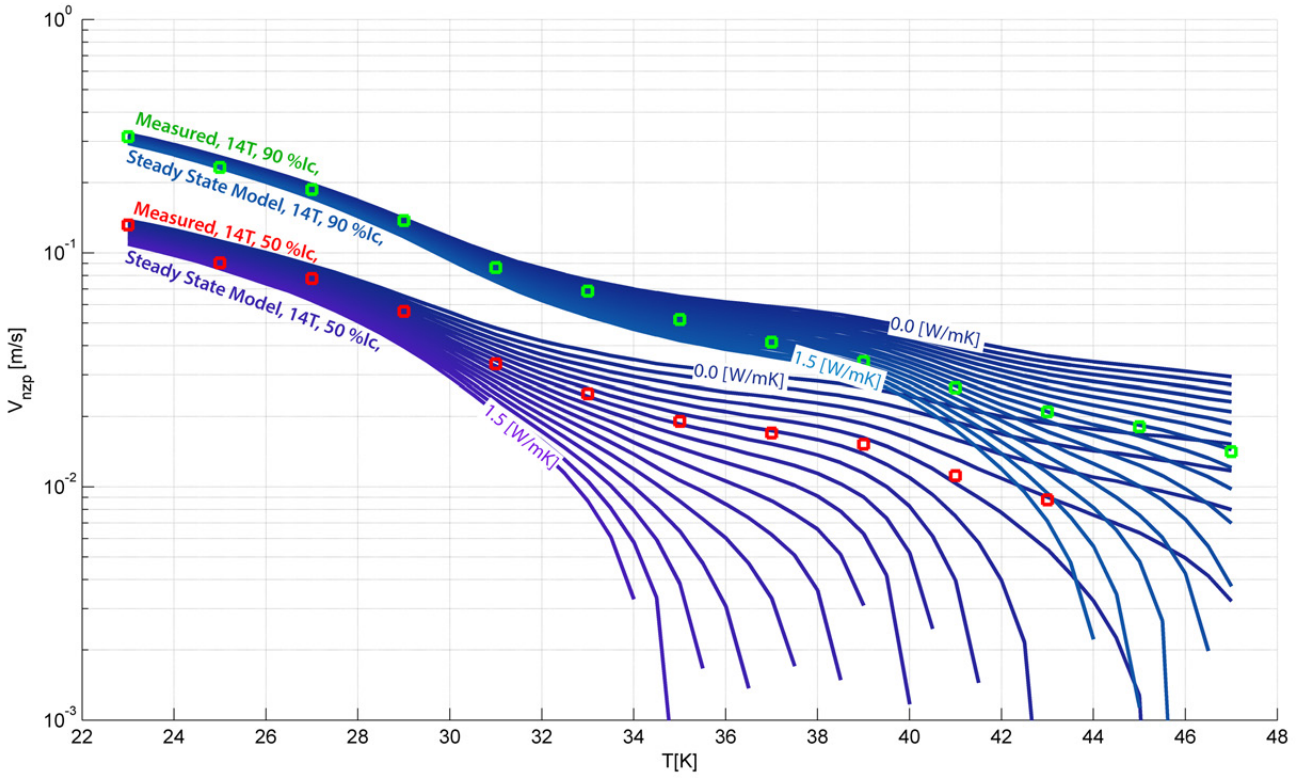

Figure 4.12: Comparison between measured data and steady state model for the normal zone propagation velocity at 14 T for values of 50 and 90 $\%Ic$. The model is evaluated for values of the cooling term h ranging between 0.0 and 1.5 W/mK with increments of 0.1 W/mK.

results from such a calculation are presented in Figure 4.14. The plots are in essence a numerical reproduction of the measurement shown in Figure 3.4 in which heat efficiencies and cooling terms are negated. As such, they validate the model from the measured data.

4.3.5 Conclusion

From the numerical models the following conclusions are drawn:

- Similar to the analytical models it is required to introduce a cooling term to approximate the measured data. This again confirms that the measurements are performed under quasi-adiabatically, as opposed to fully adiabatic conditions.
- With this cooling term the maximum difference between the model and the measured data is 30 % for the steady state model and 20 % for the time dependent model. This is within acceptable levels because of the uncertainty that comes with the choice for the material properties.
- Numerical results for fully adiabatic conditions and an ideal heater, are available in Figure 4.14.
- For the numerical models no choices for the transition temperature nor the material property temperature are required, thereby making the numerical models better for making an a-priori prediction.

4.4 Sensitivity Analysis

The computer models created allow for the study of quench propagation in YBCO coated conductors in more detail. Because a full numerical analysis of the influence of various design parameters for conductors and devices lies outside the scope of this work, only a few possibly interesting results are presented here. For interested readers, it is noted that the models are available at the EMS chair.

An interesting parameter that is hard to vary in a practical experiment is the N-value. Therefore the steady state model is used to calculate the normal zone velocities as function of the N-value. The results are presented in Figure 4.15. It can be seen that the velocity increases with the N-value and that it saturates both at the low values and at the high values. The reason it saturates at the high end is because with increasing N-value the current sharing model converges to the analytical Cherry model with $T_t = T_{cs}$, while at low N-value on the other hand it converges to the analytical Keilin model

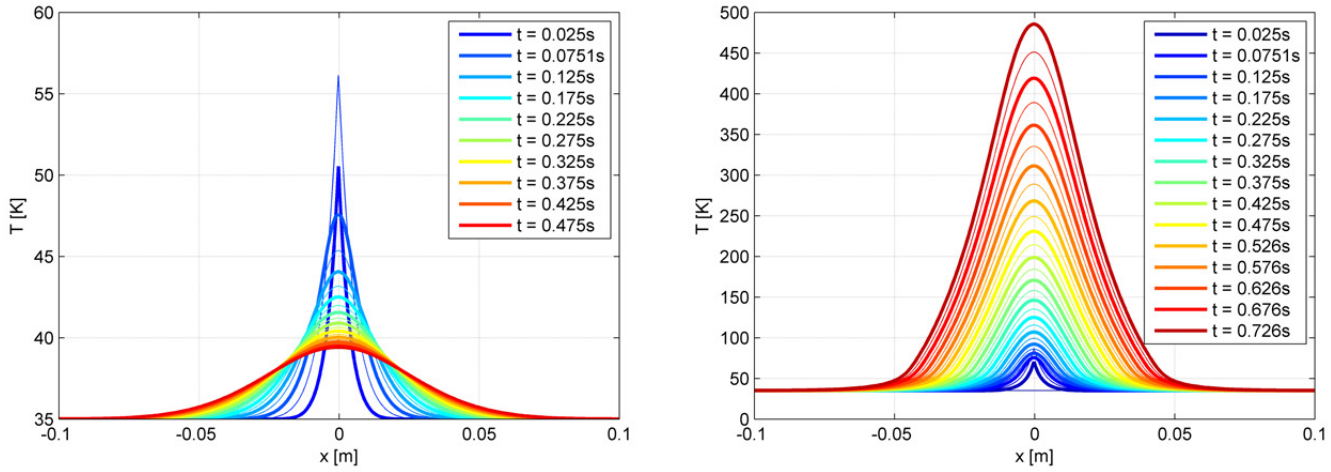

Figure 4.13: Demonstration of the transient solution of the normal zone development inside SCS4050 YBCO coated conductor. Plotted are the temperature profiles of the conductor as function of time. On the left the pulse energy is lower than the minimal quench energy and the normal zone disappears again. On the right side the pulse energy exceeds the minimum quench energy and a propagating normal zone results.

which assumes $T_t = T_c$ (see Section 4.1.1). Based on the measured data the N-value is about 10, at which the transition resembles the current sharing model in Figure 4.1 (with the difference of the more smoothed curves). As an example the calculated normal and superconducting currents are plotted for three different N-values in Figure 4.16.

Another interesting parameter is the thickness of the copper stabilizer material. The normal zone propagation velocity as function of the copper thickness is presented in Figure 4.17. The normal zone velocity is inversely related to the thickness of the copper h_{cu}. This can be straightforwardly explained by examination of Equation 4.19. Additional copper means that the one-dimensional electrical and thermal conductivity both become lower and the one-dimensional heat capacity becomes higher, all three strengthen this inverse relationship between V_{nzp} and h_{cu}.

4.5 Comparison of Data to Literature

Literature data on the normal zone behaviour in YBCO coated conductors are not abundantly available. Already briefly mentioned in Section 1.5 some studies are available. Below, all publications that were found are presented chronologically, together with a short description of the data they present. A visual overview is also presented in Figures 4.18 and 4.19, which show the literature data as an overlay on top of the $V_{vnzp}(I)$ and $QE(I)$ data from this report.

- *J. Lue et al.* (2003) [16] - In this work, the quench propagation in a 12.5 mm wide YBCO conductor is measured without applied magnetic field. The temperature is controlled using a cryocooler. The measured normal zone velocities are in the range of 1.4 to 8.3 mm/s for temperatures above 54 K.
- *R. Grabovickic et al.* (2003) [17] - In this work, a silver stabilized YBCO tape produced by the thin film group at the Oak Ridge National Laboratory (ORNL) is measured using a cryocooler. They measured at a fixed current of 30.3 A, in a temperature range of $45.8 - 76.4$ K at zero applied magnetic field. The quench propagation velocities found are in the range of $0 - 20$ mm/s.
- *X. Wang et al.* (2005) [18] - In this work, a 10 mm wide YBCO coated conductor with stabilizer from American Superconductor Corporation (AMSC) is measured. The temperatures are between 58 and 79 K and are controlled using a cryocooler. The transport current ranged between 30 and 90 $\%Ic$ and no magnetic field is applied. The minimal quench energies lie in the range of $0.3 - 3.4$ J and the normal zone velocities in the range of $2 - 27$ mm/s.
- *F. Trillaud et al.* (2005) [19] - In this work, a non-stabilized YBCO coated conductor is measured in self field at 77 K for currents at 50, 75 and 98 $\%Ic$. The minimum quench energies found are 0.335, 0.246 and 0.205 J, respectively. The normal zone propagation velocities found are 2.5, 5.0 and 5.2 mm/s respectively.
- *A. Angrisani et al.* (2008) [20] - In this work, a copper stabilized 344 YBCO tape manufactured by American Superconductor Corporation (AMSC) is measured. The temperatures in this work are 75 and 80 K and measurements are performed in the range of $50 - 100$ $\%Ic$. Interesting is that the measurements for the minimal quench energies are performed with the quench heater both on the YBCO-side and on the Hastelloy side of the tape. For the first case the QE lies in the range of $0.4 - 0.7$ J and for the latter case in the range of $0.6 - 1.6$ J. The normal zone propagation velocities are in the range of $5 - 20$ mm/s.

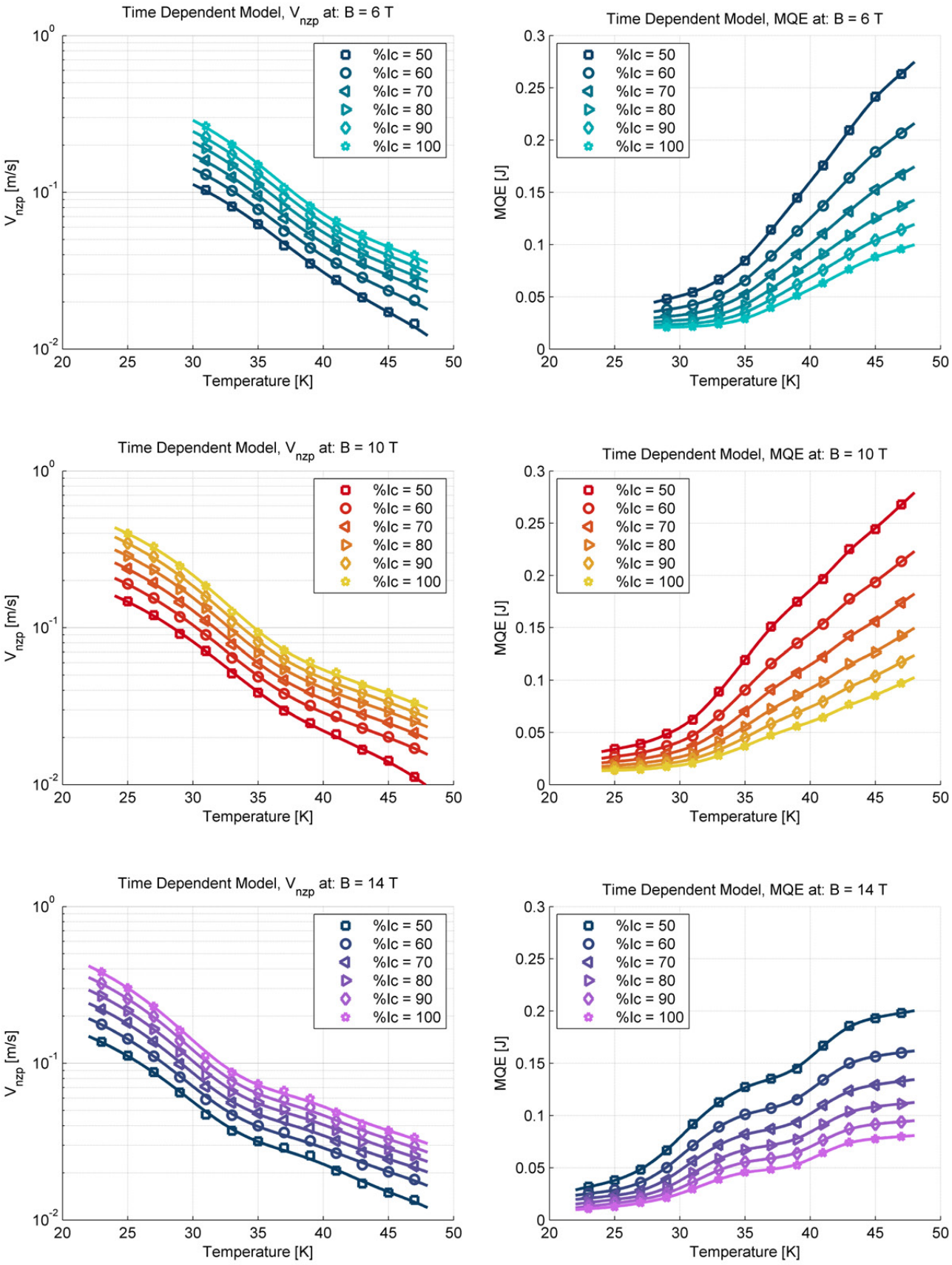

Figure 4.14: Normal zone propagation velocity and quench energy for the SCS4050 tape, calculated using the time dependent model under fully adiabatic conditions. All data points for both the propagation velocity and the minimal quench energy are interpolated using smoothing splines. This is in essence a numerically approximated idealized version of the measured data in Figure 3.4.

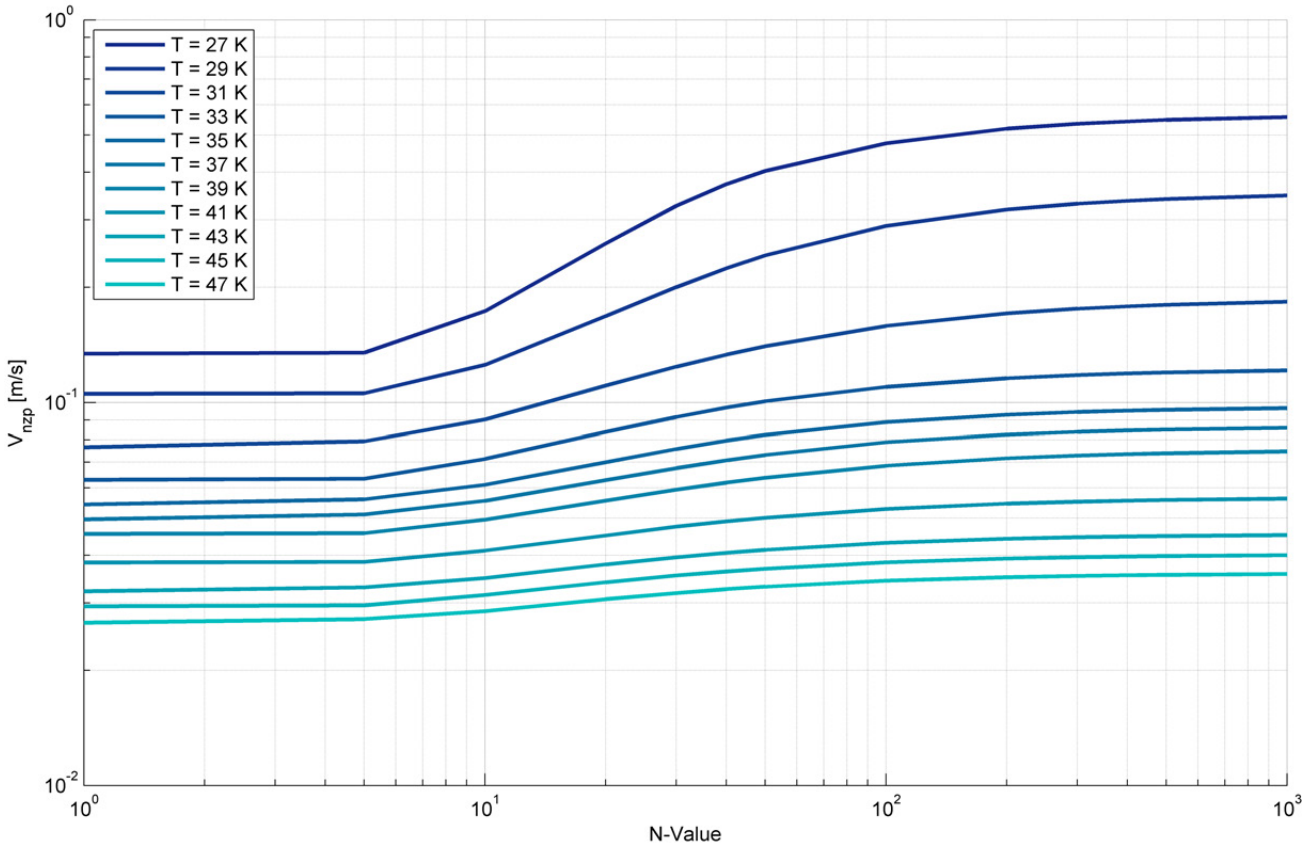

Figure 4.15: Dependence of the normal zone velocity on the N-value at various temperatures and 90 %Ic, calculated with the steady state model.

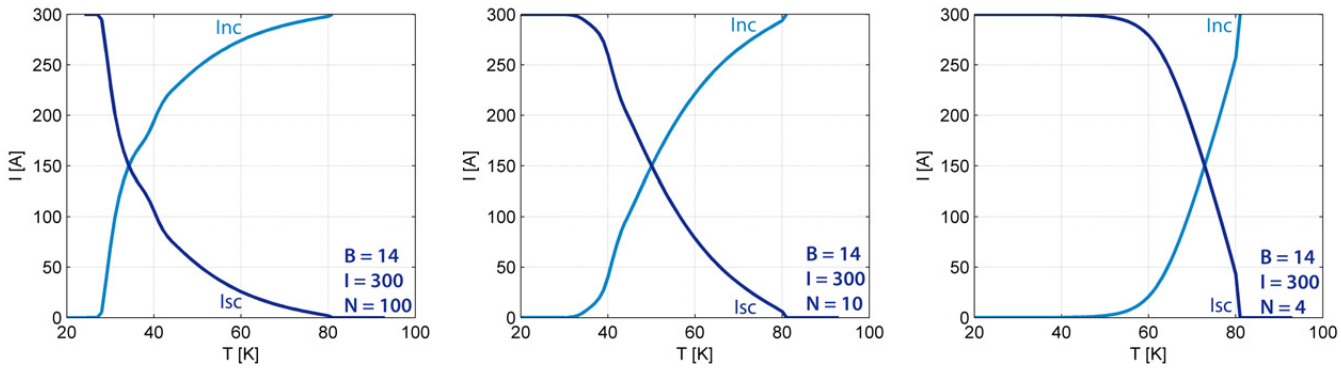

Figure 4.16: Current versus temperature demonstration of the dependence of the parallel path current sharing model (described in Section 4.3.1) on the N-value of the conductor.

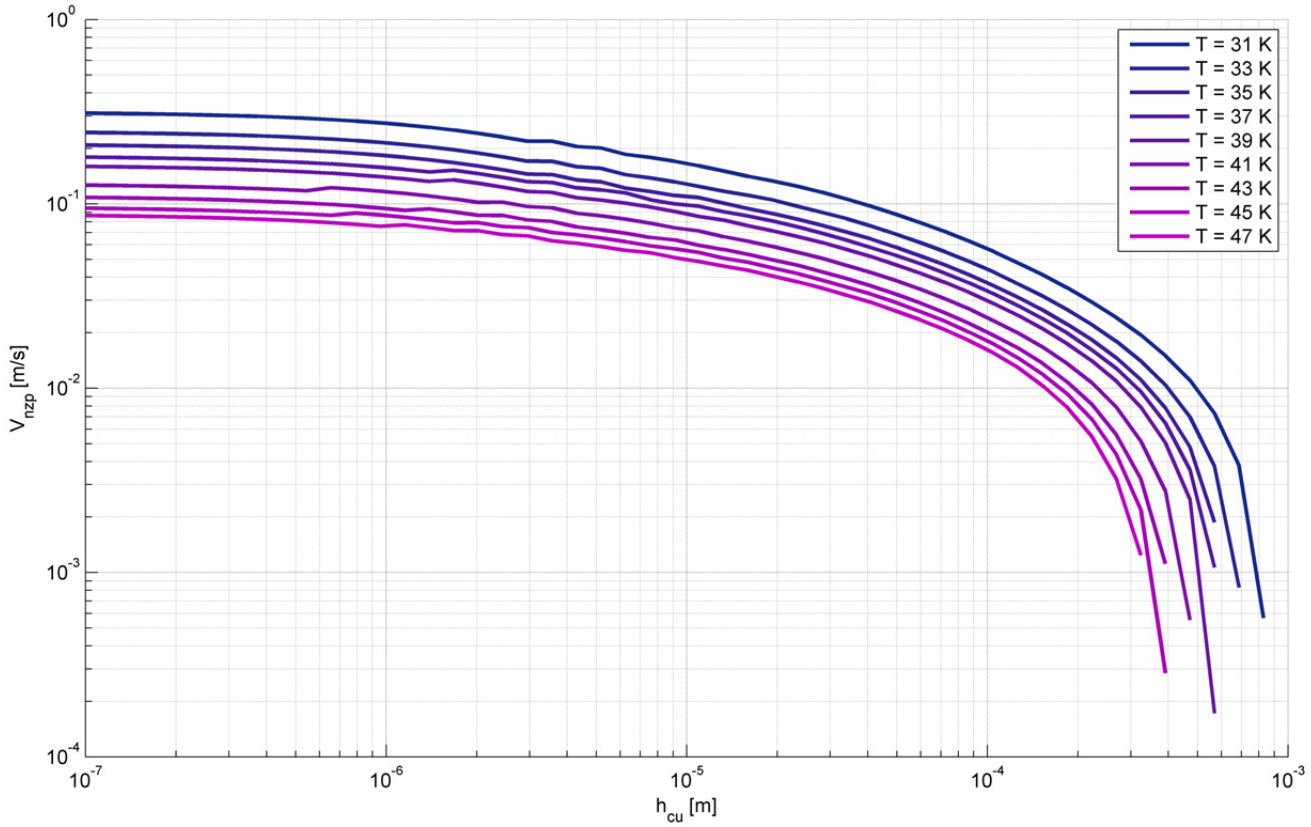

Figure 4.17: Normal zone propagation velocity as function of the thickness of the copper stabilizer layer at various temperatures and 90 $\%Ic$, calculated with the steady state model.

- *E. Young et al.* (2009) [21] - In this work, a stabilizer-free YBCO coated conductor the minimal quench energies are measured in a temperature range of $30 - 70\ K$ with a current up to $212\ A$ between 40 ans 100 $\%Ic$. However only the data on the MQE is available. It ranges between 3 and 20 mJ. This is significantly lower than the MQE from the other papers.
- *H. Park et al.* (2010) [22] - In this work, a tape with copper stabilizer from SuperPower is measured (which is similar to the tape used for this report). The temperature of the sample is controlled using a cryocooler and experiments are performed at three temperatures 40, 65 and 77 K, without applied magnetic field. The data are presented as a percentage of the critical current. MQE is presented at 50, 70, 90 and 100 $\%Ic$ and lies in the range of $0.25 - 2.5\ J$. For V_{nzp} only 50 $\%Ic$ is presented at which the velocity is in the range of $7 - 16\ mm/s$.
- *W. Lu et al.* (2012) [23] - In this work, the normal zone propagation is measured in a pancake coil configuration. Measurements are performed at liquid nitrogen temperature of 77 K. The longitudinal velocities found for the tape are in the range of $0 - 10\ mm/s$.

Literature data have been acquired from a variety of different conductors, with and without copper stabilizer, with different sample widths and with various production processes from different manufacturers. In addition most of the literature data are measured at temperatures over 50 K, in zero applied magnetic field. This makes it hard, if not impossible, to compare any of the data directly to the data presented in this report.

However from the data in the literature some relevant global trends, for temperatures above 50 K, can be observed. Firstly, as can be most clearly observed in *Wang et al.* and in *Park et al.* [18, 22], quench energies at a fixed percentage of the critical current, decrease with temperature. Combined with the data in this report, where the minimal quench energies increase with the temperature in the temperature range of $23 - 47\ K$ (Figure 3.4), this suggests that there may be a maximum somewhere in the proximity of 50 K. This would resemble the situation found in MgB_2 [15] where, as discussed in Section 1.5, the competition between increasing heat capacity and decreasing thermal margin leads to a non-monotonic $MQE(T)$ behavior. Unfortunately, in its present form our set-up does not allow to access temperatures above 50 K, so that this observation cannot be confirmed directly without major changes to the sample holder (see also the 'Suggestions' section below). In contrast to MQE and to the $V_{nzp}(T)$ behaviour in MgB_2, the normal zone velocities continue to decrease with increasing temperature at fixed percentages of the critical current. Another more general observation from the literature is that most authors choose not to compensate their data for the efficiency of the heater used (since it is simply unknown and doesn't affect the trends observed within the dataset). This explains the significant variation in the minimum quench energy (in contrast to the normal zone propagation velocity) found throughout literature.

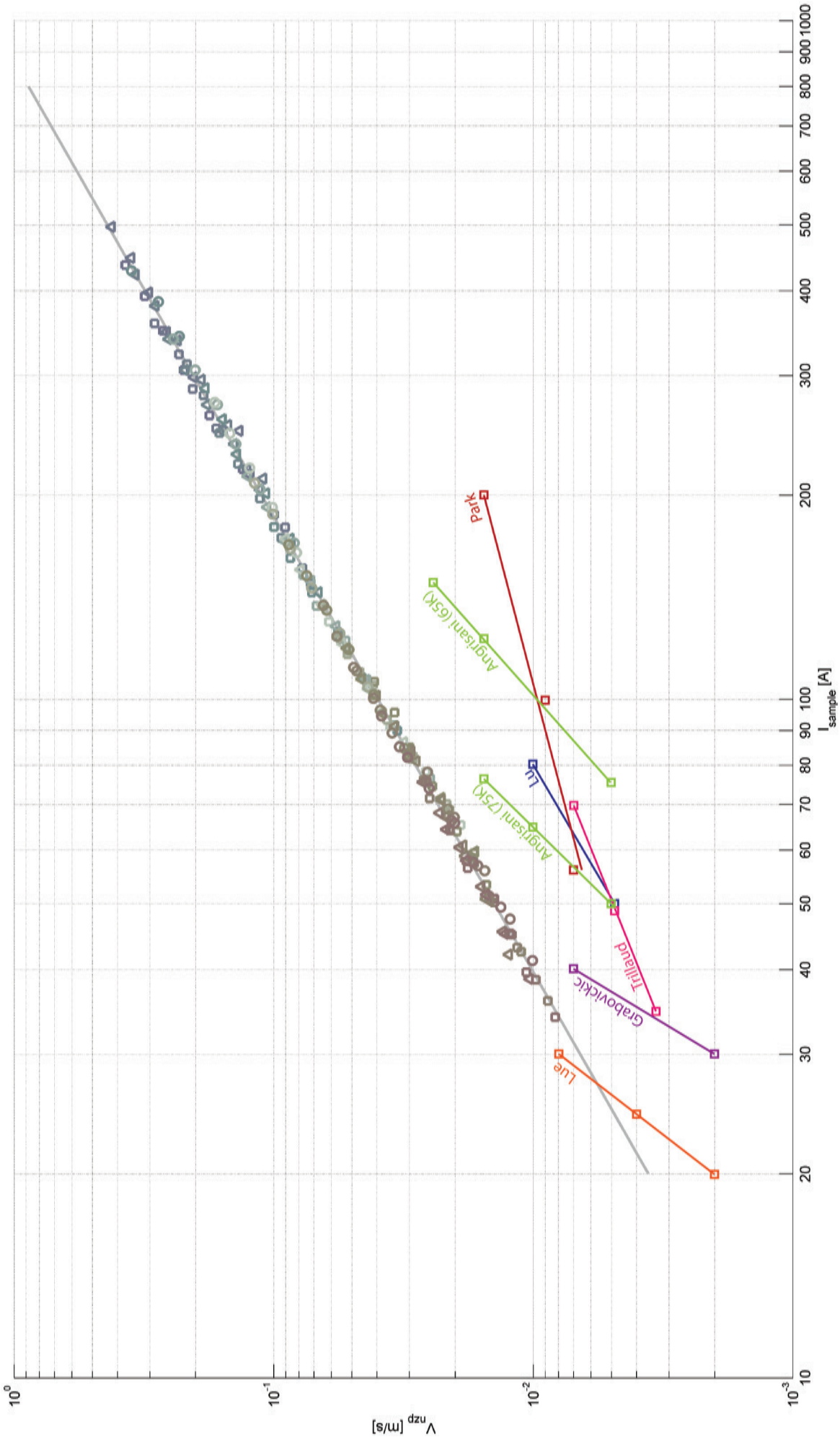

Figure 4.18: Overview of the normal zone propagation velocity plotted against the current on a log-log scale, comparing the measured data from this report to the data from the literature.

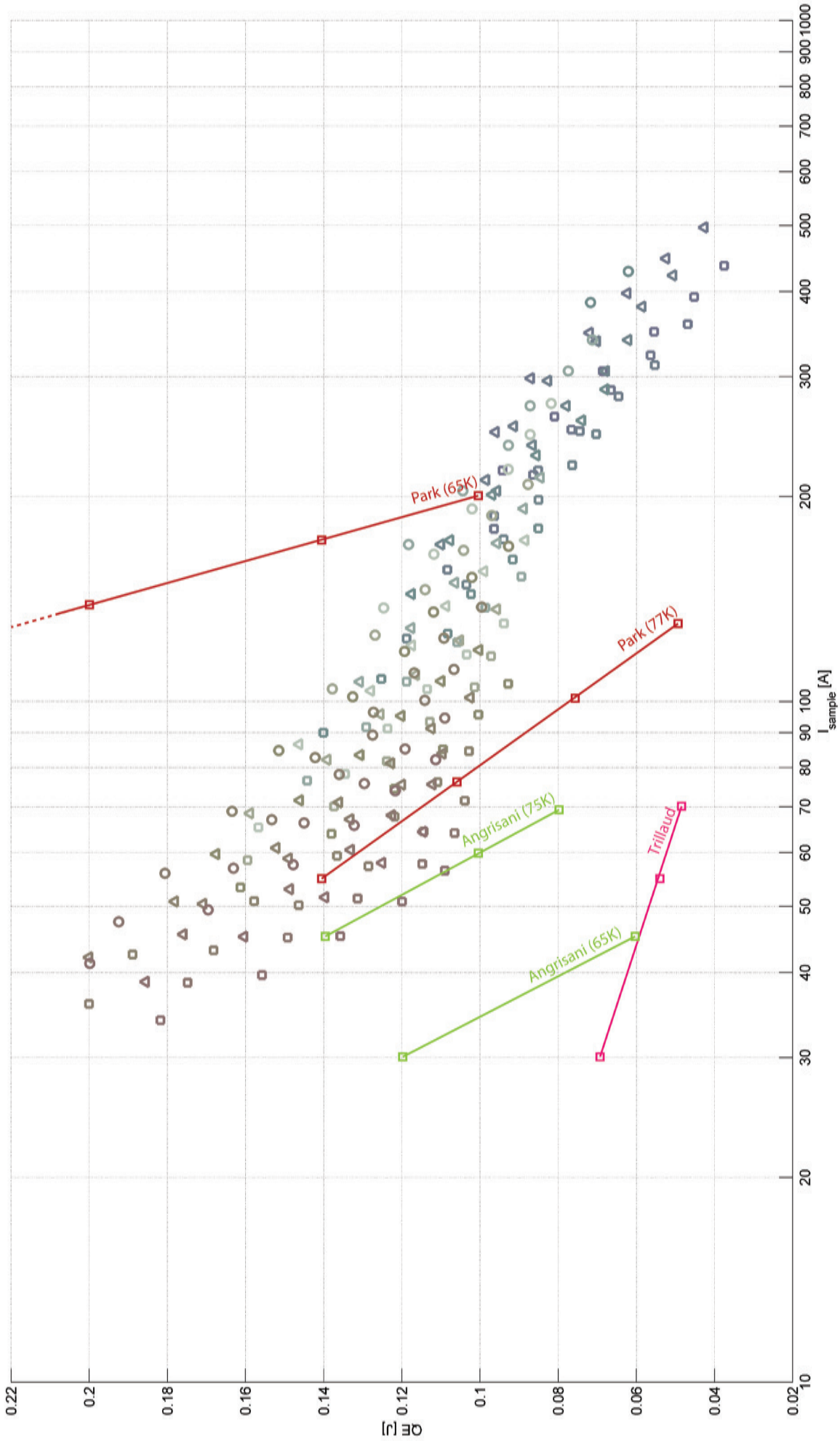

Figure 4.19: Overview of the minimum quench energies plotted against the current on a semi-log scale, comparing the measured data from this report to the data from the literature. Since in most works the heater efficiencies were not compensated for, to allow for a fair comparison the data from these works is scaled with the same heater efficiency, that is used for the data in this report (20 %).

Discussion and Conclusion

In this report the measurement of the normal zone propagation velocity and the minimal quench energy of a YBCO coated conductor SCS4050 is described, as function of temperature, percentage of the critical current and applied magnetic field. The measurements are performed using a pre-existing set-up originally created for the measurement of normal zone behaviour in magnesium di-boride MgB_2 wires. Because the set-up is not used for a while, it is necessary to reassemble all the necessary instrumentation. This also led to the introduction of a new data acquisition system based on Labview and NiDAQ. In addition, the embedded heater which was used in the experiment to control the temperature of the sample, needed to be replaced. In the process, the heater and its current leads were upgraded to a more robust design.

One of the main challenges was to find a good design for the quench heater. After some experimentation it was decided to use a surface mounted resistor, stuck to the tape with alumina-loaded epoxy. Another challenge was finding a good layout for all other components mounted on the tape during the experiment (extra heaters, temperature sensors and voltage taps). It was for example required to reduce the distance between the voltage taps to 5 mm. Eventually, after a learning curve, the experimental set-up performed well and it was possible to produce a large dataset, measured at magnetic fields of 6, 10 and 14 T applied parallel to the tape, for currents between $50 - 100$ $\%Ic$ and for temperatures ranging between 23 and 47 K. The temperature was limited at the high end by the vaporization of the helium and at the lower end by the critical current of the current leads inside the set-up.

The results of the measurement show that the normal zone propagation velocity (in the range investigated) seems to depend only on the current through a simple power law relation. The minimal quench energies depend on all measured environmental parameters B, T and I. The measured data were then compared to analytical and numerical descriptions for the normal zone propagation and the minimal quench energy. For the normal zone velocity, after introducing a small but non-zero cooling term, a good agreement is found between the measurements and both the analytical and numerical models. This means that the conditions under which the experiment is performed are only quasi-adiabatic as opposed to fully adiabatic. For the measurements described in this report, it was necessary to fit the cooling in the models to the measured data afterwards. However, if similar measurements are performed again, the minimum propagation current should be measured directly, since this allows to determine heat loss to the environment directly. For the minimum quench energies the quantitative behaviour of the measured data is similar to the model predictions. Differences between the model and the measurements are caused by the inability to compensate correctly for the efficiency of the heater, which is unknown because the thermal resistance of the boundary between the heater and the tape is difficult to determine. Therefore the results of the time dependent numerical model, in which the heat pulse is deposited directly into the nodes representing the tape, might be more useful.

To conclude: the experimental set-up and its instrumentation have been reassembled and improved successfully and it is now possible to acquire a large dataset on the normal zone behaviour of YBCO coated conductor SCS4050. The data are compared to numerical and analytical models. Good agreement is found between data and models for the normal zone propagation velocity, while the origin of quantitative discrepancies between experiment and models for the minimum quench energy is understood.

Suggestions

One of the goals for the experiment is to gain experience with this type of experiments. Based on the experience a few suggestions on how to improve the experiment are provided:

- It is recommended to measure the minimal propagation current [17]. To avoid overloading the heater it is possibly better to start the quench using a short over current.
- In order to have a larger distance over which the propagation velocity can be measured, more voltage taps and Ectron 751ELN DC-Amplifiers can be used (in the enclosure there are two additional slots available). Measuring over a longer distance allows the experiment to measure over a larger current range, while avoiding the initialisation transients.
- It is very important to avoid heat leaks by using high resistivity wire, such as manganin 0.1-0.2 mm, near the sample. The reader is referred to Ekin for more information on minimizing heat leaks [40].
- It is best not to use the vacuum tube for wiring since this creates a thermal path towards room temperature.
- In future experiments wire feedthroughs from the liquid helium towards the vacuum needs to be more robust, avoiding the risk of wires breaking. This can be done by encapsulating a flexible PCB, leading from outside the vacuum chamber into the experiment, in aluminium loaded epoxy and soldering the wires directly on it.
- More space is required to make all the electrical connections.
- The computer models need a rewrite towards object oriented programming. This it much easier when performing a sensitivity analysis.
- For YBCO tapes is proven that a short length is sufficient to measure. The total layout on the tape surface is no longer than 150 mm. If a new sample holder is constructed it may be sufficient to make only 1 or 2 turns.
- The current leads that are currently in the experiment start vaporizing a lot of helium at currents over 500 A. If a current over this level is required it may be necessary to use vapour cooling.
- The superconducting part of the current leads should be made of multiple layers of YBCO coated conductor. This allows for measurements at higher magnetic field and for measurements in liquid nitrogen at 77 K.
- The current leads should be soldered to the vacuum chamber at an easy to reach place. This can be achieved by extending the copper of the bottom flange outside the helium channel.
- Initialising the quench using a heater on the tape causes the heater to influence the experiment. Also because of the thermal boundary between the heater and the sample it is hard to determine the minimal quench energy. This problem may be solved by quench initialization with a single pulse laser and an optical fibre running into the cryostat [19].
- The 15 T magnet at the Twente Facility has an 80 mm bore. This makes it possible to use a larger sample holder.

Based on these suggestions a conceptual design for a new sample holder is presented in the schematic drawing on the next page.

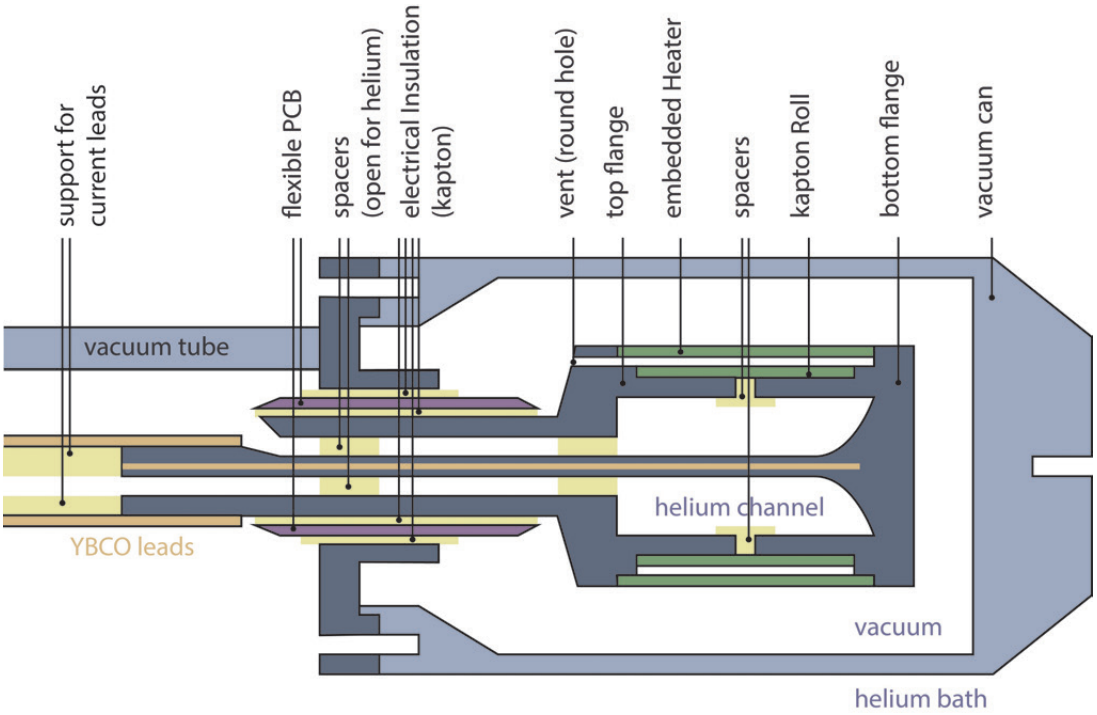

Conceptual design for a new sample holder.

Bibliography

[1] M. Tinkham, *Introduction to Superconductivity*. Dover, second ed., 2004.

[2] M. Cyrot and D. Pavuna, *Introduction to Superconductivity and High-Tc Materials*. World Scientific, 1992.

[3] H. K. Onnes, "Sur les Résistances Électriques," *Communications from the Physical Laboratory of the University of Leiden*, pp. 1–11, 1911. Supplement 29.

[4] M. Wu, J. Ashburn, C. Torng, *et al.*, "Superconductivity at 93 K in a New Mixed-Phase Y-Ba-Cu-O Compound System at Ambient Pressure," *Physical Review Letters*, vol. 58, no. 9, pp. 908–910, 1987.

[5] L. Bottura, "A Practical fit for the Critical Surface of *NbTi*," *IEEE Transactions on Applied Superconductivity*, vol. 10, no. 1, pp. 1054–1057, 2000.

[6] M. S. Lubell, "Empirical Scaling Formulas for Critical Current and Critical Field for Commercial NbTi.," *IEEE Transactions on Magnetics*, vol. MAG-19, no. 3 Pt 1, pp. 754–757, 1982.

[7] A. Godeke, "Performance Boundaries in Nb_3Sn Superconductors," Master's thesis, Twente University, 2005.

[8] M. Y. Sekitani, T and N. Miura, "Measurement of the Upper Critical field of Optimally-Doped $YBa_2Cu_3O_{7-\delta}$ in Megagauss Magnetic Fields," *New Journal of Physics*, vol. 9, no. 47, pp. 1–11, 2007.

[9] H. Maeda, Y. Tanaka, M. Fukutumi, and T. Asano, "A New High-Tc Oxide Superconductor Without a Rare Earth Element," *Japanese Journal of Applied Physics*, vol. 27, no. 2, pp. L209–L210, 1988.

[10] A. Golovashkin, O. Ivanenko, Y. Kudasov, *et al.*, "Low Temperature Direct Measurements of H_{c2} in HTSC Using Megagauss Magnetic Fields," *Physica B: Condensed Matter*, vol. 177, pp. 1859–1860, March 1922.

[11] G. Snitchler, "Progress on High Temperature Superconductor Propulsion Motors and Direct Drive Wind Generators," *International Power Electronics Conference*, 2010.

[12] N. Maki, "Design study of High-Temperature Superconducting Generators for Wind Power Systems," *Journal of Physics: Conference Series*, vol. 97, 2007.

[13] P. Tixador, "Development of Superconducting Power Devices in Europe," *Physica C*, vol. 470, pp. 971–979, 2010.

[14] R. Assmann, R. Bailey, O. Brüning, *et al.*, "First Thoughts on a Higher-Energy LHC," tech. rep., CERN, 2010.

[15] H. van Weeren, *Magnesium Diboride Superconductors for Magnet Applications*. PhD thesis, University of Twente, 2007.

[16] J. Lue, M. Gouge, R. Duckworth, *et al.*, "Quench tests of a 20-cm-long RABiTS YBCO tape," *IEEE Transactions on applied superconductivity*, vol. 13, p. 1726, 2003.

[17] R. Grabovickic, J. Lue, M. Gouge, *et al.*, "Measurements of Temperature Dependence of the Stability and Quench Propagation of a 20-cm-Long RABiTS Y-Ba-Cu-O Tape," *IEEE Transactions on applied superconductivity*, vol. 13, pp. 1726–1730, June 2003.

[18] X. Wang, A. Caruso, and M. Breschi, "Normal Zone Initiation and Propagation in Y-Ba-Cu-O Coated Conductors With Cu Stabilizer," *IEEE Transactions on applied superconductivity*, vol. 15, no. 2, pp. 2586–2589, 2005.

[19] F. Trillaud, F. Ayela, A. Devred, *et al.*, "Quench Propagation Ignition using Single-Mode Diode Laser," *Applied Superconductivity*, vol. 15, no. 2, pp. 3648–3651, 2005.

[20] A. Angrisani Armenio, A. Augieri, and G. Celentano, "Stability Measurements on YBCO Coated Conductors," *IEEE Transactions on applied superconductivity*, vol. 18, pp. 1293–1296, June 2008.

[21] E. Young, C. Friend, and Y. Yang, "Quench Characteristics of a Stabilizer-Free 2G HTS Conductor," *IEEE Transactions on applied superconductivity*, vol. 19, pp. 2500–2503, June 2009.

[22] H. Park, A. Kim, M. Park, *et al.*, "Analysis of Temperature Dependent Quench Characteristics of the YBCO Coated Conductor," *IEEE transactions on applied superconductivity*, vol. 20, pp. 2122–2125, June 2010.

[23] W. Lu, J. Fang, D. Li, *et al.*, "The Experimental Research and Analysis on the Quench Propagation of YBCO Coated Conductor and Coil," *Physica C*, 2012.

[24] H. ten Kate, H. Boschman, and L. van de Klundert, "Longitudinal Propagation Velocity of the Normal Zone in Superconducting Wires," *IEEE Transactions on applied superconductivity*, vol. 23, pp. 1557–1560, March 1987.

[25] H. Boschman, *On the Resistive Transition of Composite Superconductors*. PhD thesis, University of Twente, 1991.

[26] Z. Mei, H. Holder, and H. van der Plas, "Low-Temperature Solders," *Hewlett-Packard Journal*, 1996.

[27] B. ten Haken, *Strain Effects on the Critical Properties of High-Field Superconductors*. PhD thesis, University of Twente, 1994.

[28] B. ten Haken and H. ten Kate, "The Degradation of the Critical Current Density in a Nb_3Sn Tape Conductor due to Parallel and Transversal strain," *Fusion Engineering and Design*, vol. 20, pp. 265–270, 1993.

[29] Y. Lecrevisse *et al.*, "Critical Current and Junction Between Pancake Studies for HTS Coil Design," tech. rep., CERN, EuCARD, May 2012.

[30] A. Kosse, A. Prokhorov, and V. Khokhlov, "Measurements of the Magnetic Field and Temperature Dependences of the Critical Current in YBCO Films and Procedures for an Appropriate Theoretical Model Selection," *Superconductor Science and Technology*, vol. 27, no. 7, 2008.

[31] A. Otsuka, T. Kiyoshi, and M. Takeda, "A 1.3 GHz NMR Magnet Design under High Hoop Stress Condition," *IEEE Transactions on applied superconductivity*, vol. 20, pp. 596–599, 2010.

[32] Ectron Corporation, 8159 Engineer Road, San Diego, CA 922111-1907, *Instruction Manual: 751ELN DC Amplifier*, 2010. website: www.ectron.com.

[33] A. Bejan, *Heat Transfer*. John Wiley & Sons, Inc, 1993.

[34] L. Dresner, "Analytic Solution for the Propagation Velocity in Superconducting Composites," *IEEE Transactions on Magnetics*, vol. 15, pp. 328–330, January 1979.

[35] R. Bellis and Y. Iwasa, "Quench Propagation in High T_c Superconductors," *Cryogenics*, vol. 34, no. 2, pp. 129–144, 1994.

[36] V. Johnson and R. Stewart, "A Compendium of the Properties of Materials at Low Temperature (phase I)," tech. rep., National Bureau of Standard, 1960.

[37] Y. Iwasa, *Case Studies in Superconducting Magnets*. Springer Science, 2nd ed., 2009.

[38] M. Wilson, *Superconducting Magnets*. Oxford Science Publications, March 1987.

[39] G. Recktenwald, "Finite-Difference Approximations to the Heat Equation," tech. rep., Mechanical Engineering Department, Portland State University, March 2011.

[40] J. Ekin, *Experimental Techniques for Low-Temperature Measurements*. Oxford University Press, 2011.

[41] D. Matsumoto, C. Reynolds, and A. Anderson, "Thermal Boundary Resistance at Metal-Epoxy Interfaces," *Physical Review B*, vol. 16, pp. 3303–3307, October 1977.

[42] A. Verweij, *CUDI: Users Manual*. LHC-MMS, CERN, 2007.

[43] D. Smith and F. Fickett, "Low-Temperature Properties of Silver," *Journal of Research of the National Institute of Standards and Technology*, vol. 100, pp. 119–171, March-April 1995.

[44] A. Berger, "Stability of Superconducting Cables with Twisted Stacked YBCO Coated Conductors," tech. rep., Plasma Science and Fusion Center, Massachusetts Institute of Technology, February 2021.

[45] J. Lu, E. Choi, and H. Zhou, "Physical Properties of Hastelloy C-276 at Cryogenic Temperatures," *Journal of Applied Physics*, vol. 103, March 2008.

[46] N. Simon, E. Drexler, and R. Reed, "Properties of Copper and Copper Alloys at Cryogenic Temperature," *NIST Monograph*, vol. 177, pp. 7–23, February 1992.

[47] W. de Rapper, *Thermal Stability of Nb_3Sn Rutherford Cables for Accelerator Magnets*. PhD thesis, University of Twente, CERN, unsubmitted.

Appendix A Construction Protocol for the Embedded Heater

A schematic cross-section of the cylindrical heater assembly is shown in Figure 2.8 on Page 15. The construction of the heater is performed using the following steps:

1. First note that the heater needs to be trimmed at the end of the process. Make sure no wires or vital components are outside the area to be kept.
2. Several Kapton strips with a thickness of 0.07 *mm*, a width of 60 *mm* and a length of 500 *mm* need to be cut. It is easiest to use a ruler and several clamps to affix the kapton before cutting it.
3. Cut a copper foil, with thickness 0.1 *mm*, to a width of 60 *mm* and a length equal to the circumference of the heater roll.
4. The surface of the Kapton strips is sanded lightly and cleaned with alcohol.
5. The Kapton strip is rolled onto a smooth former while clear epoxy is applied with a brush between the layers (the number of layers and their thickness can be found in Table 2.3). Avoid air from being trapped under the epoxy since this weakens the heater. The former can be sprayed with Teflon oil to ease the removal of the heater at the end of the process.
6. Wrap the heater roll in Teflon tape and dry it using a hair dryer. Do this preferably while it is rotating on a lathe.
7. After the heater roll is dry, wind a Phosphor Bronze (works really well) or manganin wire onto the heater roll. Use a nail at each end to fix the wire to the heater roll.
8. Use a scalpel to remove the insulation layer from the wire and solder the current leads to it with high temperature solder (The heater now resembles the heater depicted in Figure A.1).
9. Fold a Kapton strip over the copper sheet such that both ends extend over the edge of the copper. Use Figure 2.8 for reference.
10. Use clear epoxy to bond the copper and Kapton to the heater roll, while guiding the current leads through the opening. To avoid shorts make sure that the current leads can not touch the copper sheet in any way. The use of Kapton tape and Teflon tape may be very useful here (an extra pair of helping hands is recommended as well).
11. Wrap the heater roll in Teflon tape again and dry it using a hair dryer. Preferably while it is rotating on a lathe.
12. Glue the connector pad to the heater using loaded epoxy and after the epoxy has dried solder the current leads to it with high temperature solder.
13. Apply several extra layers of Kapton to the heater.
14. Cut the heater into its final length using a metal saw. It is easiest to put the former in the lathe and fix the metal saw in position using a clamp.
15. Put nails in the former around the heater and wind nylon wire onto it. The nylon wire should be horizontal everywhere and can be tightened using some Teflon tape (See Figure A.2).
16. Use clear epoxy to fix the nylon wires to the heater and let it dry. Don't use Teflon tape on the heater surface.
17. Cut the nylon wires at the edge of the heater and remove the heater from the former.
18. Glue a Kapton ring to the top and bottom of the heater with clear epoxy in order to avoid the copper foil making an electrical short circuit between the top and bottom current flanges of the overall set-up.

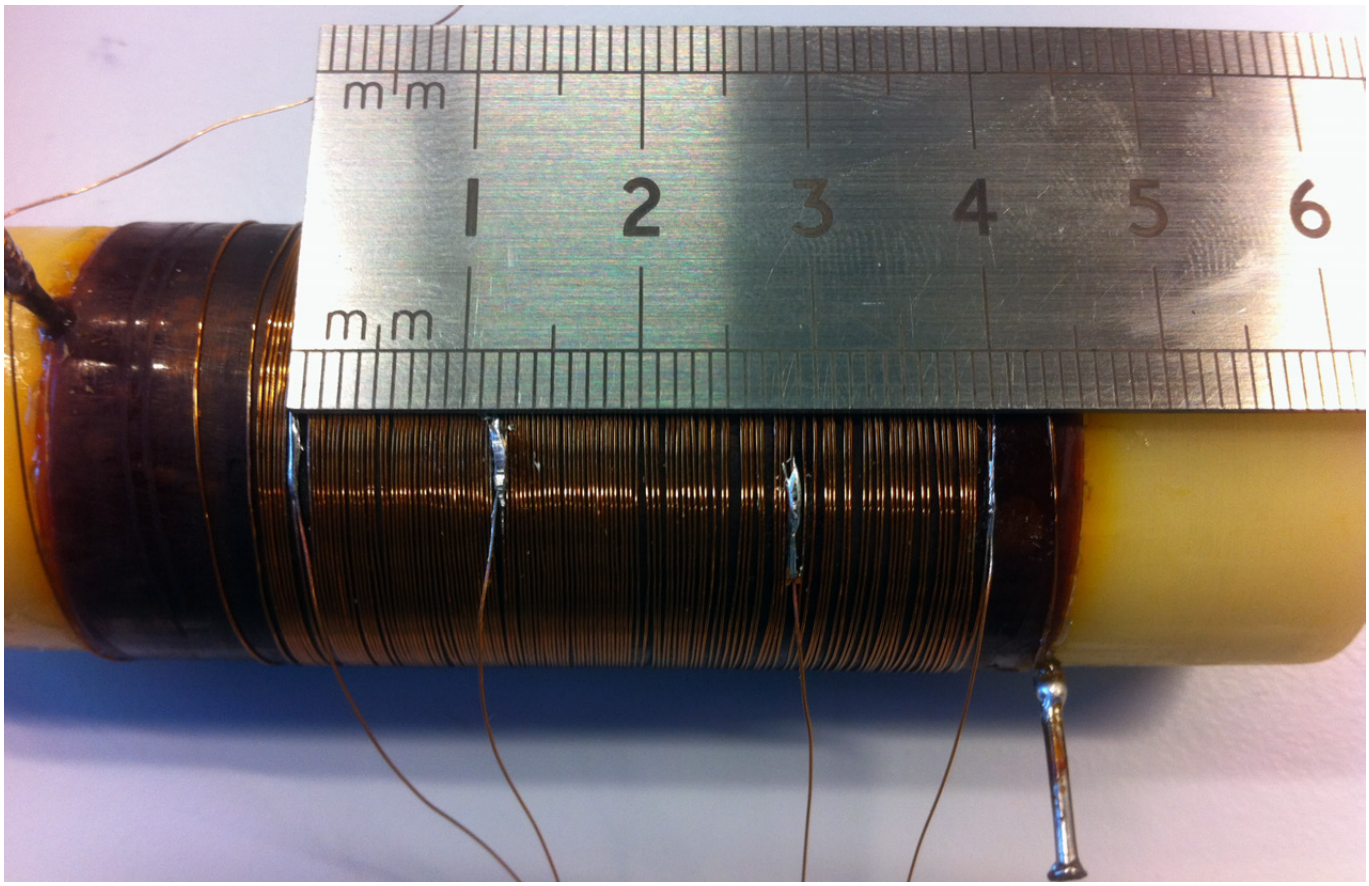

Figure A.1: Photograph of the phosphor bronze wires and the location of the current leads.

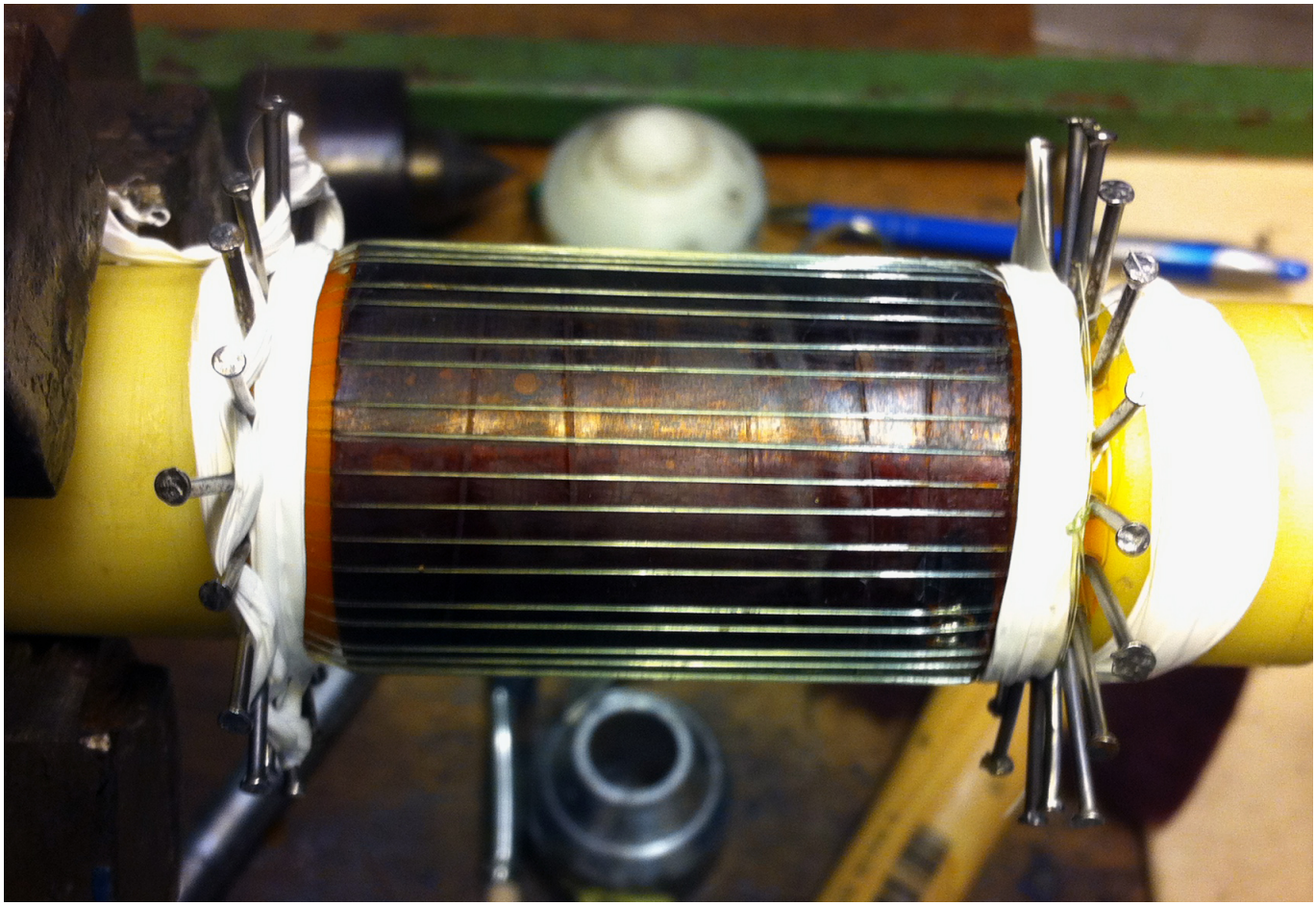

Figure A.2: Photograph of the nylon wires that form the surface ridges of the heater.

Appendix B Estimate of Thermal Time Constants

Throughout this report is referred to the experiment as 'quasi adiabatic' leading to the assumption - unless stated otherwise - that the amount of heat transported along the sample is 'much' more important than the amount of heat lost to the environment. This Appendix aims to quantify this assumption and also to clarify which conditions needs to be fulfilled for it to hold. The quasi-adiabatic assumption can also be stated in terms of thermal time constants: for an experiment to be adiabatic the time constant of the cooling of a local hotspot towards the environment must be many times larger than the time constant of heat transfer away from the hotspot towards the colder sample ends. An order-of-magnitude estimate is provided for these time constants.

Cooling to the Environment

The time constant of cooling is determined using the simple thermal network in Figure B.1. The temperature evolution of such a network can be described with a differential equation:

$$C\frac{dT}{dt} = h\,(T_b - T)\,, \tag{B.1}$$

where T_b is the temperature of the bath, T is the temperature of the conductor, C is the heat capacity of the tape and h is the thermal conductivity to the bath (throughout the report these are expressed as one-dimensional quantities (i.e. C in J/mK and h in W/mK. The solution of this straightforward differential equation is

$$T(t) = T_b + [T(0) - T_b]\, e^{-\frac{t}{\zeta_e}}, \tag{B.2}$$

with $T(0)$ the initial temperature and ζ_e the time constant of heat flow to the environment given by

$$\zeta_e = \frac{C}{h}. \tag{B.3}$$

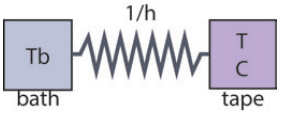

Figure B.1: Simple thermal network used for the estimate of the time constant for the sample cooling to the environment.

Heat Flow to Sample Ends

Heat flow along the sample depends of course on the thermal gradient involved. Since we want to estimate to what degree heat loss to the environment influences the propagation of a normal zone, we use the temperature profile and -evolution related to this process. The time constant for the heat flow to the sample ends can then be estimated using

$$\zeta_s = \frac{\ell_{char}}{V_{nzp}}, \tag{B.4}$$

where V_{nzp} is the normal zone velocity, ζ_s is the time constant for flow to the sample ends and ℓ_{char} is a characteristic length. This length is chosen to be the distance between the sample location at the transition temperature T_t and the location at the temperature of the helium bath T_b at the front of the normal zone. If the temperature profile is linearised, the length scale can be determined using

$$\ell_{char} = \frac{dz}{dT}\,(T_t - T_b)\,, \tag{B.5}$$

where the gradient dT/dz in the superconducting zone can be determined using transformed heat equation (see Equation 4.11 in Section 4.2.1 describing the static heat balance equation in reduced coordinates z). For a linearised system the solution of this equation can be written as

$$CV_{nzp}\frac{dT}{dz} = k\,(T_b - T)\,, \tag{B.6}$$

where k is the heat transfer coefficient in the longitudinal direction of the tape (again in one-dimensional units of Wm/K). Combining Equations B.4, B.5 and B.6 the typical time constant for heat flow along the tape during normal zone propagation becomes

$$\zeta_s = \frac{k}{CV_{nzp}^2}. \tag{B.7}$$

Degree of Adiabaticity

For a quench to be (quasi-) adiabatic, heat transfer to the environment must be a much slower process than heat transfer towards the ends of the tape, i.e. $\zeta_e >> \zeta s$. Using the expressions for the time constants in Equations B.3 and B.7, this condition can be rewritten as

$$h << \frac{C_s^2 V_{nzp}^2}{k}. \tag{B.8}$$

As illustration, some typical numbers are inserted into this equation. Assuming a background temperature $T_{op} = 30\ K$, Figure 4.3 shows that $C \approx 0.1\ J/mK$ and $k \approx 10^{-4}\ Wm/K$. Comparison between the measured data and the analytical (Figure 4.4) or the numerical (Figure 4.10 - 4.12) models, shows that $h \approx 0.1\ W/mk$. Applying Equation B.3 then gives $\zeta_e \approx 1\ s$. Note that this is a rather conservative estimate, since experience with the background temperature regulation (see Section 2.4) suggests that this value might be closer to $\zeta_e \approx 10\ s$. At a field of 14 T and a curent of 200 A, v_{nzp} was found to be $\sim 0.1\ m/s$. Using Equation B.7 this yields $zeta_s = 0.1\ s$, i.e. under these conditions heat flow along the sample is about one decade faster than heat loss to the environment. Although these typical values of the two time constants confirm the quasi-adiabatic assumption, their difference is not that large that heat flow to the environment can be totally neglected. As discussed in Section 4.2.1 and Section 4.3.3, corrections to the model that take into account this heat loss indeed lead to better correspondence between model and experiment, especially when currents become lower (and therefore V_{nzp} slower).

Appendix C Lakeshore Calibration Curves

Lakeshore provides their thermometers with calibration curves. For convenience the calibration curves for the used thermometers are reproduced also here. For the $X31553$ and $X31554$ the temperature is calculated as

$$T = A_0 + A_1 k + A_2(2k^2 - 1) + A_3(4k^3 - 3k) + A_4(8k^4 - 8k^2 + 1) + A_5(16k^5 - 20k^3 + 5k) + A_6(32k^6 - 48k^4 + 18k^2 - 1),$$

and for the $X78396$ the temperature is calculated as

$$T = \sum_{i=0}^{9} A_i \cos(i \cdot \arccos(k)),$$

where A_n are the thermometer specific coefficients provided by Lakeshore and k is defined as

$$k = \frac{(Z - ZL) - (ZU - Z)}{ZU - ZL},$$

with

$$Z = \log 10(R).$$

ZL and ZU are additional coefficients provided by Lakeshore. For the $X78396$ the coefficients are provided for three separate temperature intervals. All coefficients are reproduced in Table C.1). Labview code that calculates the temperature using these calibration curves,was written and is furnished to.

S.N.	$X31553$	$X31554$	$X78396$	$X78396$	$X78396$
T_{range}	$4 - 300\ K$	$4 - 300\ K$	$1.4 - 14.2\ K$	$14.2 - 80.0\ K$	$80.0 - 325\ K$
R_{range}	all	all	$> 1492\ \Omega$	$355.8 - 1492\ \Omega$	$< 355.8\ \Omega$
ZL	2.548819199941	2.50886625093846	3.1266152229	2.50703224814	1.99350254985
ZU	3.68666307673625981	3.63030580790044022	4.77536680078999964	3.23033708314999979	2.60083194192000011
A_0	20.08672	20.20759	5.393251	42.131764	176.739948
A_1	-21.91403	-22.00058	-6.238169	-37.681744	-126.748839
A_2	7.57565	7.47398	2.877497	8.809913	22.69694
A_3	-1.74904	-1.66282	-1.123111	-1.23584	-3.142686
A_4	0.25846	0.23235	0.374544	0.136807	0.566372
A_5	-0.02901	-0.03056	-0.103769	-0.007651	-0.106293
A_6	0.00799	0.00799	0.021473	-0.00568	0.012742
A_7	0	0	-0.001899	0.001339	0
A_8	0	0	-0.001187	-0.000362	0
A_9	0	0	0.000917	0.001516	0

Table C.1: Coefficients for calibration curves of the Lakeshore thermometers.

Appendix D Superpower SCS4050 EI-Curves

In Figure D.1, D.2 and D.3 on the next three pages, the Electric field as function of the current can be found for Superpower SCS4050 YBCO coated conductor for the respective magnetic fields of 6, 10 and 14 T parallel to the tape.

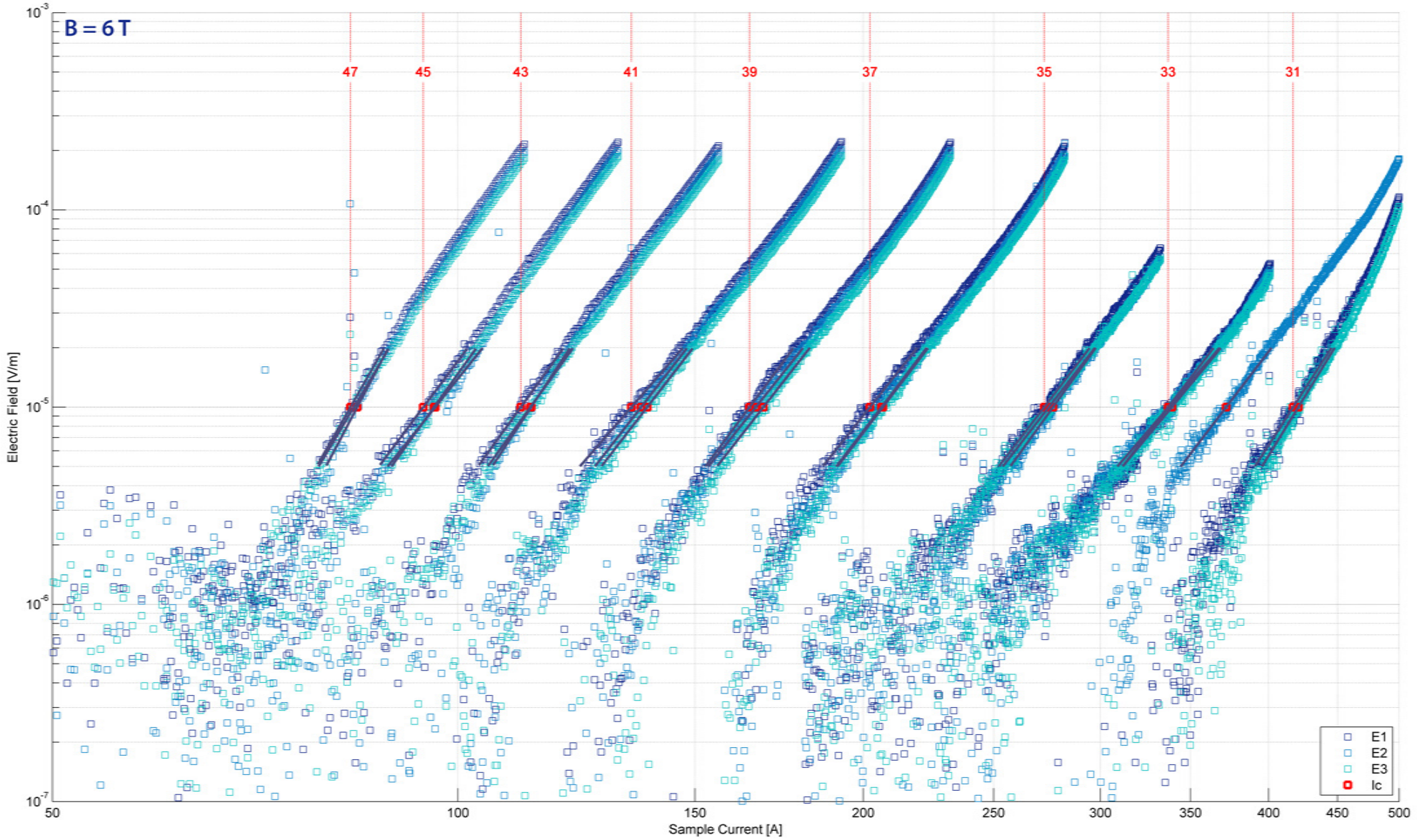

Figure D.1: Measured electric field plotted against current for Superpower SCS4050 YBCO coated conductor at a magnetic field of 6 T parallel to the tape. The red squares indicate the critical current and the corresponding numbers annotate the temperature. Different colors refer to the three different voltage pairs. The solid lines fitted around $E_0 = 10\ \mu V/m$ represent the customary power-law behaviour $E = E_0 [I/I_c]^N$ used to analyse such superconductor $E(I)$ data.

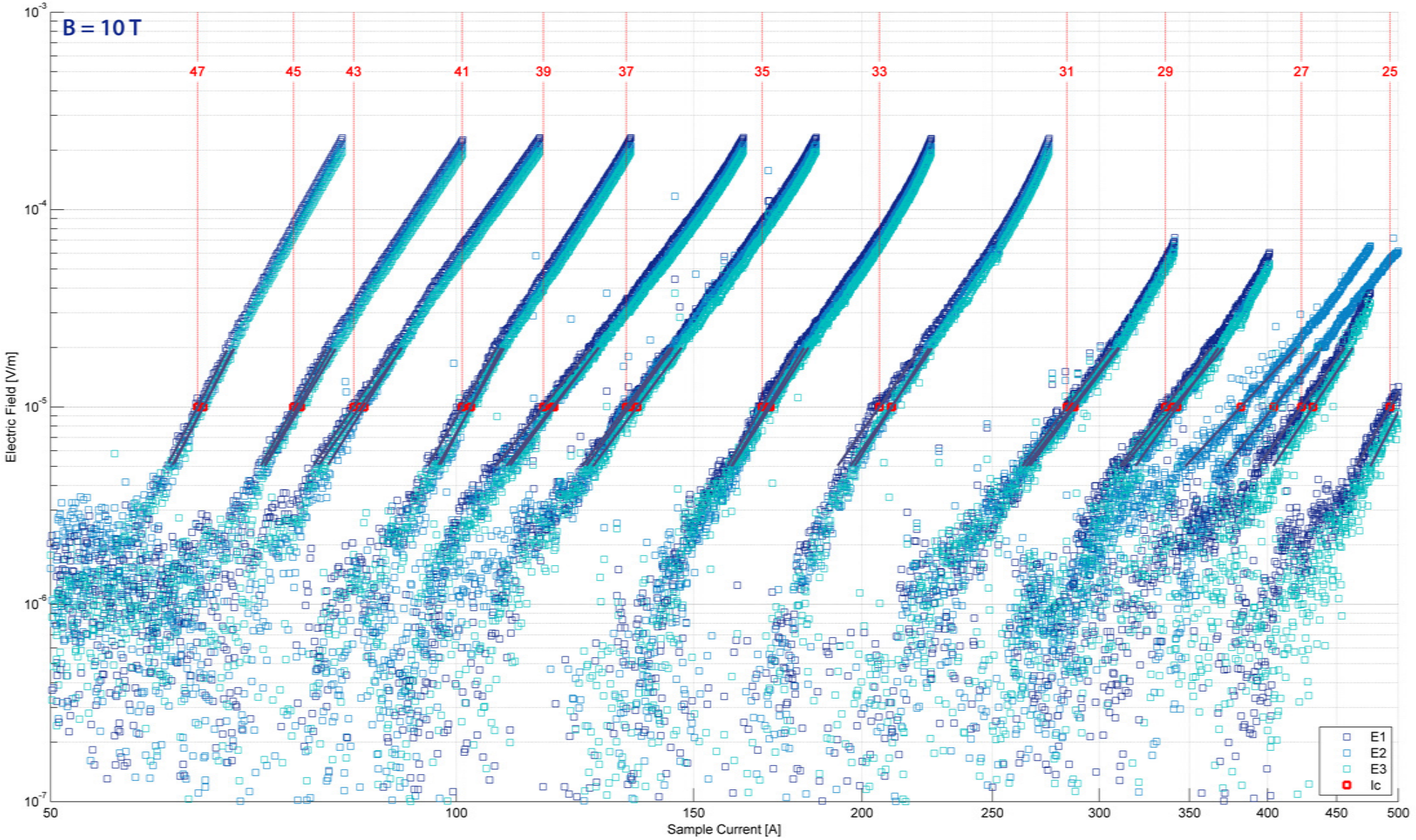

Figure D.2: Measured electric field plotted against current for Superpower SCS4050 YBCO coated conductor at a magnetic field of 10 T parallel to the tape. The red squares indicate the critical current and the corresponding numbers annotate the temperature. Different colors refer to the three different voltage pairs. The solid lines fitted around $E_0 = 10\ \mu V/m$ represent the customary power-law behaviour $E = E_0 [I/I_c]^N$ used to analyse such superconductor $E(I)$ data.

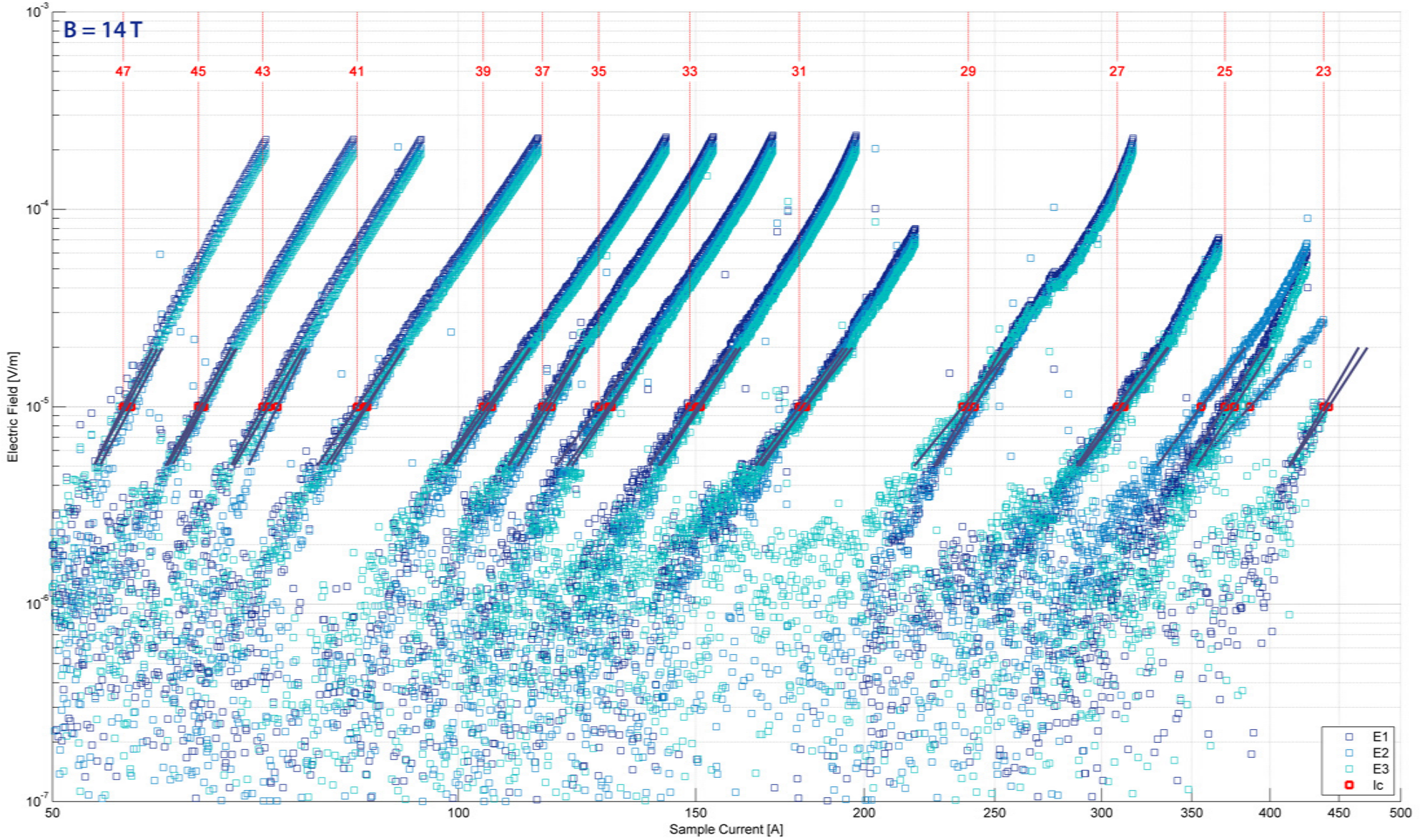

Figure D.3: Measured electric field plotted against current for Superpower SCS4050 YBCO coated conductor at a magnetic field of 14 T parallel to the tape. The red squares indicate the critical current and the corresponding numbers annotate the temperature. Different colors refer to the three different voltage pairs. The solid lines fitted around $E_0 = 10\ \mu V/m$ represent the customary power-law behaviour $E = E_0 [I/I_c]^N$ used to analyse such superconductor $E(I)$ data.

Appendix E Gorizont Results

Prior to the experiments on the YBCO coated conductors measurements have been performed on Nb_3Sn Gorizont tape to test the setup. To save helium, measurement was performed at only two temperatures. The critical current of this tape was determined at 8.0 T, at temperatures of 8.5K and 10 K. The measured critical current was respectively 168.4 A and 35.5 A. For the quench propagation the sizes of the voltage taps were L1 = 0.098 m, L2 = 0.108 m and L3 = 0.085 m. The development of the normal zone is presented in Figure E.1. It can be seen that when the quench enters the next voltage tap, the voltage saturates. This is because the sample inside the voltage tap is fully normal. The measured quench propagation velocities and quench energies are presented in Figure E.2. Note that for these measurements an older design for the quench heater was used which was later found to be in bad thermal contact with the tape (see Section 2.5).

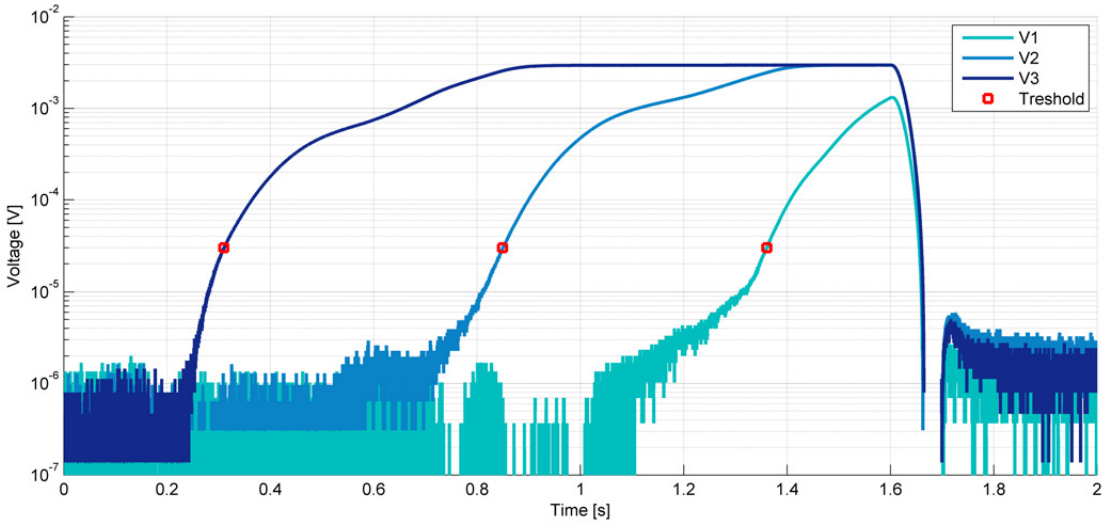

Figure E.1: Measured voltages over the voltage taps as function of time for a quench in a Gorizont tape at a start temperature of 10 K and a current of 32.2 A, which corresponds to 90 %I_c.

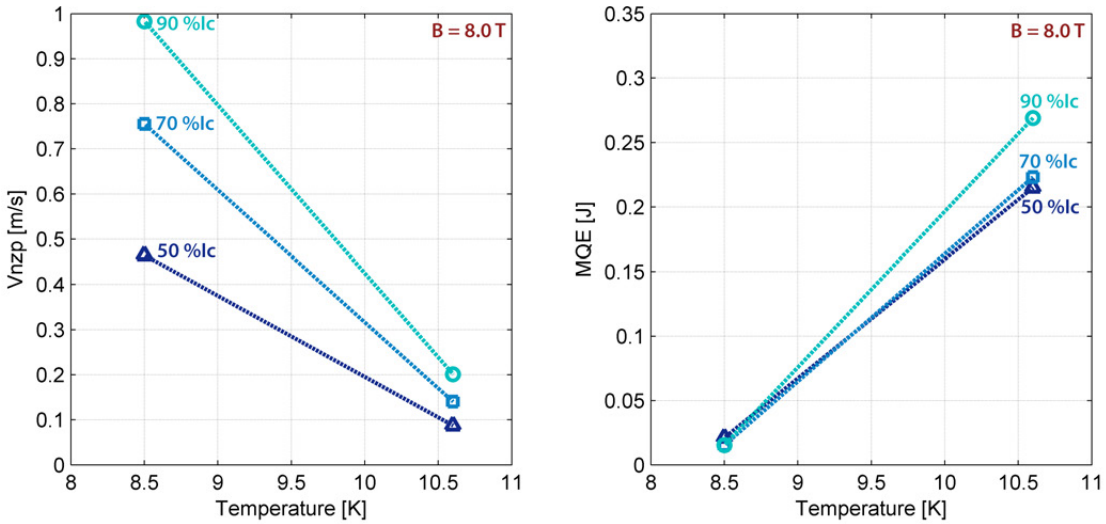

Figure E.2: Measured normal zone propagation velocity and quench energy as function of field, temperature and percentage of the critical current. Quench energies are not compensated for heater inefficiencies.

Appendix F Heater Model

Because the models are largely validated by the measurements, it is possible to study the behaviour of the heater with some confidence using a similar model. The goal of this study is to estimate the heater efficiency. This is done by attaching a model of the SMD resistor to the transient model (See Figure F.1). In this model the pulse energy is deposited inside the heater node instead of the tape. The model compensates for the fact that manganin current leads were used in which part of the energy is dissipated. The SMD resistor is basically an Alumina plate with a thick-film electrical resistor on top. The thermal resistance between the resistor and the tape is then calculated by adding the thermal resistivity of the plate, the alumina-loaded epoxy and twice the contact resistance between the epoxy and a solid material. Unfortunately, not much information is available on the cryogenic thermal contact resistance between an epoxy and a solid. The best value found in literature for the boundary resistance was $8.4 \times 10^{-5}\ Km^2/W$, which is valid for an epoxy to solid boundary at 10 K [41]. The thermal capacity of the heater is the combined heat capacity of the plate and of the alumina-loaded epoxy.

As an example, the temperature development of the tape and the attached quench heater are calculated for a start temperature of 35 K and without current in the tape. The heater pulse has an energy of 0.8 J. The result is presented in Figure F.2. It can be seen that the peak temperature of the heater is much higher than the peak temperature of the tape and that the energy from the heater is only transferred slowly to the tape. The energy transferred to the tape, before its temperature reaches its maximum, is 0.16 J, which corresponds to 20 % of the input pulse. By evaluating the model at other temperatures it was found that the temperature has almost no influence on this percentage. Because this value is not influenced by the quench behaviour of the model, it was used to compensate the measurements for the heater efficiency. However, when a current of 115 A corresponding to 90 $\%Ic$ runs through the tape, the temperature development is different due to the self heating of the tape (See Figure F.3). The energy transferred from the heater now has a peak because at a certain point the tape is warmer than the heater resulting in a heat flux in the opposite direction. The energy transferred before this peak is estimated to be only 0.12 J, which corresponds to a heater efficiency of 15 %. At lower temperatures (and thus higher currents, up to 500 A) this value drops even further to 10 %.

This explains the differences between the measurements and the model when it comes down to quench energies. However using this model to compensate for the heater efficiencies when a current is present in the sample however would be bad practice because it would inherently replicate the results from the model. For the design of superconducting devices the results for the quench energy calculated with the time dependent model, without heater and cooling, are probably more accurate than the measurement (see Section 4.3.4 and Figure 4.14).

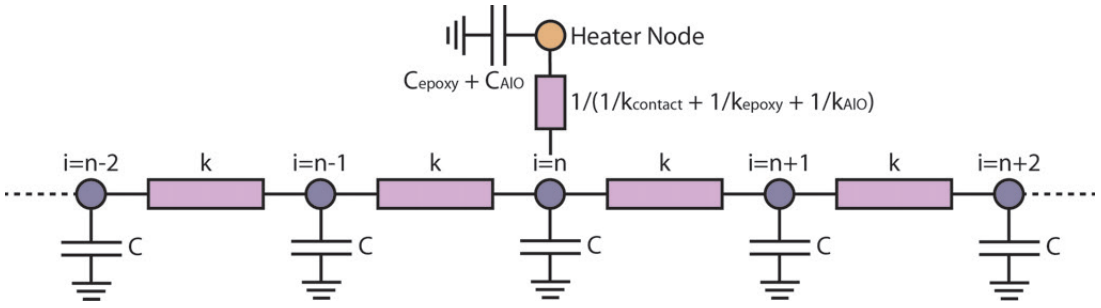

Figure F.1: Node representation of YBCO tape with heater.

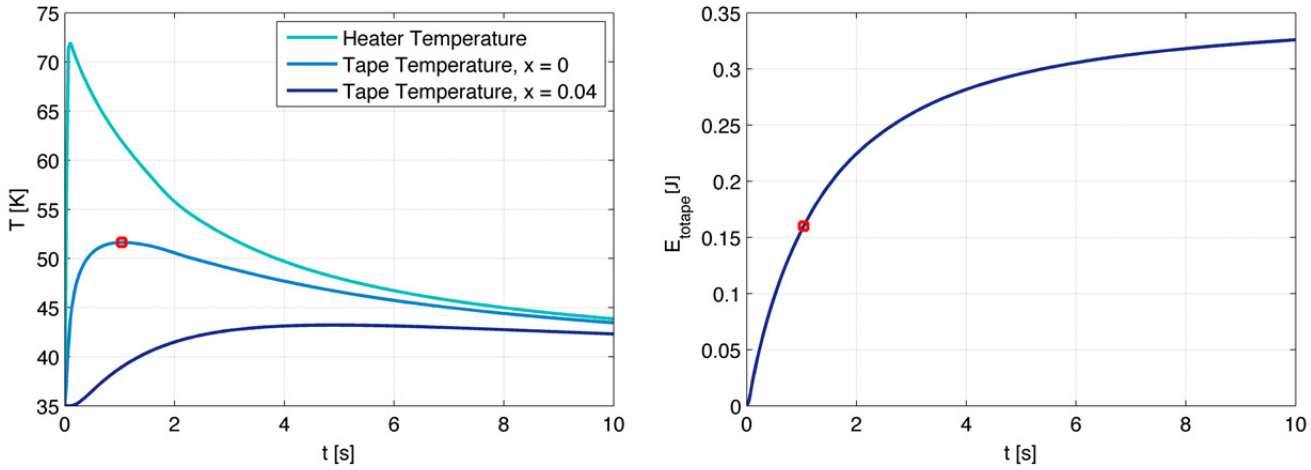

Figure F.2: Temperature development and heat transfer calculated with the heater model without current in the tape. The left plot shows the temperature evolution of the heater itself, of the tape immediately underneath the heater and of the tape 4 *cm* away from the heater. The red dot indicates the point where the tape reaches its highest temperature. The right plot shows the thermal energy absorbed by the tape. By the time it reaches its highest temperature, it has absorbed 160 *mJ*.

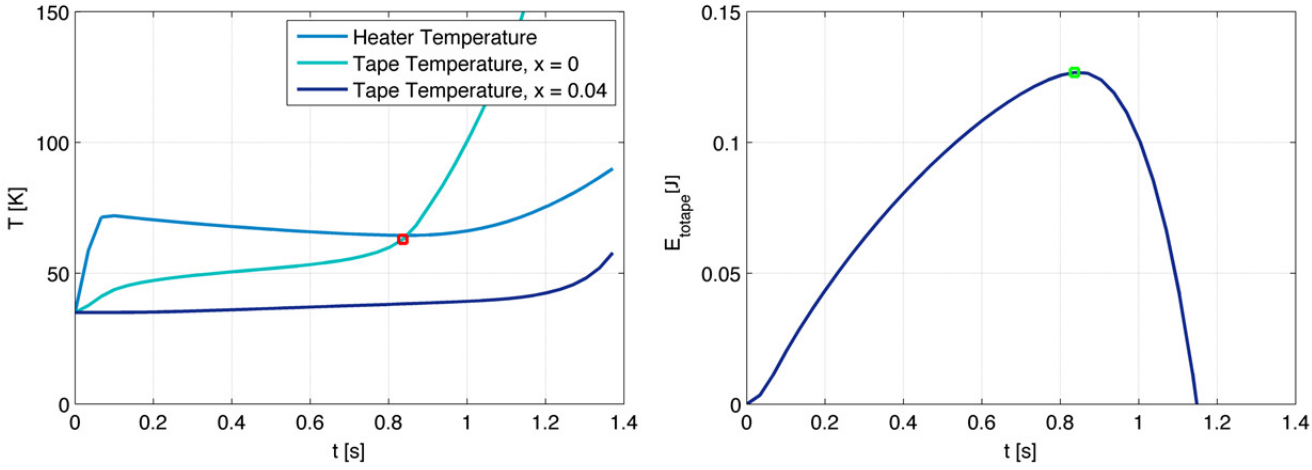

Figure F.3: Temperature development and heat transfer calculated with the heater model. The external heat pule itself is the same as in figure F.2, but this time the tape carries a current of 115 *A*. Note that the scale of both axis is different from Figure F.2. Instead of dropping again, like in Figure F.2, the temperature of the tape continues to rise due to ohmic self-heating, until it becomes warmer than the quench heater (red dot). At this point, the tape has absorbed 120mJ of heat from the heater.

Appendix G Material Properties

In this Appendix the material properties used for the numerical models are presented.

Electrical Resistivity

The electrical resistivity is an important parameter to the model for it determines the current sharing behaviour. The electrical resistivity is calculated from the properties of three materials: Copper, Silver and Hastelloy. The electrical resistivity of the tape, ρ_{tape} given in Ω/m can be calculated using

$$\rho_{tape}(RRR, B, T) = \left[\frac{w_{tape}h_{cu}}{\rho_{cu}(RRR, B, T)} + \frac{w_{tape}h_{hs}}{\rho_{hs}(T)} + \frac{w_{tape}h_{ag}}{\rho_{ag}(B, T)}\right]^{-1}, \tag{G.1}$$

where ρ_{cu}, ρ_{hs} and ρ_{ag} are respectively the electrical resistivities of copper, hastelloy and silver, given in the sections below; and where h_{cu}, h_{hs} and h_{ag} is the respective thickness of the layers. Note that the resistivity of the individual materials are given in Ωm while the resistivity of the tape is given in Ω/m. It should be noted that for the electrical properties of an coated conductor the influence of the copper is significantly higher than the other materials. Therefore it was proven to be more important to find an accurate fitting curve (that takes magneto-resistivity into account) for the electrical resistivity of the copper than for the other materials.

Copper

The CUDI manual [42] provides a perfect equation that takes both the RRR value and the magneto-resistance into account. The equation is given as

$$\rho_{cu}(RRR, B, T) = \left(\frac{C_0}{RRR} + \frac{1}{\frac{C_1}{T^5} + \frac{C_2}{T^3} + \frac{C_3}{T}}\right) \times 10^{-8} + B\,(0.37 + 0.0005 * RRR) \times 10^{-10}, \tag{G.2}$$

where the constants C_1, C_2, C_3 and C_4 are given in Table G.1. The equation is valid in a temperature range of $1 - 500\ K$ and a triple-R range of $5 - 400$. The RRR value is defined as $\rho_{T=290}/\rho_{T=4}$. As an example some curves are calculated with this equation (See Figure G.1 and Figure G.2.

Name	C_0 $[\Omega m]$	C_1 $[\Omega m K^5]$	C_2 $[\Omega m K^3]$	C_3 $[\Omega m K]$
Value	1.7	2.33×10^9	9.57×10^5	163

Table G.1: Coefficients for the scaling relation of the electrical resistivity of copper.

Silver

The electrical resistivity of silver is taken from NIST [43] and is given as function of temperature and magnetic fields of $0, 1, 2, 4, 6, 10, 14\ T$. If required the data is interpolated linearly. As an example a few curves have been plotted in Figure G.3.

Hastelloy C-276

Electrical resistivity of Hastelloy was taken from Berger [44, 45]. The engineering equation only depends on the temperature and is given as

$$\rho_{hs}(T) = (p_1 * T + p_2) \times 10^{-6} \qquad (T \leq 12), \tag{G.3}$$

$$\rho_{hs}(T) = (p_3 * T + p_4) \times 10^{-6} \qquad (T > 12), \tag{G.4}$$

$$\tag{G.5}$$

where constants P_1,P_2,P_3 and P_4 are presented in Table G.2.

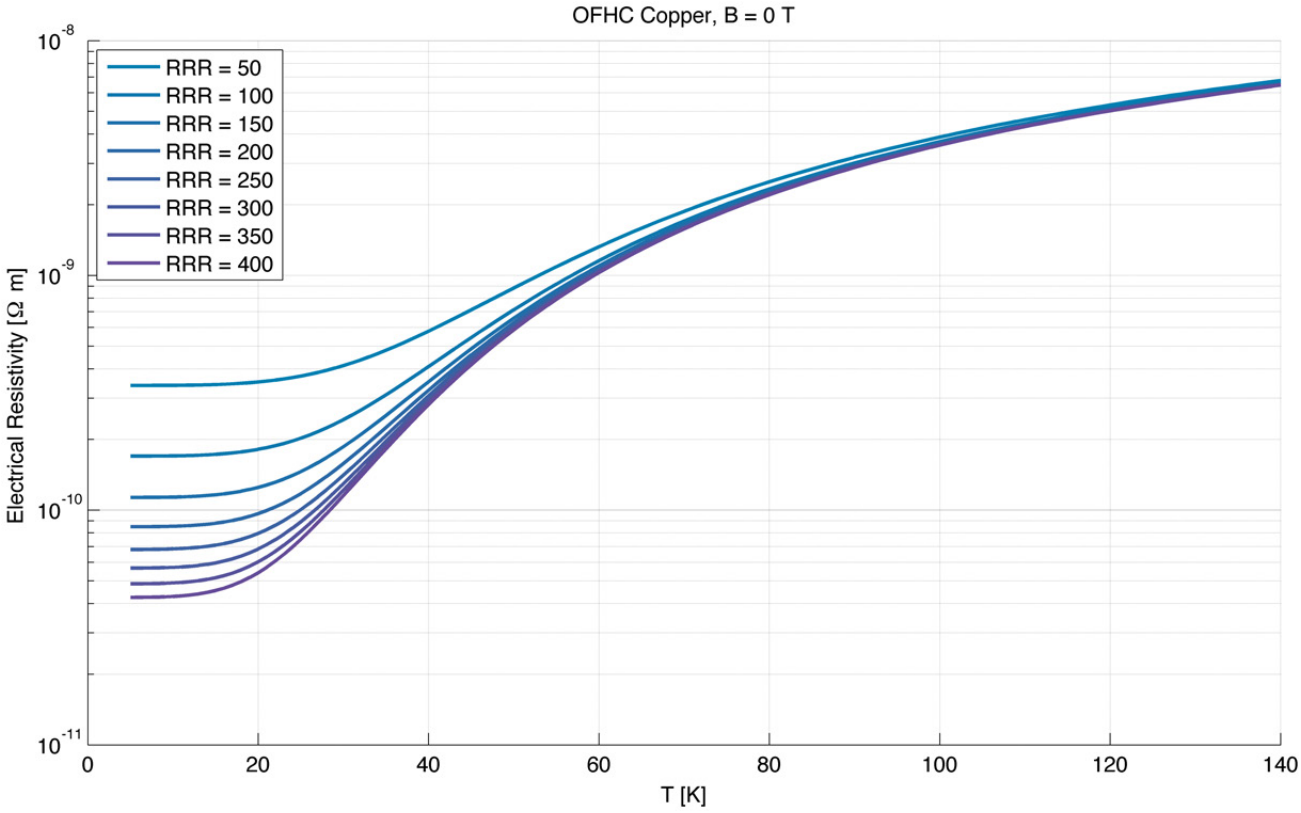

Figure G.1: Electrical resistivity of Copper as function of RRR and T at zero field.

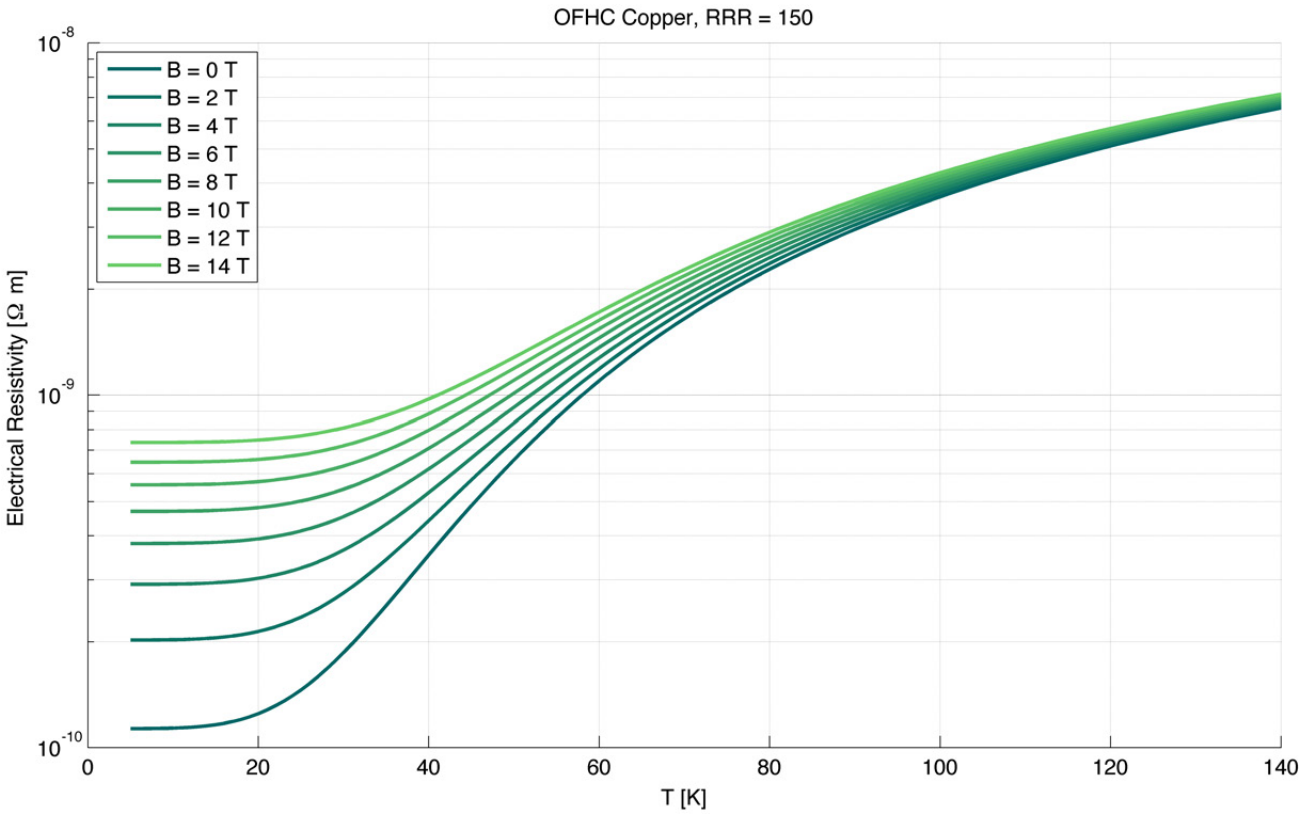

Figure G.2: Electrical resistivity of Copper as function of B and T at a RRR of 150.

Name	P_1	P_2	P_3	P_4
Value	0.0002667	1.234	0.0001469	1.229

Table G.2: Fitting coefficients for the scaling relation of the electrical resistivity of Hastelloy.

Thermal Conductivity

The thermal conductivity determines the heat flux resulting from a temperature difference. The thermal conductivity of the tape, k_{tape} in units Wm/K is given by

$$k_{tape} = w_{tape}\left(h_{hs}k_{hs}(T) + h_{ybco}k_{ybco}(T) + h_{ag}k_{ag}(B,T) + h_{cu}k_{cu}(RRR,T,B)\right), \tag{G.6}$$

where k_{hs}, k_{ybco}, k_{ag}, and k_{cu} are the thermal conductivities of the individual materials. Note that the individual conductivities are given in units of W/Km. Since the electrical resistivity and the thermal conductivity are 'linked' through the Wiedemann Franz law, it is of no surprise that for the thermal conductivity also the copper also plays the most important role.

Copper

The thermal conductivity of copper at zero field has been provided by NIST and is available for RRR values of 50, 100, 150, 300 and 500 [46]. The scaling relation is given by

$$k_{cu,0}(T) = 10 \wedge \left(\frac{a + cT^{0.5} + eT + gT^{1.5} + iT^2}{1 + bT^{0.5} + dT + fT^{1.5} + hT^2}\right), \tag{G.7}$$

where coefficients a,b,c,d,e,f,g,h,i are given for various values of RRR in Table G.3. The equation is valid in a temperature range of $4 - 300\ K$. If necessary at different RRR values, the curves can be interpolated. In order to take the magneto resistivity into account, it is possible to use the scaling from the electrical conductivity between zero field and the requested field in combination with the Wiedemann-Franz law [47]. The resulting scaling relation is

$$k_{cu}(RRR,T,B) = k_{cu,0}(RRR,T) \cdot \frac{\rho_{cu}(RRR,T,0)}{\rho_{cu}(RRR,T,B)}. \tag{G.8}$$

As an example some curves are provided in Figure G.4 and Figure G.5.

RRR	50	100	150	300	500
a	1.8743	2.2154	2.3797	1.357	2.8075
b	-0.41538	-0.47461	-0.4918	0.3981	-0.54074
c	-0.6018	-0.88068	-0.98615	2.669	-1.2777
d	0.13294	0.13871	0.13942	-0.1346	0.15362
e	0.26426	0.29505	0.30475	-0.6683	0.36444
f	-0.0219	-0.02043	-0.019713	0.01342	-0.02105
g	-0.051276	-0.04831	-0.046897	0.05773	-0.051727
h	0.0014871	0.001281	0.0011969	0.0002147	0.0012226
i	0.003723	0.003207	0.0029988	0	0.0030964

Table G.3: Fitting coefficients from NIST for the scaling relation of the thermal conductivity of copper at zero field.

Silver

Scaling relation for the thermal conductivity of silver is given by a polynomial of the form [43, 44]

$$k_{ag,0} = aT^5 + bT^4 + cT^3 + dT^2 + eT + f, \tag{G.9}$$

where the coefficients a, b, c, d, e and f are given in Table G.4. Similar to the copper for the silver the magnetic field is taken into account using

$$k_{ag}(T,B) = k_{ag,0}(T) \cdot \frac{\rho_{ag}(T,0)}{\rho_{ag}(T,B)}. \tag{G.10}$$

As an example several curves are plotted in Figure G.6.

Hastelloy

The thermal conductivity of Hastelloy is calculated in a similar way as silver using the polynomial from equation G.9 [44]. The coefficients for Hastelloy are given in two temperature domains and can be found in table G.5.

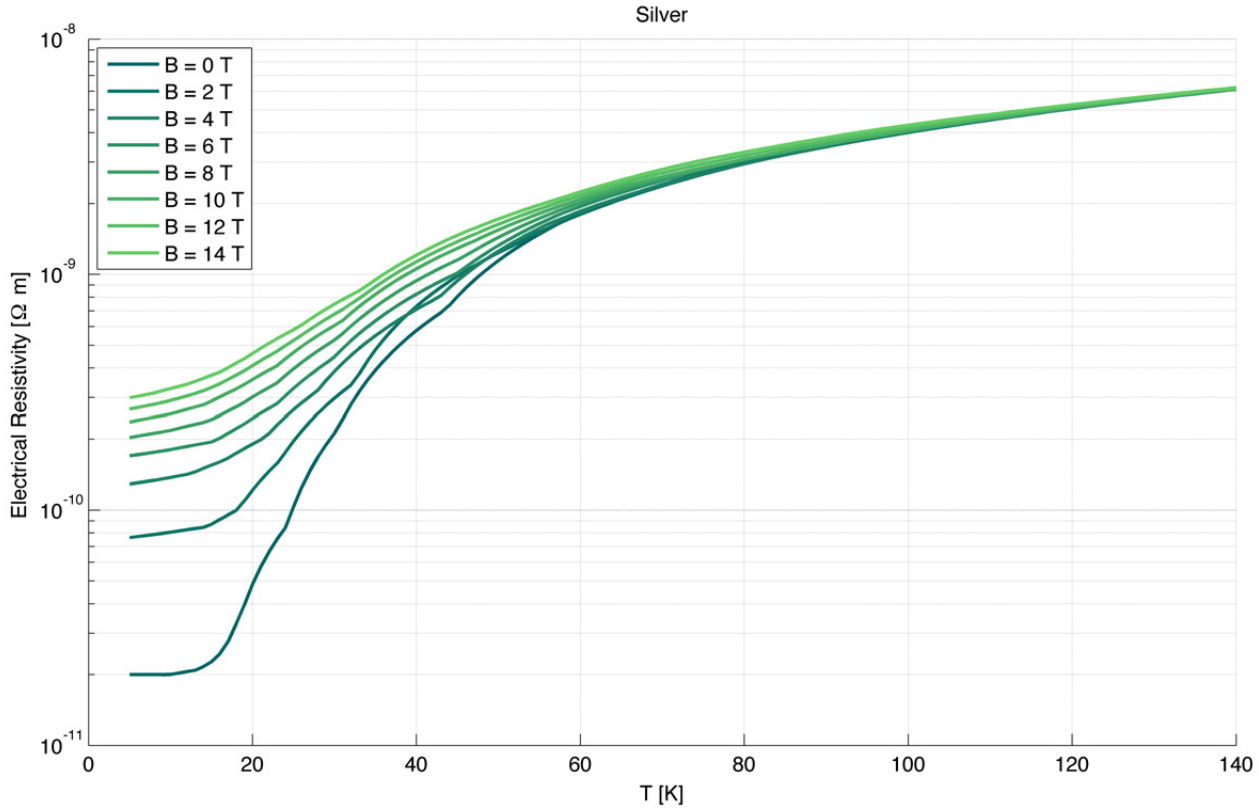

Figure G.3: Electrical resistivity of Silver as function of B and T.

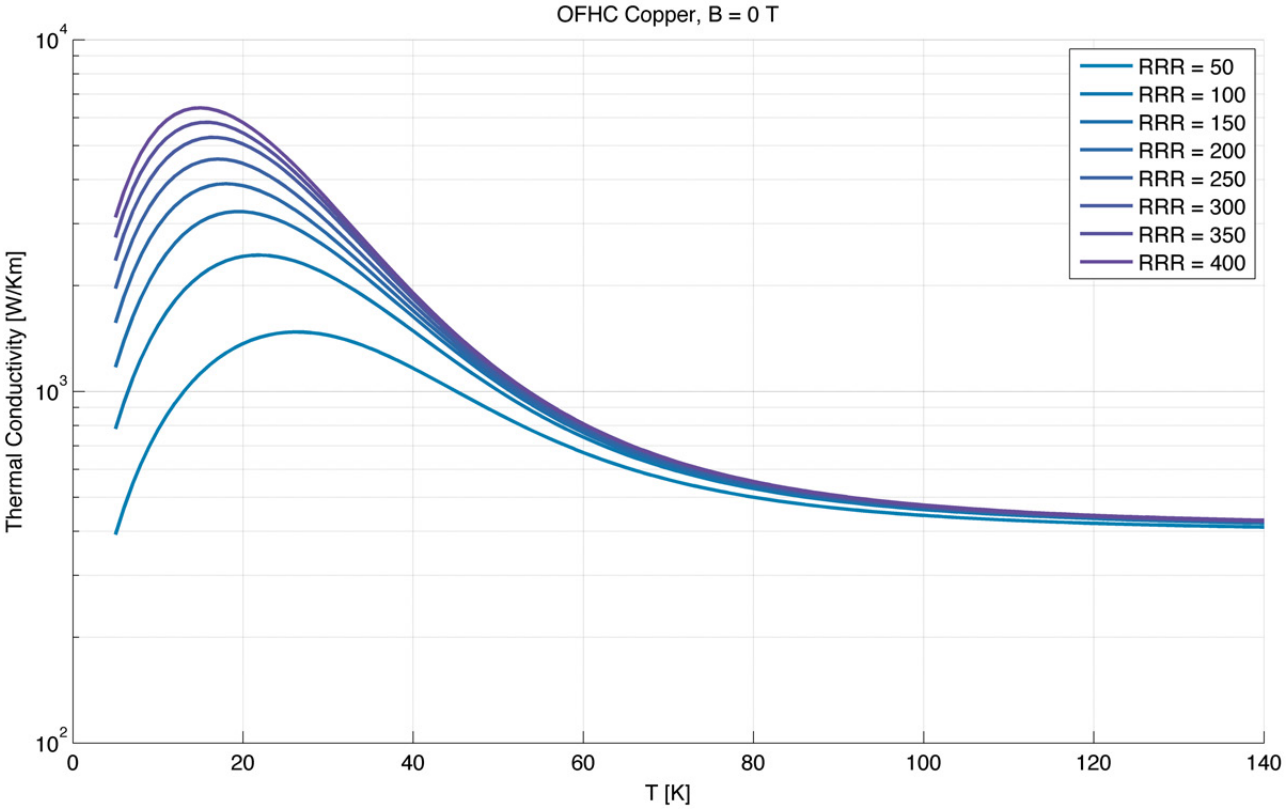

Figure G.4: Thermal conductivity of Copper as function of RRR and T at zero field.

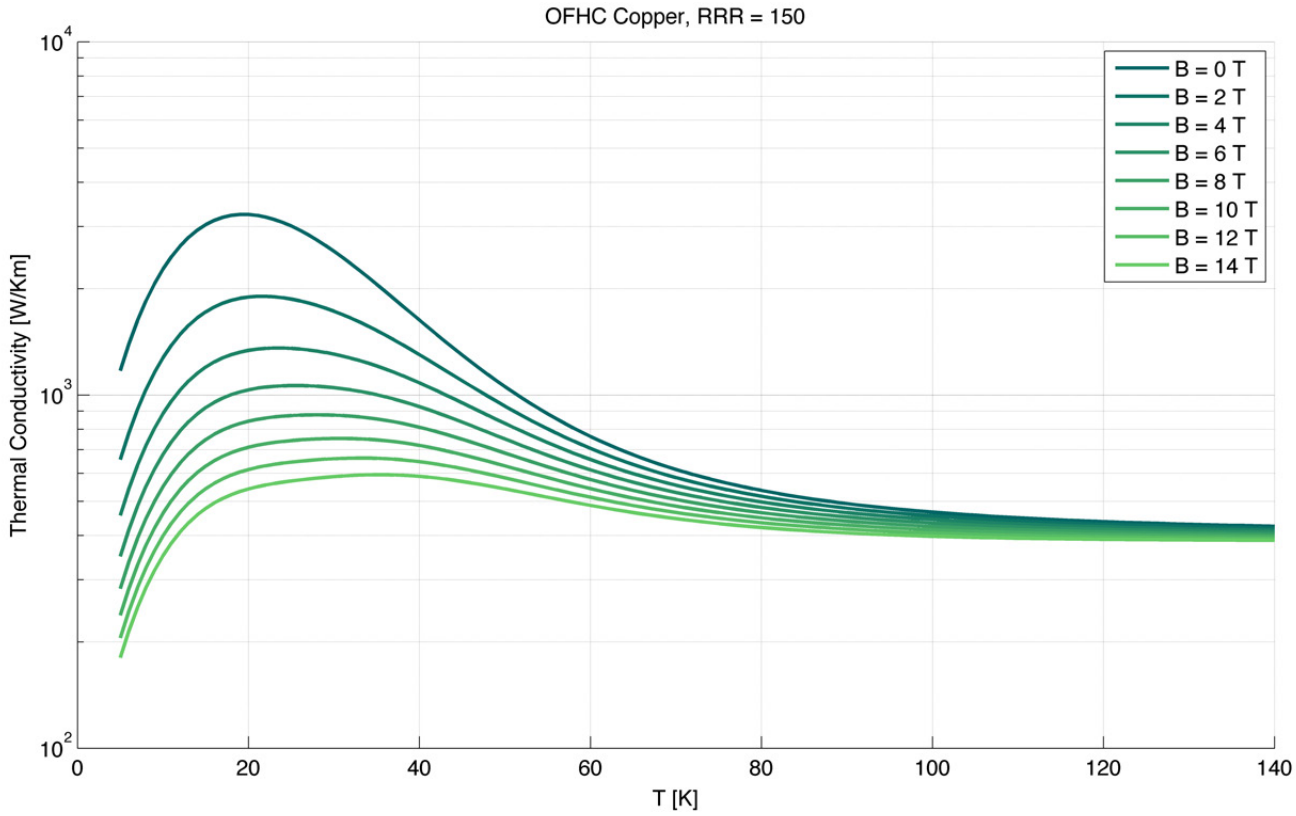

Figure G.5: Thermal conductivity of Copper as function of B and T at a RRR of 150.

range	$T \leq 33$	$33 < T \leq 100$	$100 < T$
a	$-8.085202766065000 \times 10^{-4}$	$-3.358195377766776 \times 10^{7}$	$8.147381572319895 \times 10^{-11}$
b	0.084173230577580	$1.869961406456805 \times 10^{-4}$	$-1.042739292996614 \times 10^{-7}$
c	−2.898387926986296	−0.041125881979616	$5.409027188706845 \times 10^{-5}$
d	30.127572196852682	4.473201297735611	−0.013972777872369
e	$1.323932096483007 \times 10^{2}$	$-2.413050714859127 \times 10^{2}$	1.569131427472265
f	$1.031106730600989e \times 10^{2}$	$5.659032445727915 \times 10^{3}$	$4.105421708582979 \times 10^{2}$

Table G.4: Coefficients for scaling relation of the thermal conductivity of silver.

range	$T \leq 55$	$55 < T$
a	$-1.976150097497916 \times 10^{8}$	$3.544514666284345 \times 10^{11}$
b	$1.692069531515161 \times 10^{6}$	$-3.085569423939295 \times 10^{8}$
c	$3.428435748706821 \times 10^{5}$	$9.862456406179634 \times 10^{6}$
d	−0.008289421572708	−0.001448613557764
e	0.399017559651135	0.120321620954427
f	−0.827062339102484	3.632700117022619

Table G.5: Coefficients for scaling relation of the thermal conductivity of Hastelloy.

YBCO

Thermal conductivity of YBCO is also calculated with G.9. The coefficients are also provided in two temperature domains and are available in Table G.6.

range	$T \leq 70$	$70 < T$
a	$-1.266103106492942 \times 10^5$	$-1.316704893540544 \times 10^9$
b	0.002670105477219	$2.636151594117440 \times 10^6$
c	−0.197035302542769	−0.001601689632073
d	4.933962659604384	0.428760641312538
e	29.651536939501670	−53.306643333287260
f	66.578192505447330	$3.682252343338599 \times 10^3$

Table G.6: Coefficients for scaling relation of the thermal conductivity of Hastelloy.

Heat Capacity

Specific heat determines the amount of energy is required to increase the temperature of a material. The thermal conductivity of the tape, in units of J/Km is given by

$$C_{tape}(T) = w_{tape}\left(d_{hs}h_{hs}C_{hs}(T) + d_{ybco}h_{ybco}C_{ybco}(T) + d_{ag}h_{ag}C_{ag}(T) + d_{cu}h_{cu}C_{cu}(T)\right), \tag{G.11}$$

where d_{hs}, d_{ybco}, d_{ag} and d_{cu} are the densities of the materials given in Table G.7; and C_{hs}, C_{ybco}, C_{ag} and C_{cu} the specific heats of the materials given in the Sections below (and to provide an overview in Figure G.7). Note that the unit of the specific heats is J/kgK. In contrast to the thermal conductivity and the electrical resistivity for the heat capacity the contribution of all materials is of importance. Especially the copper and the Hastelloy because they are the thickest layers in the tape modelled for this work.

Copper

Specific heat from copper is calculated using an equation from NIST which is given as [46]

$$\begin{aligned} C_{cu}(T) = 10 \wedge (&a + b(log_{10}T) + c(log_{10}T)^2 + d(log_{10}T)^3 + e(log_{10}T)^4 \\ &+ f(log_{10}T)^5 + g(log_{10}T)^6 + h(log_{10}T)^7 + i(log_{10}T)^8) \end{aligned} \tag{G.12}$$

where the coefficients are given in Table G.8.

Silver

The heat capacity of silver is given by the following polynomial [44]

$$C_{ag}(T) = aT^3 + bT^2 + cT + d, \tag{G.13}$$

The coefficients are provided in three temperature domains and are given in Table G.9.

Hastelloy

The heat capacity of Hastelloy is given by the following polynomial [44]

$$C_{hs}(T) = aT^5 + bT^4 + cT^3 + dT^2 + eT + f, \tag{G.14}$$

where the coefficients are given by Table G.10.

YBCO

For YBCO the specific heat is given using the same formula as Hastelloy [44]. The coefficients are given in Table G.11.

d_{hs}	d_{ybco}	d_{ag}	d_{cu}
8.89×10^3	6.3×10^3	10.49×10^3	8.94×10^3

Table G.7: Densities of the materials in an YBCO coated conductor in kg/m^3.

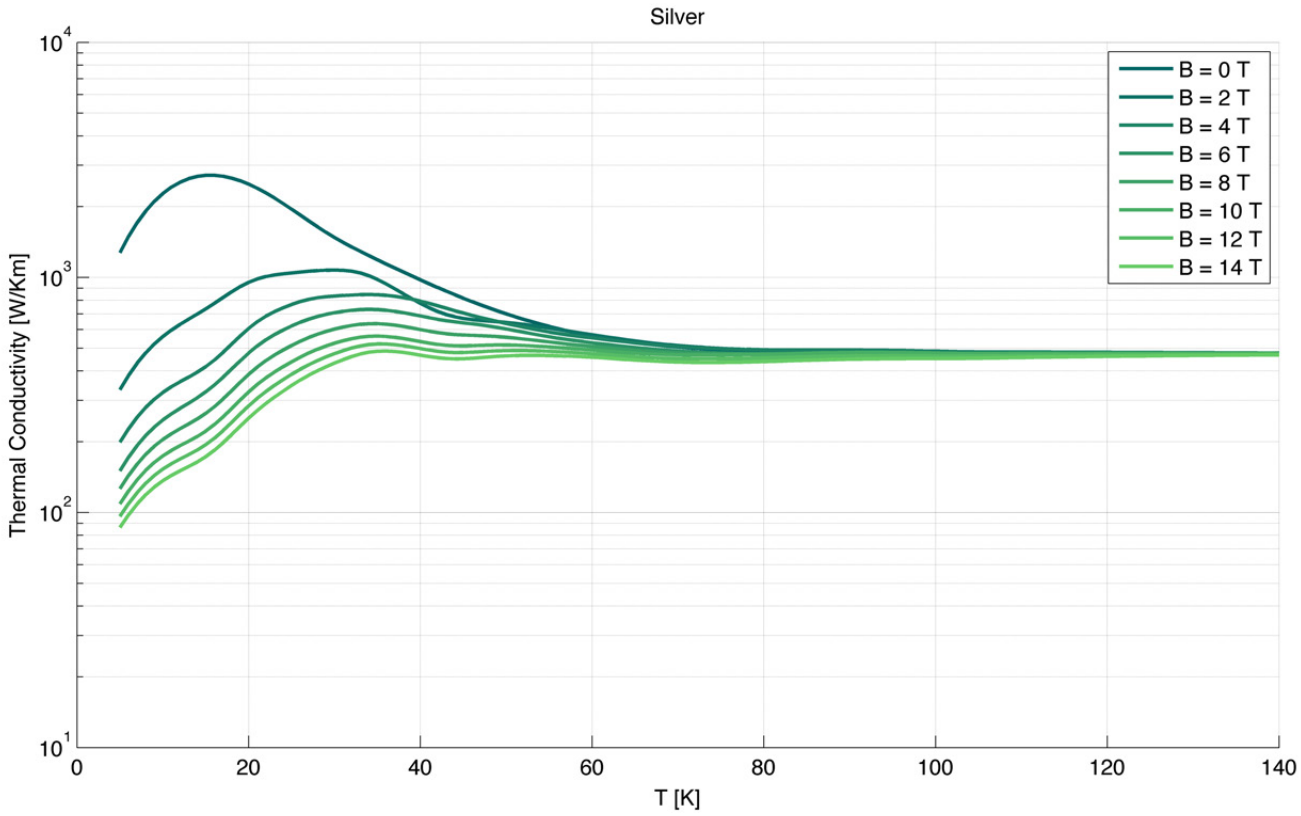

Figure G.6: Thermal conductivity of Copper as function of B and T at a RRR of 150.

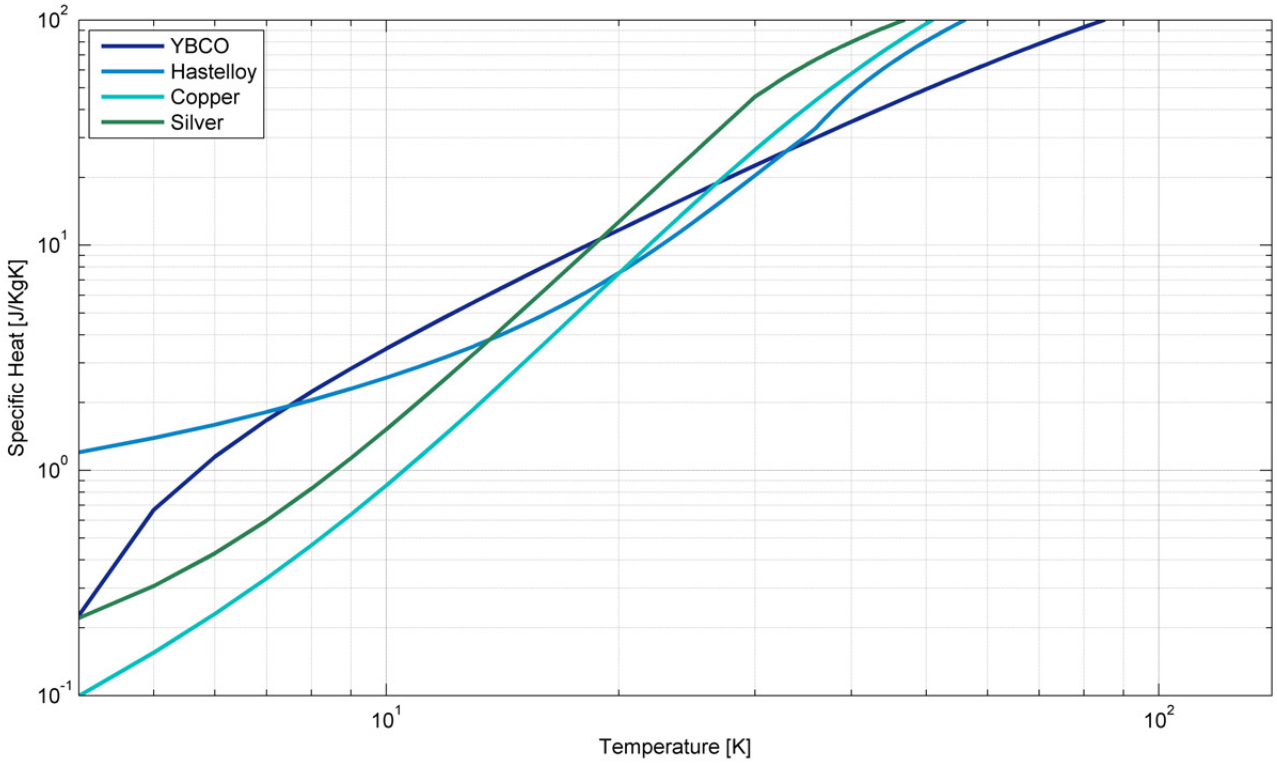

Figure G.7: Specific heat as function of temperature of the materials in an YBCO coated conductor.

name	a	b	c	d	e	f	g	h	i
value	-1.91844	-0.15973	8.61013	-18.996	21.9661	-12.7328	3.54322	-0.3797	0

Table G.8: Coefficients for scaling relation of the specific heat of Copper.

range	$T \leq 30$	$30 < T \leq 125$	$125 < T$
a	0.00201	1.11189×10^{-4}	3.70101×10^{-6}
b	-0.012	-0.04289	-0.00326
c	0.071	6.05068	1.0369
d	-2.66454×10^{-14}	-100.586	116.90736

Table G.9: Coefficients for scaling relation of the specific heat of silver.

range	$T \leq 35$	$35 < T$
a	$-8.659744297212208 \times 10^{-7}$	$20.150134339872814 \times 10^{-10}$
b	$7.209308577841222 \times 10^{-5}$	$-1.458398200879766 \times 10^{-7}$
c	-0.001346146407585	$4.376675190884510 \times 10^{-5}$
d	0.017992946436959	-0.015104610350977
e	0.084834978274794	4.491152093383801
f	0.642508075273653	$-1.107126478142060 \times 10^{2}$

Table G.10: Coefficients for scaling relation of the specific heat of Hastelloy.

range	All
a	$-7.567485538209158 \times -10$
b	$6.351452642016898 \times -7$
c	$-1.947975786547597 \times -4$
d	0.023616673974415
e	0.239331954284042
f	-1.096191721280114

Table G.11: Coefficients for scaling relation of the specific heat of YBCO.